Flux dependence of topological superconductivity in two-dimensional heterostructures

Alexander M. Whiticar

Ph.D. Thesis

Center for Quantum Devices
Niels Bohr Institute
Faculty of Science
University of Copenhagen

January 24th 2020

Academic advisor:

Prof. Dr. Marcus

Assessment committee:

Prof. Dr. Paaske
Prof. Dr. Schönenberger
Dr. De Franceschi

FLUX DEPENDENCE OF TOPOLOGICAL SUPERCONDUCTIVITY IN TWO-DIMENSIONAL HETEROSTRUCTURES

ABSTRACT

The realization of a quantum computer requires the development of a scaleable and reliable two-level system. This thesis presents the knowledge gained from experimenting with a series of low-dimensional hybrid superconductor/semiconductor quantum devices to investigate topological superconductivity. A topological superconductor is expected to host Majorana zero modes (MZMs) at its boundaries that are described by a non-local wavefunction obeying non-abelian exchange statistics. These attributes of MZMs enable the critical 'fault-tolerant' quantum computation, whereby quantum information is stored in the fermionic parity of a non-local state. This method of encoding is predicted to protect quantum information from local noise sources, allowing for longer qubit lifetimes. This work extends beyond local tunneling spectroscopy signatures of MZMs on proximitized nanowires and focuses on investigating non-locality and Majorana parity that requires two-dimensional device geometries.

My dissertation demonstrates that two-dimensional InAs-Al heterostructures are an encouraging material system for investigating topological superconductivity. This platform allows for conventional top-down fabrication, facilitating scalable device geometries necessary for pursuing topological qubit networks. A series of device geometries ranging in complexity were investigated to assess the feasibility of creating the first topological qubit using two-dimensional heterostructures.

The essential findings include the observation of conductance oscillations through a Majorana island interferometer with a flux period of h/e (h is Planck's constant; e is the elementary charge). This indicates coherent transport of single electrons through the islands - a signature of Majorana non-locality. I demonstrate the progress that was made towards parity-to-charge conversion for detecting the two parity states of a topological qubit. This includes the observation of transport signatures of zero-energy mode hybridization that are compatible with predictions of MZM hybridization. Finally, I introduce a fully two-dimensional platform based on a Josephson junction that enables a flux controlled topological phase transition. I report on transport signatures consistent with the observation of MZMs in a topological Josephson junction.

The primary implication of this work is that two-dimensional heterostructures offer a promising platform for scalable topological quantum computation.

ACKNOWLEDGEMENTS

Anyone who has been a part of a condensed matter experiment will tell you that it involves a collaboration of many dedicated researchers. I was fortunate enough to have had both the assistance and guidance of many talented colleagues during my three-year Ph.D.

I would like to extend a sincere thank you to **Charlie** for taking me on as a student and for being a remarkable mentor. His ceaseless enthusiasm about every aspect of physics and his constant drive to improve work-life, both on a technical and social level are admirable. I hold in high regard his swift and keen interpretations of experimental data and his ability to inspire students to pursue challenging but rewarding experiments. Thank you for making QDev the impressive lab that it is today and for *limitless* coffee.

I would like to thank my assessment committee members, **Jens Paaske**, **Christian Schönenberge**r, and **Silvano De Franceschi** for taking the time to evaluate this dissertation.

The results presented in this thesis builds upon the work and dedication of both former and present Topo2DEG team members that deserve recognition. First and foremost, the previous members **Morten**, **Henri**, and **Fabrizio**. Without their hard work to develop the hybrid quantum well heterostructures, the results of this thesis would not have been the same. A ginormous thanks to **Antonio** - who is a fantastic colleague and friend. I am grateful to have had the opportunity to work so closely with him over the past three years. I will remember fondly all of the days discussing life and a little bit of physics and our midnight encounters to load the fridge. **Eoin** deserves thanks for the continued support both as an experimentalist and as a mentor. One day I will miss our breakfast club. Let us hope that day does not come soon. I would like to thank the remaining members of the A-team - **Asbjørn**, **Ahnaf**, and **Abhishek** - for ensuring that the Topo2DEG spirit is kept alive. And I would like to thank the fresh blood who recently join the A-ish-team **Daniel**, **Andreas**, **Felix** and **Sangeeth**, who will now have to carry the torch.

A special mention is dedicated to the team at Purdue university. It has been a pleasure and a unique experience to work in close collaboration with a skilled materials team. I would like to thank **Tiantian**, **Candice**, **Sergei**, **Ray**, **Geoff**, and **Mike** for this opportunity. I am eager to see how the platform develops.

I would like to thank **Lucas**, **Mingtang**, and **Filip K.** for my brief stint working on SAG. It was an enjoyable experience to see researchers come together from different backgrounds on a common goal.

An experimentalist at QDev is fortunate to have top-tier theory support for unraveling the mysteries of Majoranas. I would like to thank **Ady**, **Bernard**, **Chetan**, **Erikas**, **Erez**, **Jens S.**, **Jukka**, **Karsten**, **Martin**, **Michael**, **Panagiotis**, **Roman**, **Torsten**, **Tommy**, and **Setiawan** for the countless hours discussing experimental data and theoretical interpretations.

I would like to thank **Amir Yacoby** for my visit to Harvard and to **Charlotte** for being a great host. It was an eye-opening experience to see the wide range of experiments being performed in the lab, all using different measurement techniques.

I thank the technical, electrical, and administrative staff at QDev for keeping everything running smoothly, such that the only bottle-neck of a project is an experimentalist's dedication. In this regard, I thank the technical staff, **Nader**, **Karolis**, and especially **Claus** for coming in at a moment's notice to rescue fridges and tools. I would like to acknowledge support from the electronic team, **Rikke**, and **Ruben**. And I would like to extend a warm thank you to the admin team, **Dorthe**, **Katrin**, **Maria**, and **Marianne** for making work life more enjoyable.

I am in debt to the fantastic company of **Anders**, **Fabio**, and **Saulius**. It was an enjoyable experience getting to know such exuberant PhD students. Thank you for making the PhD unforgettable, I am looking forward to what adventures await.

I would like to thank the entire QDev community for having a strong and welcoming social atmosphere. The grand diversity that makes up the mixed melting point of cultures at QDev makes it an interesting place to work. I will remember fondly the retreats, BBQs, and most importantly the extensive betting problem that QDev has. To this end, I would like to thank **Albert**, **Anasua**, **Damon**, **Deividas**, **Dovydas**, **Federico**, **Judith**,**Lukas**, **Malcolm**, **Rob**, for all of the wonderful conversations and laughs.

On a personal level, I would like to acknowledge my friends and family back in Canada. To my friends, it is always refreshing to visit and reflect on what is important in life. I appreciate being reminded that publications are not the meaning of life. To my **parents** and **brother**, thank you for your unwavering support over the past five years in Copenhagen. And lastly, I would like to thank **Frida** for reminding me what is beautiful in life.

LIST OF PUBLICATIONS

Results presented in this thesis are adapted from the following manuscripts:

1. **A.M. Whiticar***, A. Fornieri*, E. O'Farrell, A. Drachmann, T. Wang, C. Thomas, S. Gronin, R. Kallaher, G. Gardner, M. Manfra, C.M. Marcus, F. Nichele. Interferometry and coherent single-electron transport through hybrid superconductor-semiconductor Coulomb islands.

   In review. *arXiv* 1902.07085 (2019).

2. A. Fornieri*, **A.M. Whiticar***, F. Setiawan, E. Marin, A. Drachmann, A. Keselman, S. Gronin, C. Thomas, T. Wang, R. Kallaher, G. Gardner, E. Berg, M. Manfra, A. Stern, C.M. Marcus, F. Nichele. Evidence of topological superconductivity in planar Josephson junctions.

   Nature, 569 (2019).

3. F. Krizek, J. Sestoft, P. Aseev, S. Marti-Sanchez, S. Vaitiekenas, L. Casparis, S. Khan, Y. Liu, T. Stankevic, **A.M. Whiticar**, A. Fursina, F. Boekhout, R. Koops, E. Uccelli, L. Kouwenhoven, C.M. Marcus, J. Arbiol, P. Krogstrup. Field effect enhancement in buffered quantum nanowire networks.

   Phys. Rev. Materials, **2**, 093401 (2018).

4. E. O'Farrell, A. Drachmann, M. Hell, A. Fornieri, **A.M. Whiticar**, E. Hansen, S. Gronin, G. Gardner, C. Thomas, M. Manfra, K. Flensberg, C.M. Marcus, F. Nichele. Hybridization of Subgap States in One-Dimensional Superconductor-Semiconductor Coulomb Islands.

   Phys. Rev. Lett., **121**, 256803 (2018).

5. S. Vaitiekenas, **A.M. Whiticar** M.-T. Deng, F. Krizek, J. Sestoft, C.J. Palmstrøm, S. Marti-Sanchez, J. Arbiol, P. Krogstrup, L. Casparis, C.M. Marcus. Selective-Area-Grown semiconductor-superconductor hybrids: A basis for topological networks.

   Phys. Rev. Lett. **121**, 147701 (2018).

6. F. Nichele, A. Drachmann, **A.M. Whiticar**, E. O'Farrell, H. Suominen, A. Fornieri, T. Wang, G. Gardner, C. Thomas, A. Hatke, P. Krogstrup, M. Manfra, K. Flensberg, C.M. Marcus. Scaling of Majorana Zero-Bias Conductance Peaks.

   Phys. Rev Lett., **119**,136803 (2017).

*Equal contribution

Publications that are not included in this thesis:

1. E. Mårtensson, **A.M. Whiticar**, M. De La Mata, R. Zamani, J. Johansson, J. Nygård, K. Dick, J. Bolinsson. Understanding GaAs Nanowire Growth in the Ag–Au Seed Materials System.

   Cryst. Growth Des., 18(11) pp 6702-6712 (2018).
2. **A.M. Whiticar**, E. Mårtensson, J. Nygård, K. Dick, J. Bolinsson. Annealing of Au, Ag and Au–Ag alloy nanoparticle arrays on GaAs (100) and (111)B.

   Nanotechnology, 28 (20), 205702 (2017).
3. C. Lindberg, **A.M. Whiticar**, K. Dick, N. Skőld, J. Nygård, J. Bolinsson. Silver as seed-particle material for GaAs nanowires – dictating crystal phase and growth direction by substrate orientation.

   Nano lett., 16(4) (2016).

CONTENTS

1

MOTIVATION

Currently there is an immense global push to realize quantum technologies. At the pinnacle of this endeavor is the pursuit of a fully-fledged universal quantum computer. The current leading approach to quantum computing is based on superconducting circuits, which use a Josephson junction as a non-linear element to create an anharmonic oscillator [1, 2]. A recent breakthrough came from the Martinis group at Google who achieved quantum supremacy, a feat where a quantum processor outperforms any classical computer on a specialized computation [3]. This technology is anticipated to allow for quantum processors consisting of $\sim$ 1000 quantum bits (qubits), while todays most advanced quantum processors comprise less than a hundred [2]. However, qubits are prone to decoherence, a process whereby quantum information stored in the quantum state is lost. An important consideration of decoherence is that only a finite amount of gate operations (calculations) can be performed before the information is lost. To achieve a more powerful quantum processor, both the number of qubits and the number of executable gate operations need to be improved in concert. This consideration appears to be difficult for all known qubit technologies today. Fortunately, the solution to the problem of decoherence may come from fundamental physics research.

In 1980, a new field of physics, known as topological condensed matter, was born with the discovery of the quantum Hall effect [4]. Unbeknownst to von Klitzing at the time, the precise quantization of conductance in units of e^2/h is deeply rooted in the topology of the system [5, 6] *. In fact, the robustness of the quantum Hall effect and its insensitivity to

---

*e is the elementary charge and h is the Planck constant

specific experimental conditions allows to be used as a standard for electrical resistance [7]. This culminated in 2016 when Nobel prize in physics was awarded to Kosterlitz, Haldane, and Thouless for their contribution to the discovery of topological phase transitions and topological phases of matter.

It is based on these two topics that this dissertation finds its footing. The question that is currently being investigated in many laboratories around the world is if topology can be harnessed to protect quantum information from decoherence. It is this prospect that led to the conception of the field known as 'topologically-protected' or 'fault-tolerant' quantum computation [6]. Various quantum systems are expected to exhibit topological phases of matter [8]. However, the current leading approach for fault-tolerant quantum computation is based on systems with Majorana zero modes (MZMs) [9, 10]. It is expected that quantum information encoded in this system will be protected from the common sources of decoherence that perturb conventional qubits.

Majorana zero modes are exotic quasiparticle excitations that appear at the boundaries of a topological superconductor [10, 11]. While there are only a few bulk material candidates that may exhibit topological superconductivity [12, 13], it is predicted that with certain material combination readily available in the laboratory, topological phases of matter can be engineered [14]. This thesis focuses on the proposal, based on one-dimensional nanowires with strong Rashba spin-orbit interaction and proximity induced conventional superconductivity, that are subjected to an external magnetic field [15, 16]. Each of these four key elements will be introduced in **Chapter 2** and the material system used to investigate topological superconductivity is presented in **Chapter 3**. This thesis focuses on the development of a new material system based on quantum well heterostructures, where an Indium-Arsenide (InAs) two-dimensional electron gas is put in proximity to a thin film of superconducting Aluminum (Al) [17].

1.1 Majorana Fermions and where to find them

The concept of Majorana fermions started with a young Italian physicist named Ettore Majorana. In 1937, Ettore Majorana was investigating the relativistic Dirac equation [18]. This equation describes fermionic particles and predicted the existence of anti-particles. By demanding his solution to be real (instead of the conventional imaginary solutions), Majorana found that the wavefunction describing a particle was also its own antiparticle [19]. For decades physicists have looked to fundamental particles and high energy physics for evidence of the hypothetical particle - now commonly referred to as a Majorana fermion. However, convincing evidence is yet to be found [20]. At the turn of the century, it was discovered that the particle-hole symmetry offered by a superconductor can give rise to quasiparticle excitations that obey similar properties to the proposed fundamental particles by Ettore Majorana [14, 21, 22]. These excitations are referred to as Majorana zero modes (MZMs).

To first introduce the mathematical description of Majorana fermions, a mathematical decomposition of standard Dirac fermions into a Majorana basis can be performed. Dirac fermions are described by many-body creation complex operators $c_j^\dagger$, which creates an electron with quantum numbers j and the operator c_j annihilates it (creates a hole). As these fermionic operators describe identical particles they obey the anticommutation relations [23],

$$\{c_i, c_j\} = \{c_i^\dagger, c_j^\dagger\} = 0 \quad \{c_i, c_j^\dagger\} = \delta_{ij}$$

These fermionic operators can be decomposed in real and imaginary parts in terms of new fermionic operators γ_i as [10, 11],

$$c_j = \frac{1}{2}(\gamma_1 + i\gamma_2), \quad c_j^\dagger = \frac{1}{2}(\gamma_1 - i\gamma_2) \quad . \tag{1.1}$$

This decomposition leads to a fermion being divided into two halves by γ_i. Inverting the preceding equations gives,

$$\gamma_1 = (c_j + c_j^\dagger), \quad \gamma_2 = i(c_j - c_j^\dagger) \quad .$$

By inspection, it is observed that the γ operators are composed of equal electron and hole parts and satisfy,

$$\gamma_i = \gamma_i^\dagger, \quad \gamma_i^2 = 1 \quad .$$

Therefore, the operator $\gamma_i^\dagger$ creates a particle that is identical to its own antiparticle. These particles are indeed Majorana fermions. Additionally, γ_i are fermionic operators that obey the anti-commutator relations [10],

$$\{\gamma_i, \gamma_j\} = 2\delta_{ij}; \quad \{\gamma_i, \gamma_j^\dagger\} = 0 \quad \text{for i} \neq \text{j} \quad .$$

These results may not come as a surprise to some, since by construction it was demanded that γ to be an equal superposition of electron and hole parts and may seem to carry no physical consequence. However, it will become evident in the following section that if these two Majorana fermions are isolated from each other (as is the case of a topological superconductor), then this description becomes more than an abstract decomposition and results in Majorana zero modes.

In solid state systems, quasiparticle excitations are primarily electrons and holes that carry charge and spin. As Majorana fermions are their own antiparticles they are constrained from having spin or charge. This implies that a solid-state realization of Majorana fermions necessitates emergent non-trivial quasiparticle excitations. A promising candidate material is a superconductor due to particle-hole symmetry. In a superconductor, single-quasiparticle excitations are known as Bogoliubons b and are described by [10, 11],

$$b_\downarrow^\dagger = uc_\downarrow^\dagger - vc_\uparrow, \quad b_\uparrow = vc_\downarrow^\dagger + uc_\uparrow \quad ,$$

which are excitations composed partly electron and hole components. Here u and v represent coherence factors of electron-like and hole-like excitations, respectively (more on this in Chapter 2.3.1). Particle-hole symmetry states that for a quasiparticle b with energy E, there exists another quasiparticle with energy $-E$ such that $b(E) = b^\dagger(-E)$, as depicted in Fig. 1.1a [11]. If the energy of the particle and antiparticle is zero then $b_\uparrow = b_\downarrow^{\dagger}$*. However, these zero-energy excitations are not necessarily Majorana fermions. In conventional superconductors, electrons form spin-singlet pairs (s-wave), causing the particle and antiparticle to have opposite spin. The electron pairing in a p-wave topological superconductor is spinless, allowing for quasiparticle excitations obeying $\gamma = \gamma^\dagger$, which are indeed Majorana fermions as shown in Fig. 1.1b.

In the context of solid state, these zero-energy quasiparticle excitations are localized modes living at the boundaries of a topological superconductor (see Fig. 1.2), and are referred to as Majorana zero modes (MZMs) [10, 24]. As opposed to the fundamental particle postulated

---

*The excitation is described by a linear combination of equal electron and hole parts ($|u|^2 = |v|^2$)

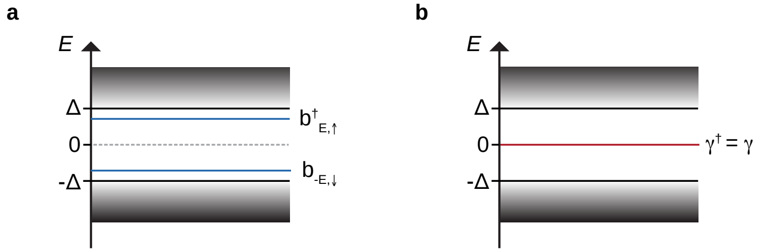

Figure 1.1: Excitation spectrum of a trivial and topological superconductor: **a**, Schematic representation of the quasiparticle spectrum of a trivial superconductor with a spinful sub-gap excitations b at energy E and the particle-hole symmetric counterpart at $-E$. **b**, At the boundaries of a topological superconductor there exists zero-energy Majorana zero modes obeying $\gamma = \gamma^\dagger$.

by Ettore Majorana, these zero modes have an additional condition in that they commute with the Hamiltonian H of the system ($[H, \gamma] = 0$) [10, 24]. Since MZMs are zero energy excitations and a pair of MZMs describe a ordinary fermion (see Eq. 1.1) that can either be filled or empty, the ground state of a system with N Majorana pairs is 2^N-fold degenerate [10, 11]. **Chapter 2** examines how to engineer topological superconductivity and MZMs out of conventional material systems.

1.2 MAJORANA QUBITS

As opposed to conventional quasiparticle excitations in a superconductor, MZMs exhibit numerous exotic properties that enable fault-tolerant quantum computation. The following section will outline the two most relevant attributes for this thesis - Majorana non-locality and Majorana parity.

Figure 1.2: One-dimensional topological superconductor: Schematic representation of a one-dimensional topological superconducting nanowire. At the ends of the nanowire are two non-local Majorana zero modes γ_1 and γ_2.

Figure 1.2 depicts a one-dimensional topological superconductor with two non-local MZM excitation γ_1 and γ_2 at the ends of the wire. Majorana non-locality describes the spatial separation between a pair of MZMs, which together correspond to a single ordinary fermion. As a consequence, the quantum information stored in these quasiparticle excitations is stored non-locally and is protected from the environment due to the presence of a topological gap in the bulk of the nanowire [10]. Majorana qubits are expected to be insensitive to local noise sources, such as charge noise*, that leads to decoherence of conventional qubits, provided that the separation between pairs of MZMs is large. This property is expected to allow for long qubit lifetimes that scales with the length of the topological segment [25]. In **Chapter 6**, Majorana non-locality is investigated by performing an interferometry experiment, where coherent single-electron transport is observed through a Majorana island, consistent with theoretical expectations of non-locality [26].

The quantum information stored in these quasiparticle excitations is encoded in the Majorana parity of two MZMs. The parity of an individual MZM is ill-defined, as it is a fractionalized Dirac fermion [10, 11]. However, a pair of MZMs constitute a single fermion that can either be occupied or empty. The principle of using fermionic degrees of freedom as a qubit was first implementation in 1999 as a charge qubit [27], however, this technology suffers from short coherence times.

The concept of Majorana parity is introduced by considering the fermionic counting operator $n = c^\dagger c$, which determines if a state is occupied $(n = 1)$ or empty $(n = 0)$ [23]. If this operator is translated into the Majorana bias then,

$$n = \frac{1}{2}(1 + i\gamma_1\gamma_2) \quad .$$

The Majorana parity p is then defined as,

$$p_{1,2} = 1 - 2n = i\gamma_1\gamma_2 = \begin{cases} 1, & \text{if } n = 0 \\ -1, & \text{if } n = 1 \end{cases} \quad .$$

This parity is a two-level system that constitutes the basis of a Majorana qubit. As discussed above, this parity is protected due to the non-locality of the MZMs and, therefore, this information is expected to be robust to local sources of decoherence. In the following section, the concept of Majorana parity will be implemented into a topological qubit architecture.

---

*MZMs are charge neutral as they are composed of equal electron and hole parts

1.3 A ROUTE TO TOPOLOGICAL QUANTUM COMPUTATION

There are several competing schemes for implementing MZMs as a qubit [28–33]. Originally, a leading proposal for manipulating MZMs was to physically braid them in real-space using electrostatic gating in a T-shaped junction [28]. However, since an external magnetic field aligned to the nanowire axis is used to induce a topological phase transition, segments in an orthogonal orientation will experience a transverse magnetic field, which closes the topological gap (more on this in Chapter 2.4). Additionally, there is currently little experimental evidence of spatial control of MZMs by electrostatic gating, necessary for physically braiding. An alternative approach relies on performing a sequence of measurements to mimic braiding operations without the need of physically moving quasiparticles. This is known as the 'measurement-only' scheme [34].

In this dissertation, two different approaches for measuring the parity of Majorana zero modes are investigated. The first relies on interferometry, where the transmission phase through a Coulomb blockaded Majorana island is expected to be sensitive to the MZM parity [26, 29]. Indeed, in **Chapter 6** it was observed that conductance oscillations through the interferometer were sensitive to the parity of a Majorana island. A second approach for parity readout relies on the coupling between MZMs and a quantum dot (QD). The occupation of this quantum dot is predicted to be sensitive to the parity of MZM pairs, and therefore, can be used to manipulate and readout the Majorana qubits [30, 32, 33]. The progress towards a parity-to-charge conversion scheme is detailed in **Chapter 7** through **9**.

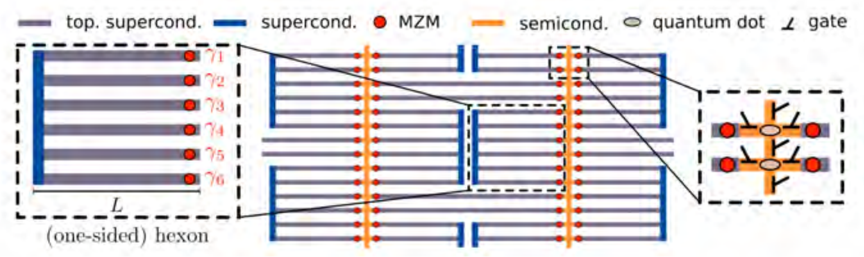

Figure 1.3: **Topological qubit network:** An array of linear topological wires forming a network of topological segments connected by trivial superconductor backbones. Quantum dots are adjacent to Majorana zero modes to allow for readout and manipulation of Majorana parity. This figure is adapted from Ref. [32].

The qubit architecture that this thesis is aspiring to is schematically drawn in Fig. 1.3. It consists of linear topological wires connected into a network by trivial superconducting backbones and loops [32]. To drive the nanowires into the topological regime with MZMs, a parallel magnetic field $B_{||}$ must be applied along the wire axis. Since magnetic field is typically a global parameter, all of the wires must be well aligned to the external magnetic field; otherwise the topological gap will not open (see Chapter 2.4). The quantum information is measured and controlled by adjacent QDs, as will be discussed in **Chapter 7**.

Several of the chapters of this thesis investigate the feasibility of constructing topological superconducting networks using hybrid superconducting-semiconductor two-dimensional electron gases. In **Chapter 3**, the material system consisting of an InAs quantum well that is proximitized by a thin film of epitaxial Al is introduced [17]. This platform is considered scaleable because it allows for device fabrication based on a top-down approach. This means that nanowire networks can be patterned by conventional lithographic techniques. As such, the fabrication of the network represented in Fig. 1.3 is not difficult to envision (see the devices in Chapters 8 and 9 for examples). However, the real experimental challenge is assigned to the formation of multiple connected topological superconducting qubits, each needing individual chemical potential tuning and QD parity readout.

An alternative two-dimensional geometry, based on Josephson junctions may relax some of these requirements. Figure 1.4a shows an elongated Josephson junction that is predicted to host a topological phase with MZMs appearing at the ends of the junction (see the MZM wavefunction probability density in Fig. 1.4b) [35, 36]. These junctions offer an additional control parameter, the superconducting phase difference ϕ across the junction, capable of tuning the topological phase of the junction. In Fig. 1.4c the topological phase diagram is plotted as a function of Zeeman energy E_Z and phase difference ϕ, showing that the topological phase can attained at lower E_Z at $\phi = \pi$ [36]. In principle, this geometry should be less dependent on the microscopic details of the junction, such as chemical potential, mitigating the need for fine-tuning of gate voltages to reach to the topological regime. Furthermore, by using a global out-of-plane magnetic field to tune the phase difference, multiple junctions can be tuned simultaneously into and out of the topological regime, opening up novel methods for braiding MZMs [37]. Devices based on this proposals are investigated in **Chapter 10**.

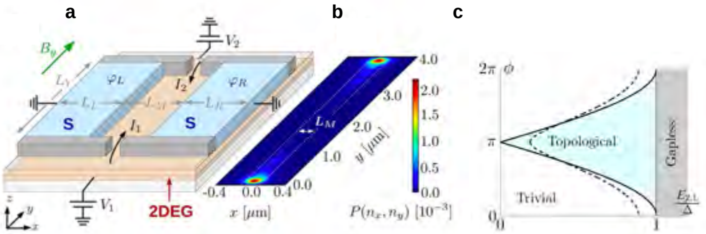

Figure 1.4: Topological planar Josephson junctions: a, Schematic illustration of a topological Josephson junction where a narrow channel is confined between two superconducting leads (S). **b**, In the topological regime, Majorana zero modes appear at the ends of the junction as shown by the wavefunction probability P. **c**, Topological phase diagram as a function of Zeeman energy E_Z and superconducting phase difference ϕ. Figures **a** and **b** are adapted from Ref [35] and **c** is adapted from Ref [36].

I

INTRODUCTION

2

THEORY

This chapter introduces the four key ingredients for synthesizing topological superconductivity in solid state, namely: one-dimensional nanowires with strong Rashba spin-orbit interaction in proximity to a conventional s-wave superconductor and subjected to an external magnetic field. By creating a system that includes all of these ingredients, it will be shown that Majorana zero modes are formed at the ends of the engineered one-dimensional topological superconductors.

2.1 TWO-DIMENSIONAL ELECTRON GAS

It is difficult to envision the development of condensed matter physics without the discovery of quantum wells (QWs) and the two-dimensional electron gas (2DEG). This platform enabled unprecedented and now hallmark experiments, such as the integer [4] and fractional quantum hall effects [38], as well as, quantized conductance [39]. Electron motion within a QW is confined by a potential that restricts motion in the growth direction, while leaving free motion in a two-dimensional plane. Quantum wells are usually grown by molecular beam epitaxy (MBE) that enables atomically precise thin-film growth of single crystalline materials. The high purity of the growth species and ultra-high vacuum growth conditions both facilitate high carrier mobilities and low carrier densities. This enables unimpeded electron motion over micron distances and long characteristic Fermi wavelengths λ_{f}, making QWs ideal for studying quantum systems. Heterostructures, grown by MBE, are highly flexible due to the ability of precise tuning of elemental compositions in a layer-by-layer fashion that allows for custom tailored quantum wells.

To illustrate how confining potentials create a QW, the effect of dimensional reduction on a bulk three-dimensional system is investigated. When the dimensions of a system approach length scales on the same order as the characteristic electronic wavelengths, quantized energy levels will form. The separation between successive energy levels scales as $\Delta E \propto 1/L^2$, where L is an associated length of the system [40]. This principle allows for the construction of low-dimensional systems (0, 1, 2-dimensional) from bulk three-dimensional materials.

Consider a bulk sample defined by lengths $L_{\mathrm{x}}, L_{\mathrm{y}}, L_{\mathrm{z}}$, as shown in the inset of Fig. 2.1a. Bound states will form due to the boundaries of the sample with energies [41],

$$E_{\mathrm{n_i}} = \frac{\pi^2\hbar^2}{2m^*}\left(\frac{\mathrm{n_i}}{L_i}\right)^2 \qquad i = \mathrm{x, y, z} \quad ,$$

where n is an integer representing a principle quantum number and m^* is the effective mass due lattice interactions. The total energy is then $E_{\mathrm{n_x,n_y,n_z}} = \sum_{\mathrm{i}} E_{\mathrm{n_i}}$. The temperature T and chemical potential μ_{c} governs the filling of electrons due to Fermi-Dirac statistics. The chemical potential μ_{c} at zero temperature is termed the Fermi energy E_{F}, where all states below (above) E_{F} are filled (empty) [41].

First, consider a system with $L_{\mathrm{x}} = L_{\mathrm{y}} = L_{\mathrm{z}}$, as shown in Fig. 2.1a. In the case of weak confinement, the separation between energy levels associated with each direction is negli-

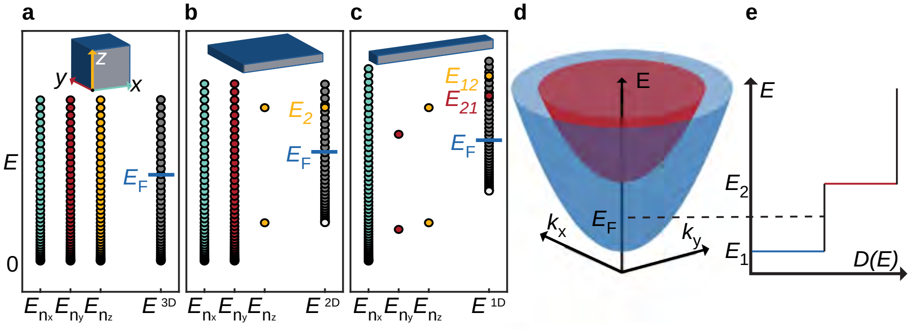

Figure 2.1: **Quantum confinement:** **a**, Energy levels of a bulk three-dimensional sample in the case of weak confinement. Columns $E_{\mathrm{n_i}}$ represent energy levels for $\hat{x}, \hat{y}, \hat{z}$-directions and the column E^{3D} is the kinetic energy of the system. **b**, Confinement along the $\hat{z}$-direction leads to energy level $E_{\mathrm{n_z}}$ quantizations, forming a two-dimensional system when E_{F} is below $E_{\mathrm{n_z}=2}$. **c**, Further confinement along the $\hat{y}$-direction leads to a one-dimensional system. **d**, Momentum dispersion relation for a two-dimensional electron gas showing the first two sub-bands. **e**, The density of states $D(E)$ for a two-dimensional system is constant within each sub-band.

gible and form continuums of states, as indicated by the overlap of the teal, red and yellow markers. Consequently, the electron motion is free in all directions and the kinetic energy of the system recovers the well-known parabolic dispersion,

$$E^{\mathrm{3D}} = \frac{\hbar^2}{2m^*}k^2 \quad k^2 = k_{\mathrm{x}}^2 + k_{\mathrm{y}}^2 + k_{\mathrm{z}}^2 \quad ,$$

where k_i is the electron momenta along the $\hat{i}$-direction and is continuous variables. The energy levels of the system are shown by the grey markers that form a continuum of states.

If the length in the $\hat{z}$-direction is reduced ($L_{\mathrm{z}} \ll L_{\mathrm{x}}, L_{\mathrm{y}}$), the separation between the $E_{\mathrm{n_z}}$ levels increases (see Fig.2.1b). Strong confinement ($L_{\mathrm{z}} \sim \lambda_{\mathrm{f}}$) leads to quantization of the energy levels in the $\hat{z}$-direction. If the Fermi energy E_{F} is below the $E_{\mathrm{n_z}=2}$ (denoted by the yellow dot in $E^{\mathrm{2D}}_{\mathrm{n_z}}$), then the electron motion is restricted to the x-y plane. The energy of the system is,

$$E^{\mathrm{2D}}_{\mathrm{n_z}} = E_{\mathrm{n_z}} + \frac{\hbar^2}{2m^*}k^2, \quad k^2 = k_{\mathrm{x}}^2 + k_{\mathrm{y}}^2 \quad ,$$

stating that for each integer $\mathrm{n_z}$, there is a continuum of two-dimensional states (referred to as a sub-band). The result of the confining potential is a restriction of the electron motion from three to two-dimensions. This reasoning can be continued by further confining electron motion in the $\hat{y}$-direction, leading to a one-dimensional wire with energies (see Fig. 2.1c),

$$E^{1D}_{n_y,n_z} = E_{n_y} + E_{n_z} + \frac{\hbar^2}{2m^*}k_x^2 \quad ,$$

which is useful for creating nanowires from two-dimensional electron gases. In Fig. 2.1c E_F is below both $E^{1D}_{1,2}$ and $E^{1D}_{2,1}$ and the system is one-dimensional.

In Fig. 2.1d the dispersion relation $E^{2D}_{n_z}$ is shown for a two-dimensional system. The Fermi energy E_F is located between the first (E_1) and second sub-band (E_2) forming a 2DEG. The density of states for a strictly two-dimensional system is [42]

$$D(E) = \frac{m^*}{\pi\hbar^2} \quad .$$

Since the density of states for a given sub-band is energy independent, the carrier density n_s can be found by ($T = 0$),

$$n_s = \int_{E_1}^{\mu_c} dE\, D(E) = \frac{m^*}{\pi\hbar^2}\left(\mu_c - E_1\right) = \frac{m}{\pi\hbar^2}E_F = \frac{k_F^2}{2\pi}$$

where k_F is the Fermi momentum. Using conventional Hall bar device geometries enables the measurement of carrier density n_s and mobility μ to be measured (see Chapter 3.3.1). This allows for many of the defining properties of a 2DEG to be calculated [41, 42]:

$$\lambda_f = \frac{2\pi}{k_F}, \quad v_F = \frac{\hbar k_F}{m^*}, \quad E_F = \frac{\hbar^2 k_F^2}{2m^*}, \quad l_e = \frac{\hbar\mu}{e}\sqrt{2\pi n_s} \quad ,$$

where v_F is the Fermi velocity and l_e is the electronic mean free path.

The two-dimensional quantum wells studied in this thesis rely on band-gap alignment to create a confinement potential. This is achieved by sandwiching a layer of InAs (low band gap material) between two layers of either $In_{1-x}Ga_xAs$ or $In_{1-x}Al_xAs$ (higher band gap material). In Fig. 2.2 the conduction band profile of a near surface InAs 2DEG is shown, where an InAs QW is formed due to the InGaAs barriers [17].

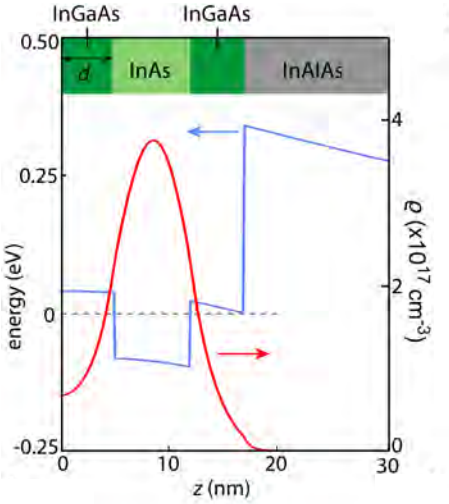

Figure 2.2: **InAs quantum well:** Energy of the conduction band and the 2DEG probability density ρ along the growth direction z calculated by a self-consistent Schrödinger-Poisson solver.This figure is adapted from Ref [17].

2.2 Spin-orbit interaction and the Zeeman effect

Electrons as fundamental fermionic particles have a spin of $\frac{1}{2}$. It was discovered in atomic physics that electron motion about a charged nucleus can interact with the spin of the electron in a process known as spin-orbit interaction (SOI) (shown in Fig. 2.3a). Essentially, SOI is a relativistic effect whereby an electron moving at velocity $\mathbf{v}$ in an electric field $\mathbf{E}$ will experience an additional magnetic field [42],

$$\mathbf{B}_{\text{eff}} = -\frac{\mathbf{v}}{c^2} \times \mathbf{E}$$

in its own frame of reference, due to the motion of the nuclei (depicted in Fig. 2.3b) . This effective magnetic field in turn couples to the spin of the electron through the Zeeman effect, causing the spin splitting observed in the fine structure of atomic emission spectra. A similar effect is observed for electrons travelling in a crystal lattice, where the ions play the role of the atomic nuclei, as illustrated in Fig. 2.3c,d. As it turns out, this motion will result in spin dependent linear shifts in momentum, which lift the spin degeneracy of the energy bands.

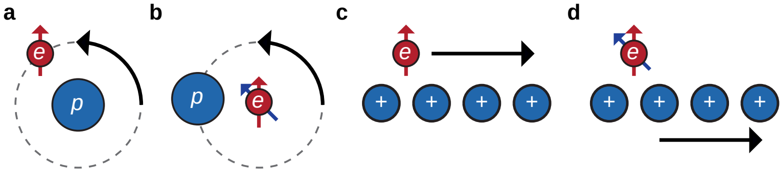

Figure 2.3: **Sources of spin-orbit interaction:** **a**, An electron (e) in an atomic orbital around the charged nucleus (p) will experience the nucleus orbiting itself in its own reference frame **b**. The nucleus generates an effective magnetic field (blue arrow) that couples to the spin of the electron (red arrow), known as spin-orbit interaction. **c,d**, Electrons travelling in a crystal lattice will experience a similar coupling effect due to the charged ions. This figure was influenced by Ref [43].

Conventional QWs are subjected to underlying symmetries that result in spin-degeneracy. Time reversal symmetry enforces that the dispersion relation satisfies $E_\downarrow(k) = E_\uparrow(-k)$, while inversion symmetry of the crystal lattice causes $E(k) = E(-k)$ [42]. If these two symmetries are left unbroken the resulting dispersion relation is doubly degenerate with $E_\downarrow(k) = E_\uparrow(k)$ as shown in Fig. 2.4b. The following sections will discuss how to break these symmetries and what implications this has for engineering topological superconductivity.

2.2.1 ZEEMAN EFFECT

Time-reversal symmetry is broken under an external magnetic field **B**, which causes spin splitting of energy bands. This is known as the Zeeman effect and is given by [42],

$$H_Z = \frac{1}{2} g\mu_B \mathbf{B} \cdot \boldsymbol{\sigma} = \frac{1}{2} g\mu_B B_x \sigma_x \quad ,$$

where g is the Lande g-factor, μ_B is the Bohr magneton and σ_i are the Pauli matrices *. The last term is for the case of a one-dimensional nanowire (see Fig. 2.4a) . Applying a magnetic field B_x causes a Zeeman energy,

$$E_Z = \pm \frac{1}{2} g\mu_B B_x \quad ,$$

---

*Here the σ_i are Pauli matrices: $\sigma_x = \begin{pmatrix} 0 & 1 \\ 1 & 0 \end{pmatrix}$, $\sigma_y = \begin{pmatrix} 0 & -i \\ i & 0 \end{pmatrix}$, $\sigma_z = \begin{pmatrix} 1 & 0 \\ 0 & -1 \end{pmatrix}$.

which opens up an energy gap of $2E_\mathrm{z}$ at $k = 0$ (see Fig. 2.4c). Notice, that due to the spin splitting, the energy bands are spin polarized. This will have important considerations for engineering a spinless system necessary for topological superconductivity.

2.2.2 RASHBA SPIN-ORBIT INTERACTION

In two-dimensional heterostructures, the confinement in growth direction $(\hat{z})$ is a result of the band alignment. It is also responsible for creating a structural inversion asymmetry [44–46]. The confining potential leads to a potential gradient and an electric field $\mathbf{E} = E_0\hat{z}$. The shape of the potential can be tuned either during growth of the quantum well or by an external gate-voltage. Electron motion in the QW experiences a corresponding effective magnetic field $\mathbf{B}_\mathrm{eff}$ due to $\mathbf{E}$, which aligns spin orthogonal to momentum p. This effect is termed the Rashba SOI and is described by the Hamiltonian [42],

$$H_\mathrm{R} = \frac{\alpha_\mathrm{R}}{\hbar}(\sigma_\mathrm{x} p_\mathrm{y} - \sigma_\mathrm{y} p_\mathrm{x}) \tag{2.1}$$

where p is the electron momentum and α_R is the Rashba interaction strength. The case of a one-dimensional nanowire with electron motion along $\hat{x}$ leads to a Rashba Hamiltonian of,

$$H_\mathrm{R}^\mathrm{1D} = -\frac{\alpha_\mathrm{R}}{\hbar}\sigma_\mathrm{y} p_\mathrm{x} \quad .$$

For a Rashba nanowire, the spin-orbit field points in-plane and perpendicular to the nanowire axis. This modifies the energy dispersion of a free particle by [45, 46],

$$E = \frac{\hbar^2}{2m}k^2 \pm \alpha k = \frac{\hbar^2}{2m}(k \pm k_\mathrm{SO})^2 - E_\mathrm{SO}$$

causing a spin-dependent shift of the energy bands in momentum by $k_\mathrm{SO} = \frac{m\alpha_\mathrm{R}}{\hbar^2}$ and down in energy by $E_\mathrm{SO} = m\alpha_\mathrm{R}^2/2\hbar^2$. The effects of Rashba SOI on the energy dispersion are shown in Fig. 2.4d.

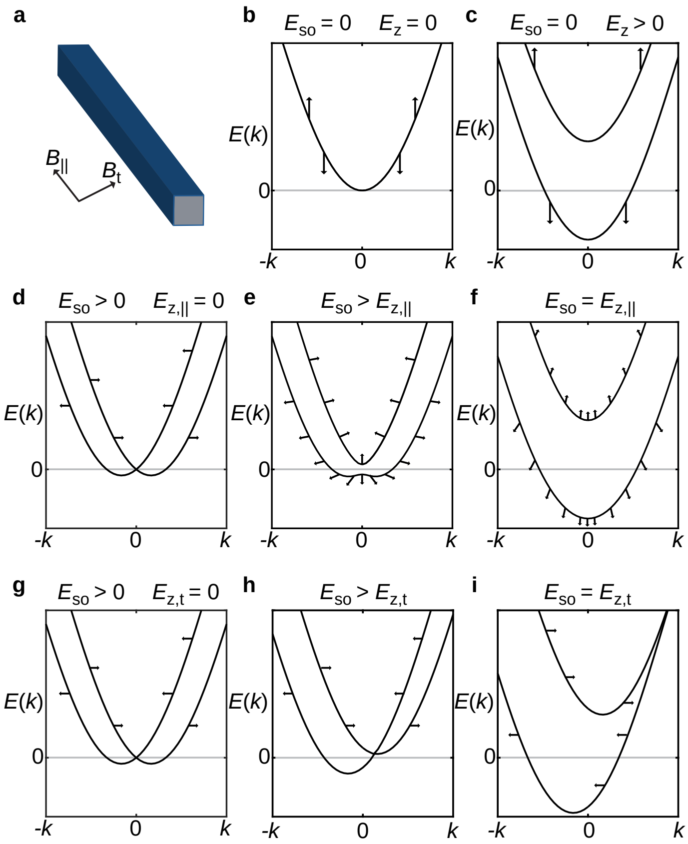

Figure 2.4: **Rashba nanowire:** **a**, Sketch of a one-dimensional nanowire and corresponding external magnetic field parallel ($B_{||}$) and transverse (B_t) to the wire axis. **b**, Energy dispersion calculated from Eq. 2.2 for spin-orbit interaction $E_{so} = 0$ and Zeeman energy $E_z = 0$ causing spin degenerate energy bands. **c**, A finite $E_z > 0$ leads to spin splitting of the bands. **d-f**, Evolution of the energy bands for a Rasbha nanowire in a parallel magnetic field $B_{||}$ (perpendicular to the SOI field). **g-i**, Evolution of the energy bands for a Rasbha nanowire in a transverse magnetic field B_t (parallel to the SOI field). Arrows denote spin orientation dependence on magnetic field and momentum. Energy dispersions were calculated by the python simulations package Kwant [47].

While a Rashba SOI depends on structural properties of the quantum well, bulk properties of the underlaying crystal-lattice structure can also contribute to spin-orbit interactions. Dresselhaus SOI (strength β_{D}) is created by crystal structures lacking an inversion symmetry, such as Zinc-Blende. For InAs QWs, a Rashba contribution is predicted to dominate over Dresselhaus by a factor of four from band structure calculation [48]. Weak antilocalization measurements on near surface InAs quantum wells (similar to the ones investigated in this thesis) without epitaxial Al found that a Rashba SOI dominated by a factor of 5.6 with $\alpha_{\mathrm{R}} = 280$ meVÅ, and $\beta_{\mathrm{D}} = 50$ meVÅ. Recent work on similar InAs QWs showed that the strength of the SOI was sensitive to a gate-voltage [49]. This is expected for Rashba SOI because the Rashba coupling strength is determined by an electric field [46].

We investigated the role of SOI in hybrid superconductor-semiconductor QWs by measuring the magnetic field dependence on the Coulomb blockade peaks of a hybrid Coulomb islands [50]. We found a dominant Rashba-like SOI by varying magnetic field directions and estimated a lower bound of α_{R} = 120 meVÅ for the hybrid system.

2.2.3 THE HELICAL GAP

An interesting competition between the Zeeman effect and Rashba SOI arises when a one-dimensional Rashba nanowire is subjected to an external parallel magnetic field $B_x = B_{||}$. If the external magnetic field is oriented orthogonal to the spin-orbit field, it causes a rotation of the spin direction creating a spin-texture. This system is modeled as,

$$H = \frac{p^2}{2m}\sigma_0 - \frac{\alpha_{\mathrm{R}}}{\hbar}\sigma_{\mathrm{y}} p_{\mathrm{x}} + B_{||}\sigma_{\mathrm{x}} \tag{2.2}$$

where the first term is the kinetic energy, the second term is the Rashba SOI, and the third term Zeeman energy due to the external magnetic field B. Applying a small B causes the spinful bands to mix, leading to an anti-crossing at $k = 0$ and the opening of an energy gap of $2E_{\mathrm{z}}$, as shown in Fig. 2.4e. Around $k = 0$ the spins align along the external magnetic field, while at large k the spins rotate perpendicular due to the momentum dependent Rashba contribution. If the chemical potential is positioned within the Zeeman gap, the electrons spin is locked to its momentum, where for $k > 0$ the spin is $\rightarrow$ and for $k < 0$ spin is $\leftarrow$. This is referred to as the helical state.

If the external magnetic field is applied transverse to the wire, $B_y = B_{\mathrm{t}}$, the field will be aligned with the spin-orbit field. In this system, no spin mixing occurs and no Zeeman gap is opened. The result can be seen in Fig. 2.4g-i, where a tilting of the dispersions is observed.

2.3 SUPERCONDUCTIVITY

A superconductor is a material where below a critical temperature T_c, all electrons within an energy window 2Δ about E_F form pairs with opposite spin and momentum. These pairs behave as bosons and are able to form a charge carrying condensate with zero resistance. A microscopic model for superconductivity was introduced in 1956 by Bardeen, Cooper, and Schrieffer (BCS), where two electrons feel an attractive potential allowing for pair formation [51]. The mechanism responsible for the attractive pairing potential is electron-phonon scattering. This is described by a three step process where an initial electron causes a lattice distortion, increasing the local positive charge density, which causes a subsequent electron to experience a net positive attraction to the first electron. Written in the language of second quantization, the pairing Hamiltonian is [52],

$$H = \sum_{k,\sigma=\{\uparrow,\downarrow\}} \xi_k c^\dagger_{k,\sigma} c_{k,\sigma} + \sum_{k,l} V_{kl} \; c^\dagger_{k,\uparrow} c^\dagger_{-k,\downarrow} c_{-l,\downarrow} c_{l,\uparrow} \quad .$$

The first term is the kinetic energy with $\xi_k = \frac{\hbar^2}{2m}k^2 - \mu_c$ and the second term describes the interaction between electrons with opposite spin and momentum (s-wave pairing). If V_{kl} is negative it will promote the pairing in a spin singlet configuration (s-wave superconductivity). In this system, the ground state has correlated pairs of electrons with a correlation amplitude described by [53],

$$\Delta(\mathbf{r}) = V_n \, F(\mathbf{r}) = V_n \, \langle \psi(\mathbf{r},\uparrow) \mid \psi(\mathbf{r},\downarrow) \rangle$$

where $F(\mathbf{r})$ represents the probability of finding two correlated electrons at a position $\mathbf{r}$. These new composite particles - referred to as Cooper pairs - obey Bose-Einstein statistics, allowing them to condense into the same lowest energy ground-state. The parameter V_n describes the binding strength of the electron pair and depends on the material, temperature and magnetic field. It will be shown below that $\Delta(\mathbf{r})$ is responsible for the energy gap in the quasiparticle spectrum.

2.3.1 QUASIPARTICLE SPECTRUM

The quasiparticle excitation spectrum of a superconductor deviates from the single-particle spectrum of a normal metal due to the presence of an energy gap 2Δ about E_F. Quasiparticle excitations in a superconductor are a coherent mixture of electron and hole states that can be can be written in terms of Bogoliubov operators b as [52] *,

$$b^{\dagger}_{-k,\downarrow} = uc^{\dagger}_{-k,\downarrow} - vc_{k,\uparrow}, \quad b_{k,\uparrow} = vc^{\dagger}_{-k,\downarrow} + uc_{k,\uparrow} \quad , \tag{2.3}$$

where u and v are the coherence factors of the electron-like or hole-like excitations, respectively. The Bogoliubov transformation of Eq. 2.3 diagonalizes the BCS mean-field Hamiltonian when they satisfy the Bogoliubov de Gennes (BdG) equation [54, 55],

$$\begin{pmatrix} H & \Delta \\ \Delta^* & -H \end{pmatrix} \begin{pmatrix} u_k \\ v_k \end{pmatrix} = E_k \begin{pmatrix} u_k \\ v_k \end{pmatrix} \quad ,$$

with $H = \frac{p^2}{2m} + V(r) - \mu_c$ where $V(r)$ is an electrostatic potential. For the trivial case of $\Delta = 0$, the BdG equation describes two decoupled Schrödinger equations - one for electron and one for holes. Turning on $\Delta > 0$, couples the two equations and mixes electrons and holes solutions †. The quasiparticle excitation spectrum is determined by considering a homogeneous system ($V(r) = 0$) and plane-wave eigenfunctions,

$$(u_k, v_k)^{\mathsf{T}} = e^{ik\cdot r}(u_0, v_0)^{\mathsf{T}} \quad .$$

The energy eigenvalues of the BdG equation are [52],

$$E_k = \pm\sqrt{\xi_k^2 + \Delta^2} \quad ,$$

with the electron and hole coherence factors given by,

$$|u_k|^2 = \frac{1}{2}\left(1 + \frac{\xi_k}{E_k}\right), \quad |v_k|^2 = \frac{1}{2}\left(1 - \frac{\xi_k}{E_k}\right) \quad . \tag{2.4}$$

In Fig. 2.5a the coherence factors are shown as a function of kinetic energy ξ_k that is measured with respect to the Fermi energy. For $\xi_k > 0$, the quasiparticle excitations are more electron-like and for $\xi_k < 0$ are more hole-like. Interestingly, if the energy of the quasiparticle excitation is zero, it is described by equal electron and hole components ($|u_k|^2 = |v_k|^2 = 1/2$). This is why MZMs are zero-energy excitations in a topological superconductor.

---

*The Bogoliubons operators commonly use γ notation and are referred to as Bogoliubons. However, here we use b to not confuse with Majorana operators

†Elementary excitations in a superconductor are described by a linear combination of electron and hole operators (see Chapter 1.1)

To understand the role of superconductivity in a one-dimensional nanowire, the system is model as,

$$H_{\mathrm{SC}} = \frac{p_x^2}{2m}\sigma_0 \otimes \tau_z + \Delta\sigma_0 \otimes \tau_x \quad , \tag{2.5}$$

where τ_i is the Pauli matrix acting in particle-hole space. The energy dispersion of this Hamiltonian is plotted in Fig. 2.5b. First, it is noticed that the particle-hole symmetry introduced by the BdG Hamiltonian doubles the number of solutions (comparing teal and black curves). By turning on electron pairing ($\Delta > 0$), the appearance of an energy gap Δ in the spectrum (red curve) is observed.

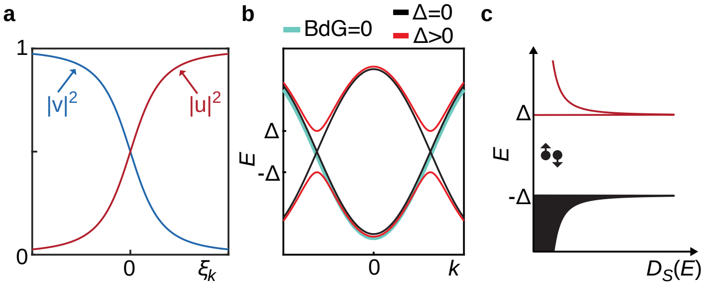

Figure 2.5: **Quasiparticle spectrum:** **a**, Electron-like (u) and hole-like (v) coherence factors as a function of electron energy ξ_k measured with respect to E_{F}. **b**, Superconducting quasiparticle excitation spectrum. For $\Delta > 0$ a gap opens about E_{F}. **c**, Quasiparticle density of states of a superconductor revealing the energy gap Δ.

This energy gap is reflected in the density of states of a superconductor $D_S(E)$ given by [52],

$$g_S(E) = \frac{D_S(E)}{D_N} = \begin{cases} \frac{E}{\sqrt{E^2 - |\Delta|^2}}, & \text{if } |E| \geq \Delta \\ 0, & \text{otherwise} \end{cases} \quad ,$$

where D_N is the constant density of states in the normal state of the metal ($T > T_c$). The density of states is plotted in Fig. 2.5c. For $E < \Delta$ there is zero density of quasiparticles states, and at $E = \Delta$ the density of states diverges giving the BCS coherence peaks. The energy gap is related to the critical temperature by $\Delta(T = 0) = 1.76 k_{\mathrm{B}} T_c$. The superconductor used in this thesis was exclusively Al, which has a bulk $T_c \sim 1.2$ K giving $\Delta = 180\ \mu$eV [52].

2.3.2 Tunneling spectroscopy

In 1960, Giaever used a thin, oxide film to form a tunnel barrier between a normal metal and a superconductor that permitted the superconducting energy gap to be resolved. He was awarded the 1973 Nobel prize in physics for this effort [56]. This experimental measurement technique is termed tunneling spectroscopy. The system is comprised of a normal lead (N) separated from a superconducting lead (S) by a tunnel barrier (I), or more commonly referred to as N-I-S tunneling spectroscopy. Shortly after Giaever's discovery, tunnel junctions formed from two superconductors, separated by a thin oxide, were studied by separately by Giaever and by Nicol, Shapiro and Smith, showing the appearance of a 2Δ energy gap [57]. Interestingly, the original S-I-S paper showed the first experimental evidence of a zero-voltage current (supercurrent), but they did not draw attention to it. These results prompted Josephson to thinking about tunneling effects between two superconductors, which led to his discovery of the famous Josephson effect.

Giaever used a tunnel barrier as a spectroscopic tool that allowed him to measure the superconducting energy gap. In the tunneling regime, a current flowing between two metals is proportional to the density of occupied states in one lead and to the density of unoccupied states on the other. Consider a system similar to Giaever's experiment, where a N-lead with a constant density of states D_N is separated by a tunnel barrier from another lead with an unknown density of states D_2. The differential conductance G as a function of source-drain bias voltage V_{sd} is [52, 53],

$$G(V_{\mathrm{sd}}) = \frac{dI}{dV_{\mathrm{sd}}} = G_0\, D_N\, D_2(eV_{\mathrm{sd}}) \quad ,$$

where I is the current resulting from the applied bias voltage, and G_0 is the conductance quantum following from Landauer theory (see appendix B for further details). Therefore, measuring the tunneling differential conductance G gives spectroscopic information about the unknown density of state $D_2(eV_{\mathrm{sd}})$. For instance, consider that second lead is a BCS superconductor. The corresponding differential conductance is,

$$G(V_{\mathrm{sd}}) = G_0 D_N\, g_S(eV_{\mathrm{sd}})$$

as observed by Giaever. The differential conductance is readily available by employing standard low frequency lock-in techniques. However, in contrast to Giaever's experimental setup, in this thesis tunnel barriers are formed by electrostatic depletion of the 2DEG into the tunneling regime $G \ll 2e^2/h$.

2.3.3 ANDREEV REFLECTION

The superconducting proximity effect describes the process of superconducting order leaking into another material [53]. This effect plays an important role in modern quantum devices. The concept places a material system exhibiting interesting attributes (say spin-orbit interactions or ferromagnetism) in close proximity to a superconductor to inherit the pairing correlations. These two materials form a unique hybrid system with properties from both materials [58]. In the following discussion, the basis for proximity effect in semiconducting systems is introduced.

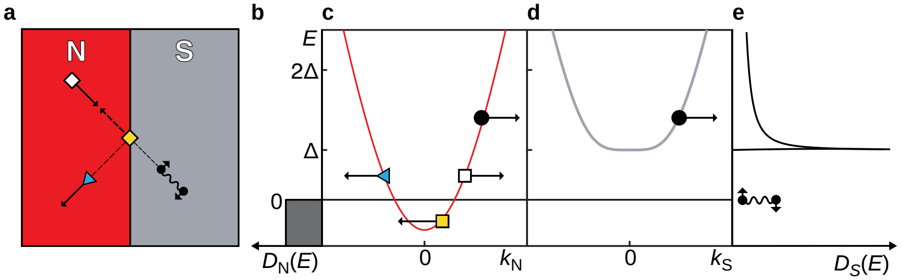

Figure 2.6: **Andreev reflection:** **a**, Real-space illustration of the transport mechanisms occurring at a semiconductor-superconductor (N-S) interface. **b,e**, Density of states in N (**b**), and S (**e**). **c,d**, Energy dispersion relation in N (**c**), and in S (**d**). Arrows represent different transport mechanisms. See text for details.

The superconducting proximity effect can be understood by considering a system where a normal semiconductor (N) with a constant density of states D_N is placed in contact to a superconductor (S) with density of states $D_S(E)$ (see Fig. 2.6b and e). Figure 2.6c and d show the dispersion for the normal state and the superconducting state, respectively.

Consider an electron with energy E incident the N-S interface depicted by the white square in Fig. 2.6a. Three different transport mechanisms are now possible [41, 53, 54, 59]. 1) If an electron in the normal metal is incident to the N-S interface with an energy $E > \Delta$ and momentum $+k$, the electron is transmitted through the N-S interface by converting to a quasiparticle in S at the same energy (see black circles in Fig. 2.6c and d). 2) If the energy of the electron is $E < \Delta$, there are no quasiparticle states in S at these energies and transport appears to be blocked. What transpires is a process known as Andreev reflection, where the S accepts both the incident electron at $(+k, \uparrow)$ and an additional electron with $(-k, \downarrow)$ to form a Cooper pair [60]. Due to momentum and charge conservation, a hole must be reflected in the normal metal with $(+k, \uparrow)$ at $-E$. More plainly stated, an incident electron is retro-reflected from the interface as a hole, thereby transferring a charge of $2e$ into the superconductor in the form of a Cooper pair. 3) If there is a potential barrier at the N-S interface, specular reflection can occur, where an electron is reflected with $-k$ (see teal triangle in Fig. 2.6c).

The Andreev reflection process places specific constraints on the retro-reflected hole. The direction of the reflected hole initially appears to be incorrect, but considering that the group velocity is given by $v_k = \frac{1}{\hbar}\nabla_k E(k)$, then the sign of the group velocity is the opposite to that of the wave vector for holes [41, 54]. For electrons, the wave vector and the group velocity are in the same direction. Therefore, the reflected hole follows the same path as the electron, but in the opposite direction (retro-reflection). This backtracking is only exact if the energy of the incident electron is $E = 0$. If $|E| > 0$ then there is a momentum difference between the electron and the retro-reflected hole [41, 53],

$$\delta k = k_e - k_h = \frac{E}{\hbar v_{\mathrm{F}}} \quad ,$$

which is absorbed by the Cooper pair [40]. An estimate of the length over which the incident electron and retro-reflected hole become out of phase ($L\,\delta k = \pi$) is given by,

$$L = \frac{\pi}{\delta k} = \frac{\hbar v_{\mathrm{F}}}{\pi E} \quad .$$

This allows for the superconducting coherence length to be defined for the case of $E = \Delta$ by,

$$\xi_0 = \frac{\hbar v_{\mathrm{F}}}{\pi \Delta} \quad .$$

This is the same result as the BCS coherence length [52], except that the Fermi velocity corresponds that of semiconductor.

We have neglected in the above discussions that the superconducting lead can have a phase $\Delta e^{i\phi_s}$. The phase shift acquired from an Andreev reflection will depend on the phase of the superconducting lead ϕ_s and on the energy of the incident electron or hole as [40, 55],

$$\varphi_{e(h)} = \arccos\left(\frac{E}{\Delta}\right) \pm \varphi_S \quad .$$

This has important consequences in the next section for the discussion of a normal region confined by two superconducting leads.

The Andreev reflection process discussed above is greatly simplified. In a realistic system, an effective barrier increases the probability of secular reflections, due to Fermi velocity mismatch, disorder, or remnant oxides, etc. A more realistic system was modeled in the seminal work of Blonder, Tinkham, and Klapwijk (BTK), where an effective barrier was introduced at the N-S interface [59]. This barrier, formally known as the Z parameter, showed that for Z = 0, the Andreev reflection probability was unity. Increasing the barrier height caused an increase in the probability of normal reflections, while the probability of Andreev reflections decreased.

An ideal system for studying the BTK model is a quantum point contact (QPC), which controls the amount of open transport channels. In a ballistic N-QPC-N geometry, conductance through the QPC constriction occurs in steps with integer values of $2e^2/h$; a signature of quantized conductance [39]. In the case of a N-QPC-S, a signature of perfect Andreev reflection is conductance steps with integers of $4e^2/h$, reflecting the charge transfer of $2e$ [61, 62]. However, in the presence of a barrier, the height of the conductance steps will only reach a fraction of $4e^2/h$, due to the enhanced probability of normal reflection. Chapter 3 shows that a simple QPC pinch-off measurement can be used to assess the quality of the interface transparency.

2.3.4 ANDREEV BOUND STATES

A semiconductor Josephson junction is constructed by confining a N region by two S leads, forming an S-N-S junction, as depicted in Fig. 2.7a. The normal region is usually referred to as a weak link. For electrons propagating in N, Andreev reflections are possible at both N-S interfaces. Therefore, quasiparticles in the weak link with an energy $E < \Delta$ are confined by the superconducting leads. As discussed, bound states are expected when confinement is strong. The superconducting gap profile of the junction is introduced as,

$$\Delta(x) = \begin{cases} \Delta e^{i\phi_1} & \text{for } x < L_1, \\ 0 & \text{for } L_1 < x < L_2, \\ \Delta e^{i\phi_2} & \text{for } x > L_2 \end{cases} ,$$

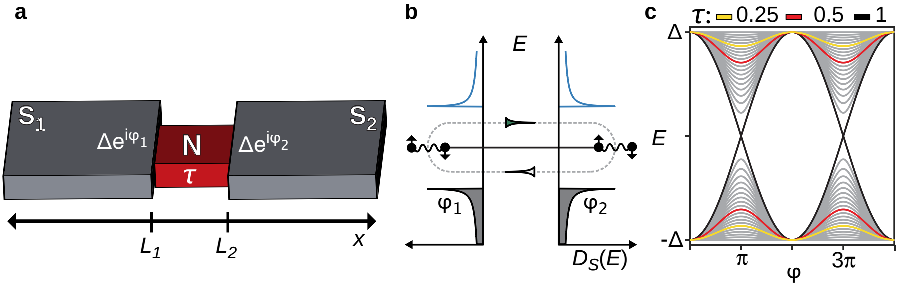

Figure 2.7: **Andreev bound states:** **a**, Sketch of a superconductor-normal-superconductor (S-N-S) Josephson junction. **b**, Two superconducting density of states confine the normal region forming bounds states due to Andreev reflections. **c**, Andreev bound state energy E_{ABS} as a function of phase difference ϕ across the junction. Colours represent different transmissions τ.

with a superconducting phase difference $\phi = \varphi_1 - \varphi_2$ across the junction of length $L_j = L_2 - L_1$. A right moving electron traversing the weak link will undergo Andreev reflection once it encounters S_2 and be reflected as a hole. This left moving hole is now incident on S_1 and will undergo a further Andreev reflection back to a right moving electron. This process is sketched in Fig. 2.7b. The total phase accumulated during a cycle is,

$$\varphi_{\mathrm{tot}} = -k_{\mathrm{h}} L_j + \arccos\left(\frac{E}{\Delta}\right) + \varphi_1 + k_{\mathrm{e}} L_j + \arccos\left(\frac{E}{\Delta}\right) - \varphi_2 \quad .$$

The phase shift is similar to the case for Andreev reflection, but with the added dynamical phase $k_{\mathrm{e(h)}} L_j$ acquired traversing the weak link. The total dynamical phase acquired is $dk L_j = \frac{EL_j}{\hbar v_{\mathrm{F}}} = \frac{L_j}{\xi_0}\frac{E}{\Delta}$. Bound state solutions arise when $\varphi_{\mathrm{tot}} = 2\pi$ giving [54],

$$\frac{E}{\Delta}\frac{L_j}{\xi_0} = \phi + 2\arccos\left(\frac{E}{\Delta}\right) - 2\pi n \quad \text{for integer n} \quad .$$

These solutions are referred to as Andreev bound states (ABS). When the junction length is short compared to the superconducting coherence length $L_j \ll \xi_0$, the dynamic phase contribution is negligible and the two lowest ABS energies are,

$$E_{\mathrm{ABS}} = \pm\Delta\cos(\varphi/2) \quad .$$

This is the case for reflectionless ballistic transport through the weak link, as plotted by the black curve in Fig. 2.7c. If impurities are present, scattering opens an avoided crossing at $\phi = \pi$ and the energy of the ABSs are described by [63],

$$E_{\text{ABS}} = \pm\Delta\sqrt{1 - \tau\sin^2(\varphi/2)}, \quad 0 \leq \tau \leq 1$$

where τ is the transmission through the impurity. The ABS energy-phase relation is plotted in Fig. 2.7c for different transmissions. These ABS are responsible for transferring a charge $2e$ across the Josephson junction, leading to a supercurrent flow. At zero temperature each ABS carries a supercurrent

$$I_{\text{ABS}} = \frac{2e}{\hbar}\frac{dE_n}{d\phi} \quad .$$

At finite temperature, the total supercurrent of an S-N-S junction is a sum of all the current carrying ABS and is given by [41, 53],

$$I_{\text{s}} = \frac{2e}{\hbar}\sum_{n=0}^{m}\frac{dE_n}{d\phi}\tanh\left(\frac{E_n}{2k_{\text{B}}T}\right) \quad ,$$

where $n = 1, 2, 3...m$ and m is the total number of ABS (open transport channels). As a consequence, ABS with a higher transmission will lead to a larger supercurrent flow. In the next section, the Josephson effect and flux quantization will be introduced to understand how to tune the phase difference ϕ across the weak link when embedded into a superconducting ring.

2.3.5 JOSEPHSON EFFECT

The story of the Josephson effect starts in the 1960s when Josephson famously postulated that electrons can tunnel across a barrier in pairs [64]. It was formerly thought such a process should be suppressed since if the probability of one electron to tunnel is τ then the probability of two electrons is τ^2, a very small number [65]. Josephson argued that the Cooper pair wavefunction is phase coherent and therefore the amplitudes need to be added before squaring. Moreover, it is not single electrons that tunnel, but Cooper pairs themselves with a probability comparable to single electrons. To understand the Josephson effect, the Ginzburg-Landau formalism of superconductivity must first be discussed.

The phenomenological theory of Ginzburg-Landau states that the wavefunction ψ describing the Cooper pair condensate is [52, 66],

$$\psi(\mathbf{r}) = \sqrt{n_s(\mathbf{r})}e^{i\theta(\mathbf{r})} \quad .$$

This is a global wavefunction describing the entire Cooper pair condensate of a superconductor, where $n_s(\mathbf{r})$ is the density of Cooper pairs and θ is the phase of the superconductor. Since this is a macroscopic wavefunction, the phase is restricted to only allow single-valued solutions of ψ. The absolute phase is not an observable quantity, but as Josephson realized the phase difference between two superconductors is measurable.

If there exists a gradient of the phase θ, a supercurrent density $\mathbf{J}_\mathrm{S}$ will flow given by [66],

$$\Lambda_\mathrm{L}\,\mathbf{J}_\mathrm{S}(\mathbf{r}) = \left(\frac{\hbar}{q^*}\nabla\theta(\mathbf{r}) - \mathbf{A}(\mathbf{r})\right), \quad \Lambda_\mathrm{L} = \frac{m^*}{q^{*2}n_s^*\hbar}$$

where $q^* = 2e$ and $m^* = 2m_e$ are the charge and mass of a Cooper pair, $\mathbf{A}$ is the magnetic vector potential and Λ_L is the London coefficient.

Consider the case where two independent superconductors (S_1 and S_2) are connected via a weak link in the absence of any vector potentials as depicted in Fig. 2.7a. Each of the two superconductors has a phase θ_i. The phase difference across junction can be described by,

$$\phi = \int_1^2 \nabla\theta \cdot d\mathbf{l} = \theta_2 - \theta_1 \quad .$$

This lead Josephson to postulate that the current density, or simply the current I (for a homogeneous current density), is a function of the phase difference between the two superconductors $I(\phi)$ [64, 67]. Furthermore, since the phase difference can only be defined up to a difference of $2\pi n$ for integer n, then the current is a periodic function, such that $I(\phi) = I(\phi+2\pi n)$. Finally, he argued that a common phase between the superconductors should not result in a current flow $I(\phi = 0) = 0$. Based on these observations he concluded that [67],

$$I_s(\phi) = I_c \sin\phi \quad , \tag{2.6}$$

where I_c is the critical current determined by the coupling strength of the two superconductors . For a ballistic junction the critical current is given by [68],

$$I_c = \frac{Ne\Delta}{\hbar}$$

where N is the number of transport channels. Remarkably, this suggests that a zero-resistance supercurrent will flow between two superconductors provided that there is a phase difference ϕ between them. The Josephson effect was experimentally first observed by Anderson and Rowell [69].

2.3.6 Flux quantization

If there exists a hole within a superconductor, then the total amount of flux threading the hole is quantized in units of h/q^*. As it turned out, flux quantization experiments were some of the most convincing early evidence for the existence of Cooper pairs. These experiments showed that $q^* = 2e$ by observing flux quantization in units of $\Phi_0 = h/2e = 2.07 \times 10^{-15}$ Wb $\sim$ 2.07 μm^2 mT [70, 71].

Flux quantization can be understood by considering two superconductors that are connected into contour C enclosing an area S. Integrating the current density about the contour gives *,

$$\oint_C \Lambda_L \mathbf{J}_S \cdot d\mathbf{l} = \frac{\hbar}{2e} \oint_C \nabla\theta \cdot d\mathbf{l} - \int_S \mathbf{B} \cdot d\mathbf{s} \quad , \tag{2.7}$$

where $\mathbf{B}$ is the magnetic field threading the area S. The phase gradient term is,

$$\oint_C \nabla\theta \cdot d\mathbf{l} = \theta(r_2) - \theta(r_1) \quad .$$

where r_1 and r_2 define the path of the contour. The wavefunction ψ must be single-valued, meaning that the start and end points enclosing this contour must have the same value [66]. This implies that for $r_2 \rightarrow r_1$, the path is closed and, therefore, $\theta(r_2) - \theta(r_1) = 0$. However, since θ is only specified modulo 2π $(\theta_n = \theta_0 + 2\pi n)$ it is found that,

$$\frac{\hbar}{2e} \oint_C \nabla\theta \cdot d\mathbf{l} = \frac{\hbar}{2e} 2\pi n = n\Phi_0$$

where $\Phi_0 = \frac{h}{2e}$ is the superconducting flux quantum and n is an integer. Setting this into

---

*Here we use the Stoke's theorem $\oint_C \mathbf{A} \cdot d\mathbf{l} = \int_S \mathbf{B} \cdot d\mathbf{s}$

Eq. 2.7 gives [66],

$$\underbrace{\oint_C \Lambda_L \mathbf{J}_S \cdot d\mathbf{l} + \int_S \mathbf{B} \cdot d\mathbf{s}}_{\text{Fluxoid}} = n\Phi_0 \quad . \tag{2.8}$$

The fluxoid condition states that for any multiply connected superconductors, the fluxoid threading the hole is quantized in units of the superconducting flux quantum. If the superconductor thickness is much greater than the London penetration depth λ_L, then a contour deep inside a superconductor can be chosen where $\mathbf{J}_s = 0$. This simplifies Eq. 2.8 to,

$$\int_S \mathbf{B} \cdot d\mathbf{s} = n\Phi_0 \quad .$$

This states that the magnetic flux threading a superconducting loop is quantized in integers of $\frac{h}{2e}$. It is noted that the external magnetic field B does not need to be quantized. Only the contributions of both the external and internal fluxes (resulting from the flowing supercurrent) are quantized (see Eq. 2.8).

2.3.7 PHASE BIASING

Figure 2.8a illustrates a device that enables an external magnetic field to tune the phase difference across a weak link. This device is commonly referred to as a RF Superconducting QUantum Interference Device (SQUID). The phase difference across the weak link is $\phi = \theta_2 - \theta_1$. Due to flux quantization,

$$\phi = \int_S \mathbf{B} \cdot d\mathbf{s} = -2\pi \frac{\Phi}{\Phi_0} \quad , \tag{2.9}$$

where Φ is the total flux threading the loop. Substitution of this into the Josephson Eq. 2.6 states that the supercurrent flowing across the junction is given by [52],

$$I = -I_c \sin\left(2\pi \frac{\Phi}{\Phi_0}\right) \quad .$$

The total flux Φ in the loop is the sum of the applied flux $\Phi_{ext} = B_\perp S$ and the flux induced by the screening current $\Phi_s = L\,I$, where L is the self inductance of the loop [52],

$$\Phi = \Phi_{ext} - LI_c \sin\left(2\pi \frac{\Phi}{\Phi_0}\right) \quad .$$

Therefore, the phase difference ϕ across the S-N-S junction can be tuned by applying a perpendicular magnetic field $B_\perp$ as given by Eq. 2.9.

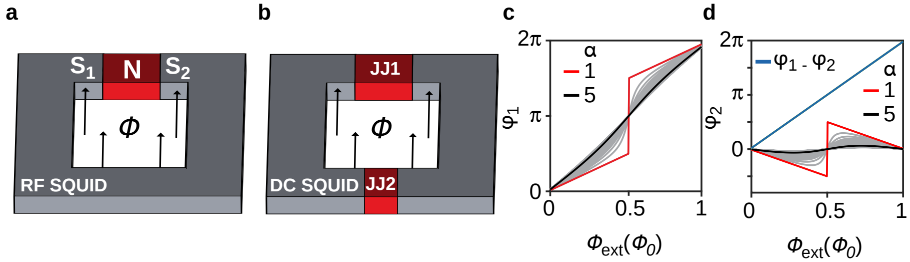

Figure 2.8: Phase biasing: Sketch of a RF SQUID (**a**), and a DC SQUID (**b**). **c,d**, Phase biasing a DC SQUID. Phase difference ϕ_1 across junction 1 (**c**) and ϕ_2 across junction 2 (**d**) for different critical current asymmetries $\alpha = I_{c_2}/I_{c_1}$ for a DC SQUID. Grey curves are for $1 < \alpha < 5$.

This device geometry does not permit for a transport measurement of the critical current because the S-N-S junction is shorted by the superconducting loop. This limits its experimentally applications. However, this geometry enables a simple method of phase biasing a Josephson junction that is measured by tunneling spectroscopy (see chapter 4.3).

If both critical current measurements and phase biasing are needed experimentally, an alternative geometry can be used that is based on two Josephson junctions JJ1 and JJ2 connected in parallel. This geometry is referred to as a DC SQUID and is illustrated in Fig.2.8b. This device geometry was selected for the experiments discussed in chapter 10. Since the weak links are semiconductor based, it is possible to open and close the superconducting loop by controlling a gate voltage to deplete the 2DEG. This allows for the independent interrogation of each junction. However, it is possible for phase to be dropped across both junctions and therefore precautionary measures must be taken when designing devices.

In a DC SQUID, the phase differences of JJ1 ϕ_1 and of JJ2 ϕ_2 are constrained by flux quantization giving [52, 66],

$$\phi_1 - \phi_2 = 2\pi\frac{\Phi}{\Phi_0} \quad , \tag{2.10}$$

where, for simplicity, the kinetic and geometric inductances are assumed to be negligible. The total current through the DC SQUID is the sum of the contributions from each junction as [52, 66],

$$I = I_{c_1}\sin\left(\phi_1\right) + I_{c_2}\sin\left(\phi_2\right) = I_{c_1}\sin\left(\phi_2 + 2\pi\frac{\Phi}{\Phi_0}\right) + I_{c_2}\sin\left(\phi_2\right) \quad . \tag{2.11}$$

When a finite Φ_{ext} is applied, a screening circulating current J will be induced,

$$J = \frac{1}{2}\left(I_{c_2}\sin\left(\phi_2\right) - I_{c_1}\sin\left(\phi_1\right)\right) \quad .$$

In a conventional DC SQUID configuration, the critical currents I_{c_i} of each junction are symmetric ($I_{c_1} = I_{c_2}$). In this configuration, however, the phase difference across each junction changes abruptly at $\Phi = \frac{1}{2}\Phi_0$ due to the screening current changing sign. As a consequence, the phase difference across the both junctions does not reach π.

For the devices geometry reported on in Chapter 10, it is important to allow for the applied external flux Φ_{ext} to tune the phase difference across JJ1 $\phi_1 \sim \pi$. This issue is resolved by introducing an asymmetry $\alpha = I_{c_2}/I_{c_1}$ between the critical currents of JJ1 and JJ2 †. The phase differences ϕ_1 and ϕ_2 as a function of Φ_{ext} are determined by self-consistently solving Eq. 2.11 constrained by Eq. 2.10 to maximize I *.

Figure 2.8c,d displays the phase difference ϕ_1 and ϕ_2 as a function of Φ_{ext} for different values of asymmetry. The case of symmetric critical currents ($\alpha = 1$) is shown by the red curves, illustrating the abrupt change in ϕ_1 and ϕ_2. Increasing the asymmetry ($\alpha > 1$) reduces the abruptness as shown by the grey curves. The devices in chapter 10 were designed with an asymmetry of $\alpha \sim 5$. Figure 2.8c and d show the case for $\alpha \sim 5$ (black curves), where the asymmetry allows for Φ_{ext} to continuously control ϕ_1 from 0 to π. Therefore, introducing an asymmetry enabled phase biasing in a DC SQUID. Similar setups have been used by other groups [72] and have been proposed as a measurement scheme to detect Majorana zero modes in a topological Josephson junction [73].

2.4 MAJORANA ZERO MODES

The following section will introduce how to engineering topological superconductivity and the behaviour of MZMs at the ends of one-dimensional nanowires. This will require incorporating aspects from the previous sections of this chapter.

---

† A large asymmetry can be thought as approaching the limit of a RF SQUID.

* A similar result is found when only a circulating current is present by setting $I = 0$ in Eq. 2.11 and solving for ϕ_1 constrained to minimize the Josephson energy.

The Kitaev chain is a common entry point to gain perspective on the fundamental properties of Majorana zero modes (MZMs) [11, 22]. Although based on a rather simplistic toy model, the results are useful to understand the experimental signatures of MZMs. Essentially, the Kitaev chain is a tight-binding model for a spinless superconductor, where the standard fermionic operators are decomposed into Majorana operators (see Chapter 1.1). By varying the model parameters, a topological phase can be engineered where the two outermost Majoranas on either end of the chain no longer appear in the Hamiltonian. This pair of Majorana modes is therefore 1) fixed to zero energy, 2) obey the predicted behaviour of Majorana operators γ and 3) appear in one-dimensional nanowires at the boundary between topological and trivial regions. The topological phase is tuned by the chemical potential, allowing for the boundary between trivial and topological to be defined by a gate voltage. Finally, the model suggests that in order to achieve this theoretical system, a p-wave superconducting phase of matter is needed. The challenge is finding a suitable material system that hosts these quasiparticle excitations.

This challenge was addressed by Fu and Kane in 2008, where they devised a mechanism for creating p-wave pairing in the laboratory [14]. Their proposal relies on the combinations of a topological insulator with conventional s-wave superconductivity induced by proximity effect, mitigating the need for resorting to bulk materials. This mechanism was extended to one-dimensional superconductor-semiconductor hybrids, which are discussed here [15, 16]. Elements of the previous sections will be used to understand this system, namely: 1) one-dimensional nanowires, 2) strong spin-orbit coupling, 3) conventional s-wave superconductivity induced by proximity effect, and 3) an external magnetic field for a Zeeman energy. This system is referred to as a Majorana wire.

A clear starting point to create a spinless superconductor is to spin polarize the electrons by applying an external magnetic field (see Section 2.2.1). This causes the bands to spin split and opens a Zeeman gap. If the Fermi energy is positioned within this Zeeman gap, then only one spin species can contribute to transport. This renders the system effectively spinless. However, conventional proximity effect relies on s-wave pairing, which is incompatible with a spinless system. This complication is overcome by introducing Rashba spin-orbit interaction to rotate the spin direction, allowing for superconductivity to leak into the semiconductor (see Section 2.2.2). The combination of Zeeman energy E_Z and spin orbit energy E_{so} in a s-wave proximitized nanowire allows for a topological phase to be engineered.

To illustrate the role of each of these energies, we consider a model commonly referred to as the Oreg-Lutchyn model for a one-dimensional Rashba nanowire coupled to a proximal s-wave superconductor and with an applied magnetic field [15, 16],

$$H = \int dx\ \Psi^\dagger \mathcal{H}_{\mathrm{BdG}} \Psi, \quad \Psi^\dagger = (\psi_\downarrow^\dagger, \psi_\uparrow^\dagger, \psi_\uparrow, -\psi_\downarrow) \tag{2.12}$$

where Ψ are the Nambu spinners and $\mathcal{H}_{\mathrm{BdG}}$ represents the 4 x 4 Oreg-Lutchyn Hamiltonian,

$$\mathcal{H}_{\mathrm{BdG}} = \underbrace{\left(\frac{p_x^2}{2m^*} - \mu\right)\sigma_0 \otimes \tau_z}_{\text{Kinetic}} - \underbrace{\frac{\alpha_{\mathrm{R}}}{\hbar} p_{\mathrm{x}} \sigma_{\mathrm{y}} \otimes \tau_{\mathrm{z}}}_{\text{Rashba}} + \underbrace{B_{\mathrm{x}} \sigma_{\mathrm{x}} \otimes \tau_0}_{\text{Zeeman}} + \underbrace{\Delta \sigma_0 \otimes \tau_x}_{\text{Superconductivity}} \quad . \tag{2.13}$$

The Hamiltonian is similar to the helical gap model introduced in Section 2.2.3, but modified to include superconductivity (as discussed in Section 2.3.1). Figure 2.9a-c, summarizes the roles of each of the three ingredients on the dispersion of the one-dimensional nanowire. Figure. 2.9a depicts the energy bands with superconductivity and without Rashba SOI or magnetic field, where a gap Δ is opened around E_{F}. Turning on Rashba SOI shifts the parabolic bands by $k_{\mathrm{SO}} = \pm\frac{m\alpha_{\mathrm{R}}}{\hbar^2}$ (see Figure. 2.9b). Applying a magnetic field spin splits the bands and tilts the spin towards the direction of the applied field (see Figure. 2.9c). The magnetic field is most effective at low k, where Rashba SOI is weak. Experimentally, it is difficult to independently control either Δ or α_R, since they strongly dependent on the material system, while the magnitude and direction of the external magnetic field is controlled with a vector magnet. Therefore, the topological phase transition is illustrated as a function of magnetic field.

Figure 2.9d-f, displays the evolution of the energy dispersion from topologically trivial to non-trivial by varying the Zeeman energy through a critical energy $E_{\mathrm{Z,c}}$. For $E_{\mathrm{Z}} < E_{\mathrm{Z,c}}$ a minimum is observed at $k = 0$ that can be brought to $E = 0$ when $E_{\mathrm{Z}} = E_{\mathrm{Z,c}}$. At this point the induced superconducting gap is closed, and signifies a transition to the topological phase. The condition for the topological phase transition is,

$$E_{\mathrm{Z,c}} = \sqrt{\mu^2 + \Delta^2} \quad ,$$

where for $E_{\mathrm{Z}} > E_{\mathrm{Z,c}}$ the topological gap opens. In a finite-sized system, MZMs will appear at the boundaries between the topological trivial and non-trivial phases.

The eigenvalue problem of Eq. 2.13 is calculated by discretizing the Hamiltonian for a Majorana wire of finite length L to understand how the system parameters affect the properties

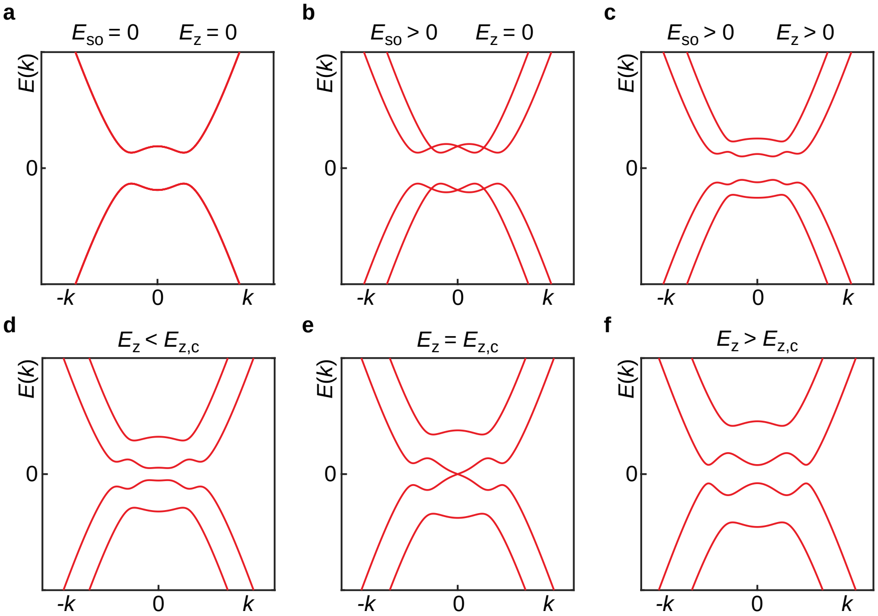

Figure 2.9: **Topological transition:** **a**, Energy dispersion calculated for the case of $\Delta > 0$ (**a**), $E_{SO} > 0$ (**b**), and $E_Z > 0$ (**c**). **d-f**, Zeeman energy induced topological phase transition, where for $E_Z > E_{Z,c}$ there is an inverted band structure. Energy dispersions were calculated from for Eq. 2.13 using a python simulations package Kwant [47].

of the MZMs and their expected transport signatures. The energy eigenvalues are calculated using a tight-binding simulation package Kwant for different system parameters [47].

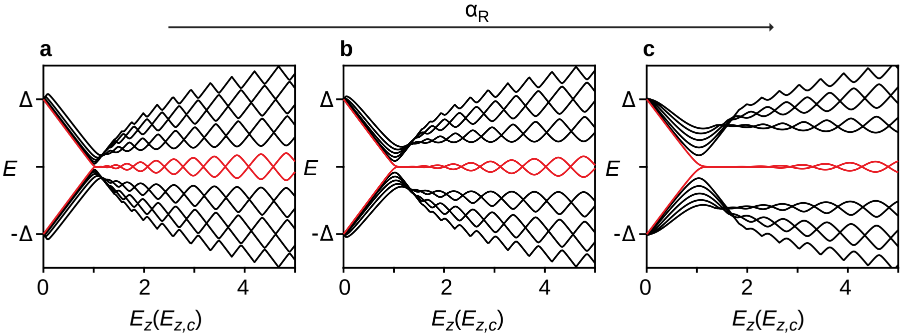

Figure 2.10: **Majorana wire spectrum: a-c**, Eigenvalue spectrum as a function of Zeeman energy for increasing Rashba spin-orbit strength α_R. For $E_Z > E_{Z,c}$ the system is in the topological phase with MZMs at the ends of the Majorana wire. Increasing α_R leads to a larger topological gap. Simulation parameters: $\mu = 0$, $\Delta = 200$, $L = 50$ and $\alpha = 50$ (**a**), 100 (**b**), 200 (**c**).

Figure 2.10a plots the energy spectrum of a Majorana wire as a function of E_Z. For low increasing Zeeman energy, the energy levels decrease towards $E = 0$. At $E_Z > E_{Z,c}$ the superconducting gap is closed and for increasing E_Z the gap reopens signifying the transition to the topological phase. Due to the finite size of the Majorana wire this transition coincides with the appearance of two MZMs (coloured in red in Fig. 2.10a) that are located on either end of the Majorana wire [74]. The strength of the Rashba interaction is increased in Fig. 2.10b and c, leading to an increase in the energy difference between the MZMs and the first excited state. This energy difference is referred to as the topological gap, granting the topological protection of quantum information stored in MZMs. The size of the topological gap is given by [75],

$$\Delta_{\text{topo}} = \frac{\alpha_R \Delta}{B} \quad .$$

It is observed that not only is a magnetic field needed to drive the system into the topological phase, but it also reduces the size of the topological gap. To increase the size of the topological gap either the magnetic field can be reduced by increasing the effective g-factor or by increasing the Rashba interaction strength α_R (see Fig. 2.10) or the size of the induced superconducting gap Δ. The majority of these parameters are fixed by the choice of material system, such as InAs and Al.

High magnetic fields decreases the size of the topological gap, but also induce oscillations of the zero energy modes. This is due to the finite-length of the system causing a residual overlap of the Majorana wavefunction, which have a characteristic decay length ξ_M* into the bulk of the Majorana wire. As the magnetic field increases, so does the superconducting coherence length $\xi \propto \frac{1}{\Delta}$, due to the decrease of the induced superconducting gap Δ. This in turn causes an increase in the overlap of the Majorana wavefunction, leading to a stronger hybridization and a larger energy splitting ΔE. This energy splitting can be reduced by increasing the length of the Majorana wire.

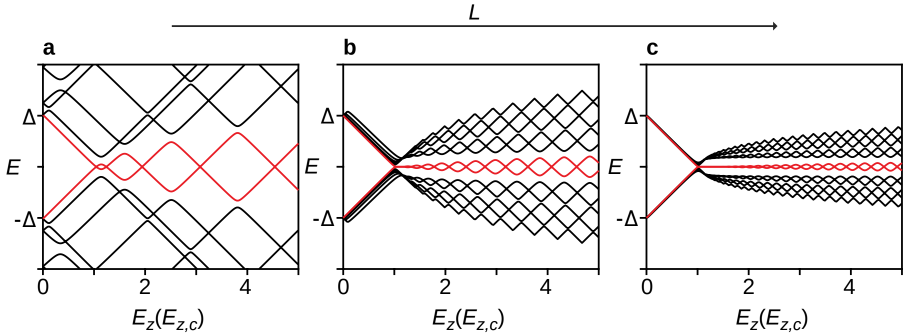

Figure 2.11: **Majorana wire length:** **a-c**, Eigenvalue spectrum as a function of Zeeman energy for increasing nanowire length L leading to a reduced energy splitting of the MZMs. Simulation parameters: $\mu = 0$, $\alpha = 50$, $\Delta = 200$ and number of sites $L = 15$ (**a**), 50 (**b**), 100 (**c**).

Figure 2.11a-c shows the energy spectrum as a function of Zeeman energy for increasing wire length. The most remarkable observation is the decrease in the oscillation amplitude with increasing length. This decrease in oscillation amplitude is directly related to the residual wavefunction overlap of the MZMs. The energy splitting of the zero-energy modes is given by [74, 76],

$$\Delta E = \hbar^2 k_{\mathrm{F,eff}} \frac{\exp(-2L/\xi_{\mathrm{m}})}{m\xi_{\mathrm{m}}} \cos\left(k_{\mathrm{F,eff}} L\right) \quad .$$

where $k_{\mathrm{F,eff}}$ is the effective fermi wave vector associated with the MZM solution. This expression shows that the oscillation amplitude is exponentially suppressed with increasing Majo-

---

*In most cases ξ_M is equal to the superconducting coherence length of the system rana wire length by $\sim e^{-L/\xi_{\mathrm{m}}}$ [74]. The decrease in ΔE with wire length reflects the non-locality of the MZMs, and captures the exponential protection offered by MZMs [76, 77]. For an infinitely long Majorana wire, the MZMs are ideal non-local states with zero wavefunction overlap. It should be noted however, that the topological gap does not increase with L (see 2.11a-c).

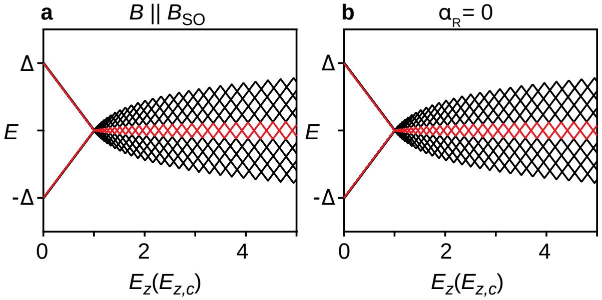

Figure 2.12: **Trivial gap closure:** Eigenvalue spectrum as a function of Zeeman field aligned parallel to the spin-orbit field (**a**), or when there is no Rashba spin-orbit interaction (**b**).

Lastly, Fig. 2.12a addresses the effect of applying a magnetic field not aligned with the Majorana wire axis. Back in chapter 2.2.2 it was observed that a transverse magnetic field that is aligned with the Rashba spin-orbit direction caused a tilting of the energy dispersions without the formation of a Zeeman gap (see Fig. 2.4). When superconductivity is introduced into this scenario, the superconducting gap simply closes with E_Z without reopening to form the topological gap, as shown in Fig. 2.12a. A similar closure of the superconducting gap occurs in the absence of Rashba SOI shown in Fig. 2.12b. This sensitivity to external magnetic field alignment will be used in the following chapters to test the stability of putative zero-energy states [78].

In summary, it was determined that to achieve well-separated MZMs in a one-dimensional nanowire, it is necessary to have strong spin-orbit interaction, a large induced superconducting gap, and a magnetic field aligned parallel to the nanowire axis.

While the model of Eq. 2.13 is idealized, it is instrumental in understanding how this material system can engineer a topological phase of matter. The first experiments providing evidence of MZMs came in the form of zero-bias conductance peaks measured in tunneling spectroscopy at the ends of a Majorana wire [79–82]. These early observations are consistent with the model shown above.

Recently, more realistic models have been considered [74]. For example, if orbital effects are taken into account, the energy splitting ΔE in magnetic field reduces in response to a decrease in wavefunction overlap [83]. Including both orbital contributions and multi subband Majorana wires can lead to a g-factor enhancement [84–86], but also causes a reduction of available parameter space for a topological regime [87]. Moreover, by including disorder induced quantum dots at the ends of a Majorana wire, trivial sub-gap states can mimic the behaviour of the zero-modes discussed above [88]. This motivates experiments that move beyond local tunneling spectroscopy measurements and probe other interesting attributes of MZMs, such as non-locality and Majorana parity.

II

MATERIALS & METHODS

3

HYBRID QUANTUM WELLS

Central to every condensed matter experiment is the material system. The choice of material system constrains the possible experiments, due to factors ranging from material properties, to ease of fabrication. The research of engineered topological phases of matter sets strict requirements on materials (as outlined in chapter 2.4). Furthermore, the envisioned topological qubit device geometries are complex, and therefore, the fabrication must be reliable. This chapter introductions the hybrid semiconductor-superconductor two-dimensional heterostructures used in this thesis. In the following chapter, an overview of the device fabrication on these heterostructures is given.

3.1 INTRODUCTION

One approach for synthesizing topological superconductivity is using s-wave proximitized one-dimensional Rashba nanowire. The first experimental realization of such a system was using vapor-liquid-solid grown free-standing III/V nanowires (InAs / InSb) with diameters $\sim$ 100 nm [79, 89, 90]. Historically, nanowires were proximitized by *ex-situ* evaporation of a superconductor (Al/Nb etc). However, this created poor interface qualities, which reduced the superconducting proximity effect. A material breakthrough was discovered in 2015, whereby Al was grown on the facets of the nanowire before breaking the vacuum of the growth chamber. Material characterization showed a more pristine interface -an epitiaxial match - between the InAs and the Al. Quantum transport characterization showed a hard-induced superconducting gap, indicating a strong hybridization between the semiconductor and superconductor. This material system was instrumental in demonstrating many of the local tunneling spectroscopy signatures of MZMs [80]. However, since nanowires are typically grown individually in a freestanding fashion, more advanced experiments involving multiple nanowires, for fabrication purposes, is challenging.

Two different approaches are actively being pursued to alleviate this fabrication challenge. One is a bottom-up technique similar to nanowire growth, but no catalyst particle is used to nucleate nanowire growth. This technique is called selective-area-growth and involves growing planar nanowires in prefabricated oxide mask[91, 92]. This thesis will not focus on this technique, but instead on a second approach based on two-dimensional heterostructures as will be discussed below.

Motivated by the success of nanowire experiments, the technique of epitaxial Al growth was implemented on two-dimensional quantum wells [17]. This is achieved by first growing a two-dimensional electron gas in close proximity to the surface, that allows for the deposition of a superconductor on top of the 2DEG. This enables the use of conventional top-down lithography techniques, allowing for device geometries to expand into the second dimension. The two-dimensional electron gases studied in this thesis were provided at the courtesy of the Manfra group at Purdue university *. This is a collaboration between QDev and Purdue university focuses on optimizing the material and transport quality of the hybrid quantum wells. This material system continues to have an increase in activity in terms of transport characterization of the material [17, 49, 61, 93–96], superconductor-insulator transitions [97], super-

---

*T. Wang, C. Thomas, S. Gronin, G. Gardner, M. J. Manfra - Department of Physics and Astronomy and Station Q Purdue, Purdue University conducting Coulomb blockade [50], superconducting qubits [98], superconducting quantum interference [99, 100] and transport signatures of MZMs [81, 101, 102].

3.2 WAFER STACK

Two-dimensional electron gases are grown by molecular beam epitaxy (MBE), which grants both a high degree of homogeneity and purity of the growth. Control over the growth temperature and material fluxes allows for layer-by-layer growth, enabling atomically precise monolayers with specific elemental compositions.

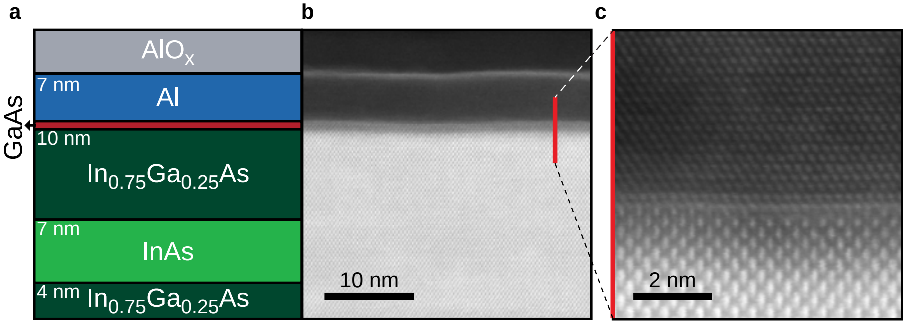

Figure 3.1: **Wafer stack:** **a**, Illustration of the top layers of the wafer stack where the InAs quantum well is confined by two layers of $In_{0.75}Ga_{0.25}As$. **b,c** Cross sectional transmission electron micrograph of the top layers of the InAs-Al heterostructure. The transmission electron micrographs are courtesy of Dr. Rosa Diaz at the Electron Microscopy Facility at the Birck Nanotechnology Center, Purdue University as part of the QDev Purdue collaboration.

The substrates predominately used are semi-insulating Fe-doped InP substrate. InP is chosen because it is moderately compatible with microwave technologies, compatible for generating resonators with reasonably high quality-factors ($Q = 6.4 \times 10^4$) needed for circuit quantum electrodynamics technologies [98]. Similar resonator tests on GaAs or GaSb showed resonators with significantly reduced quality factors. Forgoing quality-factor considerations, GaSb is a promising substrate since the substrate-to-quantum well lattice constant mismatch is reduced in comparison with InP. Generally, this results in a higher quality 2DEG and allows for thicker quantum wells due to reduced strain considerations [103]. An additional benefit of GaSb is that it can be doped to allow for back-gating. However, the GaSb

QWs that were investigated by transport measurements showed numerous problems, ranging from gate voltage hysteresis and issues related to the formation of hole gases when strongly depleting the 2DEG.

The wafer stack starts with an InP substrate and then consists of a 1 µm graded $In_{1-x}Al_xAs$ insulating buffer used to transition from the InP lattice constant (5.87 Å) to the one of InAs (6.06 Å). Following the graded buffer is the InAs quantum well, which is formed by sandwiching 7 nm of InAs between two layers of larger bandgap materials. When a smaller bandgap material is sandwiched between two larger bandgap materials, the chemical potential will align at the interface and form a quantum well (see Fig. 2.2). Usually the bottom barrier comprises of 4 nm $In_{0.75}Ga_{0.25}As$ and a top barrier of either 5 nm $In_{0.9}Al_{0.1}As$ or 10 nm $In_{0.75}Ga_{0.25}As$. The wafer stack is then finished with 2 monolayers of GaAs that are used to protect the 2DEG during wet-etching the Al. The next step is growing a 7 nm film of epitaxial Al. As mentioned, it is critical that this *in-situ* deposition is performed by MBE without breaking the chamber vacuum. This ensures a high transparency between the superconductor and the semiconductor, that is necessary for hybrid devices.

Figure 3.1a,b shows a sketch of the top layers of the wafer stack next a corresponding transmission electron micrograph image showing a high quality quantum well *. The interface between the Al and the quantum well can be seen in Fig. 3.1c, showing an epitaxial match between the two layers.

3.3 WAFER CHARACTERIZATION

To optimize the quality of the 2DEG, a wide variety of different top barrier thicknesses and compositions are grown and characterized by transport measurements. An assortment of characterization devices are fabricated on each growth to examine the material properties of the different wafer stacks. Details of the device fabrication approaches are given in chapter 4.1.

The standard characterization devices can be seen in Fig. 3.2. Primarily, the peak mobility and the induced superconductivity are measured to track the quality of the 2DEGs. Standard Hall bar techniques (Fig. 3.2a) are used to measure the density and mobility and a S-QPC-N geometry is used to measure the induced gap by tunneling spectroscopy (Fig. 3.2c). Supercurrent properties are screened in a superconductor-normal-superconductor Josephson

---

*Micrographs are courtesy of Dr. Rosa Diaz at the Electron Microscopy Facility at the Birck Nanotechnology Center, Purdue University.

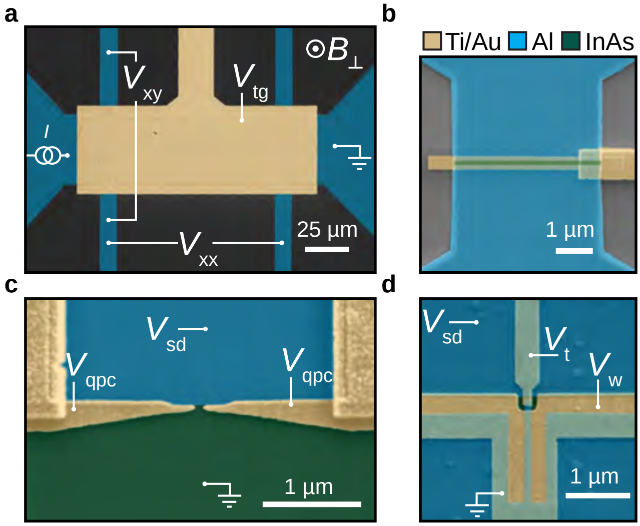

Figure 3.2: **Wafer characterization devices:** **a**, Conventional Hall bar with superconducting leads. **b**, Supercurrent properties are measured in a superconductor-normal-superconductor (S-N-S) Josephson junction with a top-gate. **c**, Tunneling spectroscopy of the proximitized quantum well is performed in a superconductor-quantum point contact-normal geometry (S-QPC-N) where the the QPC is used to create a tunneling barrier at the N-S interface. **d**, One-dimensional nanowire created by electrostatic confinement with a gate voltage V_{w} with a tunnel probe at one end controlled by gate voltage V_{t}.

junction (Fig. 3.2b) that also allows for an indirect determination of the superconducting gap [94]. However, this method of superconducting gap extraction is only resorted to if the S-QPC-N devices are faulty. Andreev bound states and Majorana zero modes are investigated in one-dimensional wire geometries (Fig. 3.2d).

3.3.1 Density and mobility

Density and mobility was measured in a Hallbar as shown in 3.2a where a current bias of $I = 10 - 20$ nA is passed through the device and the longitudinal (V_{xx}) and transverse (V_{xy}) voltages were recorded as a function of top-gate voltage V_{tg} and perpendicular magnetic field, $B_\perp$. To remove any sample specific geometry effects the per-square longitudinal and transverse resistivity are calculated for a Hall bar of length L and width W by [42],

$$\rho_{xx} = \frac{V_{xx}}{I}\frac{W}{L}, \quad \rho_{xy} = \frac{V_{xy}}{I} \quad .$$

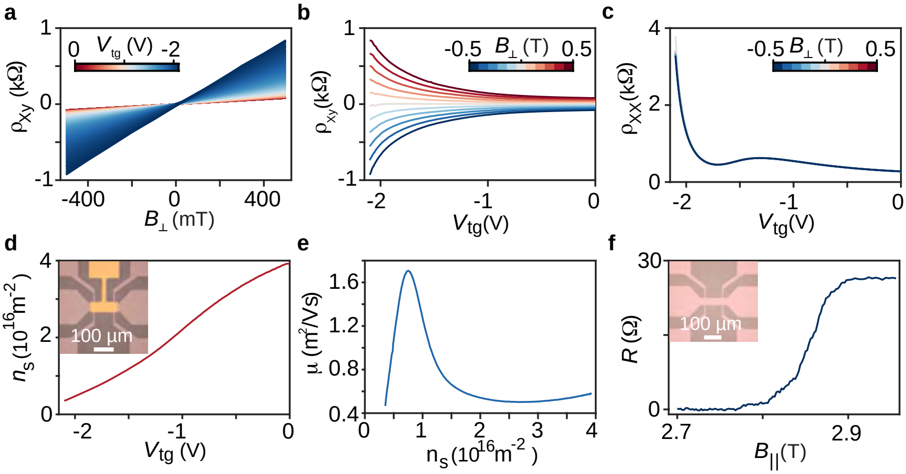

Figure 3.3: **Hall bar:** **a,b**, Hall resistivity ρ_{xy} as a function of top gate voltage V_{tg} and perpendicular field $B_\perp$. **c**, Longitudinal resistivity ρ_{xx} as a function of V_{tg} and $B_\perp$. **d**, V_{tg} dependence on carrier density n_s. **e**, Carrier mobility μ as a function of n_s. **f**, Critical in-plane magnetic field measured in an Al hall bar.

In Fig. 3.3a,b the transverse resistivity is shown as a function of $B_\perp$ and V_{tg}, which is used to calculate the electron density,

$$n_s = \frac{1}{e(d\rho_{xy}/dB)}$$

where n_s, and e are the electron density and charge, respectively. Figure 3.3d shows the calculated density as a function of V_{tg}, whereby applying a negative top-gate voltage, the carrier density in the 2DEG is controlled. From the longitudinal resistivity (Fig. 3.3c) the mobility μ at a specific V_{tg} is calculated from,

$$\mu = \frac{1}{en_s\rho_{xx}}$$

The mobility as a function of V_{tg} is shown in Fig. 3.3e, where a maximum of 1.8 m^2/Vs is obtained at $n_{\mathrm{s}} = 0.9 \times 10^{16}\ \mathrm{m}^{-2}$. The peak mobility at lower density may reflect the fact that the surface is a dominant source of scatter, and that two sub-bands are occupied at low voltages [104]. Usually our devices are operated at negative gate voltages that takes advantage of this enhancement.

3.3.2 AL FILM

A large Zeeman energy is required for hybrid InAs-Al heterostructures to undergo a topological phase transition. Therefore, the epitaxial Al needs to be able to withstand large in-plane magnetic fields. The critical magnetic field of the epitaxial Al film is determined by measuring a 4-terminal Hall bar geometry in a device where the epitaxial Al has not been etched away (see inset of Fig. 3.3f). Figure 3.3f shows the resistance of the Al Hallbar as a function of in-plane magnetic field $B_{||}$, displaying an increase in resistance at $B_{||} = 2.9$ T, marking critical magnetic field B_{c}. It is important to correct any misalignment of $B_{||}$ to achieve the highest B_{c}. The high B_{c} is caused by having the thin Al film. The Al superconducting gap Δ increases with decreasing Al thickness [105]. Additionally, this value is higher than those typically reported for nanowires, which may be related to the planar morphology and low surface roughness heterostructures. Using the Clogston-Chandrasekhar limit [52] $B_{\mathrm{c}} = \frac{\Delta}{\sqrt{2}\mu_{\mathrm{B}}}$ allows for $\Delta_{\mathrm{Al}} = 240\ \mu\mathrm{eV}$ to be extracted.

3.3.3 INDUCED SUPERCONDUCTIVITY

The quality of the induced superconducting gap is measured in a S-QPC-N device geometry to allow for a tunnel barrier to be formed at the interface between the semiconductor and Al (see Fig. 3.2c). A tunnel barrier is formed by depleting the 2DEG in the vicinity of the QPC with a gate voltage V_{qpc}. In Fig. 3.4c the differential conductance G is measured as a function of the gate voltage V_{qpc}, where a plateau at $4e^2/h$ is observed at $V_{\mathrm{qpc}} = -6.25$ V. For a ballistic QPC in the normal state, conductance quantization causes plateaus at integer steps of $2e^2/h$ [39]. For a high transparency N-S interface, Andreev reflection causes an additional charge transfer of $2e$. This is reflected in quantization of conductance steps $4e^2/h$ [61]. However, any remnant scattering will reduce the step towards $2e^2/h$. This shows that even a simple depletion curve can be used to test the quality of the material. Additionally, applying a large perpendicular magnetic field $B_{\perp} = 1$ T in Fig 3.4c shows a slight plateau at $2e^2/h$, reflecting the normal state of the Al.

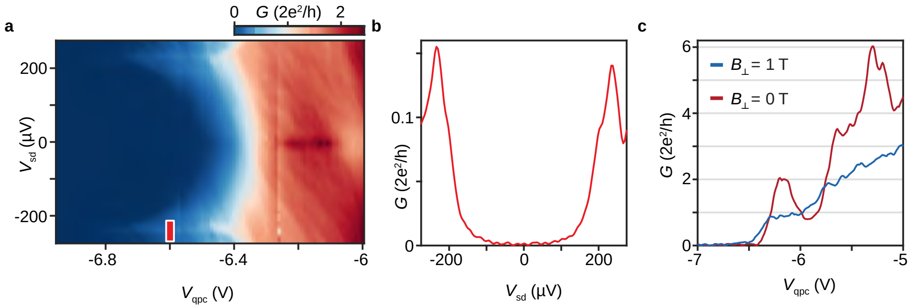

Figure 3.4: **Induced superconductivity:** **a**, Differential conductance G as a function of quantum point contact gate voltage V_{QPC} and bias voltage V_{sd}. **b**, G as a function of V_{sd} for $V_{\mathrm{QPC}} = -6.6$ V. **c** Zero-bias G as a function of V_{QPC} for a perpendicular magnetic field $B_{\perp} = 0$ and 1 T.

A tunnel barrier is formed by setting V_{qpc} below the last plateau (<-6.4 V). Measuring G as a function of bias voltage V_{sd} and V_{qpc} reveals a hard superconducting gap of $\Delta^* = 230\ \mu$eV (see Fig. 3.4a,c). This indicates a clean interface between the Al and the QW and a high quality proximity effect. This was not the case for all wafer stacks that were investigated. Wafers stacks containing top-barriers that are either thicker or have a higher potential would typically reduce the proximity effect (not shown here).

To determine the superconducting coherence length ξ_0 in the proximitized semiconductor the density at peak mobility is used. The length scale ξ_0 describes the distance between electrons pairs in the superconductor and is determined in the clean limit as,

$$\xi_0^{\mathrm{clean}} = \frac{\hbar v_{\mathrm{F}}}{\pi \Delta} \sim 1\ \mu\mathrm{m} \quad .$$

However, in this case the mean free path is $l_e \ll \xi_0^{\mathrm{clean}}$ and coherence length is described in the dirty limit as,

$$\xi_0^{\mathrm{dirty}} = \sqrt{\xi_0^{\mathrm{clean}} l_e} \sim 0.5\ \mu\mathrm{m}$$

where l_e is the electron mean free path in the semiconductor.

3.3.4 SUB-GAP STATES IN ONE-DIMENSIONAL NANOWIRES

Tunneling spectroscopy of one-dimensional nanowires is achieved by selectively etched the Al film into an elongated Al strip with a width of 0.1 μm and length of 1.5 μm) (see Fig.3.2d). Then using top-gate voltage V_w, the 2DEG surrounding the Al stripe is depleted, while the Al stripe screens the electric field from the V_w (see Refs [101, 106] for details). This forms a proximitized one-dimensional nanowire below the stripe. Tunneling spectroscopy is performed at the end of the one-dimensional stripe by forming a tunnel barrier with a gate voltage V_t.

In Fig. 3.5a, tunneling spectroscopy reveals a 4Δ superconducting gap due to S-I-S transport, which transitions to N-I-S spectroscopy at $B_{||} = 0.2$ T as a consequence of a softening of the superconducting gap under the large Al lead [101]. Increasing $B_{||} > 3$ T causes the induced superconducting gap Δ^* to collapse. A keen eye may observe that Δ^* persists higher than 2.9 T observed for the Al Hall bar in Fig. 3.3f. Typically a higher critical field was measured for elongated narrow nanowires compared to large planes of Al by several hundreds of mT in both $B_{||}$ and $B_{\perp}$. This discrepancy is potentially the result of confinement.

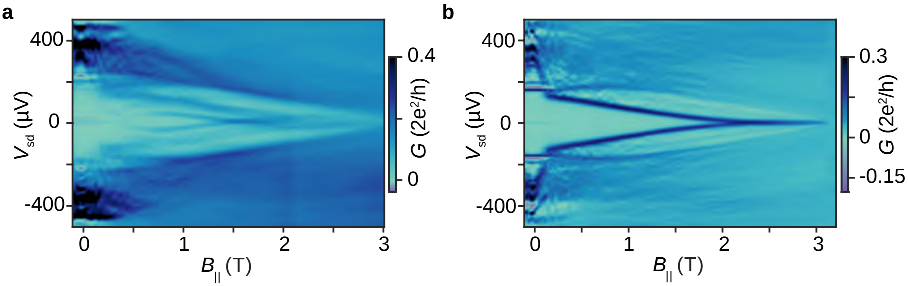

Figure 3.5: Sub-gap states in a one-dimensional nanowire: **a**, Differential conductance G as a function of parallel magnetic field $B_{||}$ and bias voltage V_sd in the tunneling regime (high density). **b**, G as a function of $B_{||}$ and V_sd (low density).

We next focus on the magnetic field dependence of the sub-gap features. Figure 3.5a shows the appearance of a few sub-gap resonances, which are interpreted to be Andreev bound states (ABS) of the proximitized one-dimensional wire. As seen in Fig. 3.5 these states cross zero-bias at $B_{||} = 1.5$ T and continue to finite-bias. Thsee Andreev bound states are expected precursors of Majorana zero modes (MZM), which could undergo a topological transition if the system parameters are correct. However, since these ABS do not remain at zero-bias as anticipated for MZMs (see Chapter 2.4), a trivial origin of these Andreev bound states is suspected.

In certain gate-voltage configurations, the ABS merge and stick to zero-energy as the magnetic field increases as shown in Fig. 3.5b. Such observations are consistent with a MZM picture, however, more evidence is needed to draw conclusions. Nevertheless this is valuable information when determining if the wafer is promising for pursuing more complicated device geometries for investigating topological superconductivity.

Comparing the two cases, I note a large discrepancy between the g-factors is noticed (see Fig. 3.5a and b). In higher density regimes as in Fig. 3.5a, a larger g-factor is frequently observed. In nanowire experiments, higher density regimes resulted in a g-factor enhancement and depleting the nanowire lead to a reduced g-factor. This is attributed to orbital effects [84, 85]. I believe that the relevant g-factor in the one-dimensional nanowires is given by sub-gap states that merge and form a robust zero-bias conductance peak, for which a g-factor of 4 is typically obtained.

3.3.5 Phase coherence

The phase coherence length of the InAs 2DEG was measured by fabricating an Aharonov-Bohm (AB) interferometer by wet etching a hole in the 2DEG and then defining a loop with gates as show in Fig. 3.6a. A negative gate voltage applied to the gate electrodes confines the 2DEG into a loop. Figure 3.6b shows the differential conductance G as a function of perpendicular magnetic field $B_\perp$ revealing periodic conductance oscillations with a flux periodicity of h/e. This indicates coherent single electron transport through the Aharonov-Bohm interferometer.

To extract the phase coherence length the semiconductor, the temperature dependence of the AB oscillations in a normal conducting 2DEG is measured. In Fig 3.6a the conductance ΔG (slowly varying background subtracted) is shown as a function of $B_\perp$ which controls the flux through the interferometer. The conductance oscillations in $B_\perp$ with a periodicity of h/e indicating phase coherent transport through the interferometer. Studying the amplitude of these oscillations as a function of temperature allows for the phase coherence length to be extracted. Figure 3.6c shows the temperature dependence of the AB oscillations amplitude A which is extracted by calculating the power spectrum of the oscillating curves in Fig. 3.6b. To extract the phase coherence length a diffusive interferometer is assumed, for which the amplitude decays exponentially with temperature as $A = A_0 \exp(-L/l_\varphi(T))$, where $l_\varphi(T) \propto T^{-1/2}$ is the phase coherence length and $L = 4.5\ \mu\text{m}$ is the circumference of the interferometer [107]. The exponential fit $A = A_0 \exp(-aT^{1/2})$ gives a base temperature coherence length of $l_\varphi(20\ \mathrm{mK}) = 4\ \mu\mathrm{m} \pm 1\ \mu\mathrm{m}$. Error bars show the standard deviation between 4 data sets at each temperature.

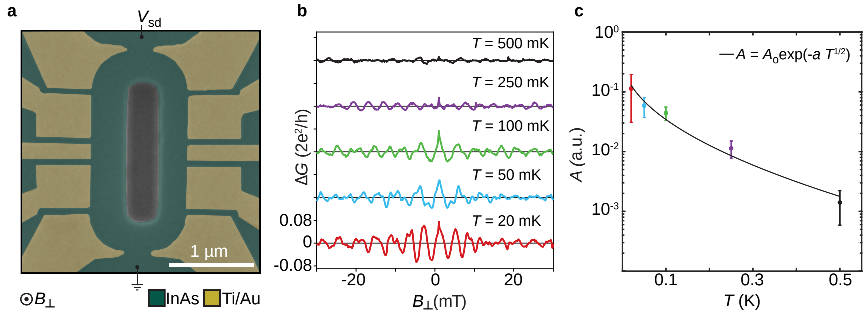

Figure 3.6: Phase coherence: **a**, False colored electron micrograph of a InAs Aharonov-Bohm interferometer. **b**, Differential conductance ΔG as a function of perpendicular magnetic field $B_\perp$ at increasing temperatures. **c**, Temperature dependence of the AB oscillation amplitude

4

METHODS

This chapter reviews the fabrication procedure used for creating quantum devices on the hybrid quantum wells (introduced in the previous chapter). A general overview of conventional lock-in techniques to used to measure the differential conductance and resistance and unconventional third harmonic lock-in techniques used to measure the zero-bias curvature are discussed. Lastly, details on the development of a normal lead for tunneling spectroscopy are given.

4.1 DEVICE FABRICATION

The design and fabrication of quantum devices on InAs-Al heterostructures is particularly flexible because it relies on a top-down fabrication approach. This allows for a complete devices to be drawn in a computer-aided design software, and the resulting device is almost an exact replica. With the current standard recipe, Al etch resolutions of $\sim$ 20 nm and gate resolutions of $\sim$ 30 nm are achieved with standard 100 keV e-beam lithography techniques and PMMA resists. Another usually overlooked advantage of the InAs-Al heterostructures is that ohmic contact is made by bonding directly on the epitaxial Al. This mitigates the need for harmful oxide milling procedures, which are necessary for fabrication based on vapour-liquid-solid or selective-area grown nanowires. This milling is usually quite close to nanowire tunnel junctions and has adverse effects. For the devices discussed in this thesis, Ohmic contacts were formed by wire bonding directly onto the epitaxial Al, creating a superconducting lead that terminates only a few microns away from the device.

In the following section, a brief overview of a standard device fabrications flow is outlined. A fantastic detailed description on fabrication was written by a previous PhD student, Morten Kjaergaard, that should be read before starting fabrication on this material system [108]. In appendix A the standard fabrication recipe used for devices in this thesis is given.

With a freshly cleaved sample, the first fabrication step was the mesa etch to define the template for the devices (bonding pads, ohmic contacts, etc.) and alignment marks. Figure 4.1 shows the standard e-beam lithography flow starting with spinning resist (PMMA A4). The next step was to expose the resist with a 100 keV Elionix e-beam system and develop in MIBK:IPA 1:3. It was critical that resist was developed for 45 s and a short 5s rinse in IPA to minimize resist swelling. With the PMMA etch mask completed the next step was to etch the mesa, starting with a 6s Al etch (50 °C Transene Type D), followed by a $\sim$300 nm III-V chemical etch
$H_2O : C_6H_8O_7 : H_3PO_4 : H_2O_2$ (220:55:3:3) (usually 9 minutes at room temperature). This ensured that the device was electrically isolated from other devices and the bonding pads for the gates. The resist was then stripped before continuing with the next step.

Following the same e-beam procedure the fine Al features were patterned with a 5s Al etch* and then the chip was directly transferred to the atomic layer deposition system to minimized Al oxidation. Around 15 to 30 nm of HfO_2 was grown over the entire sample to isolate

---

*this is by far the most delicate fabrication step.

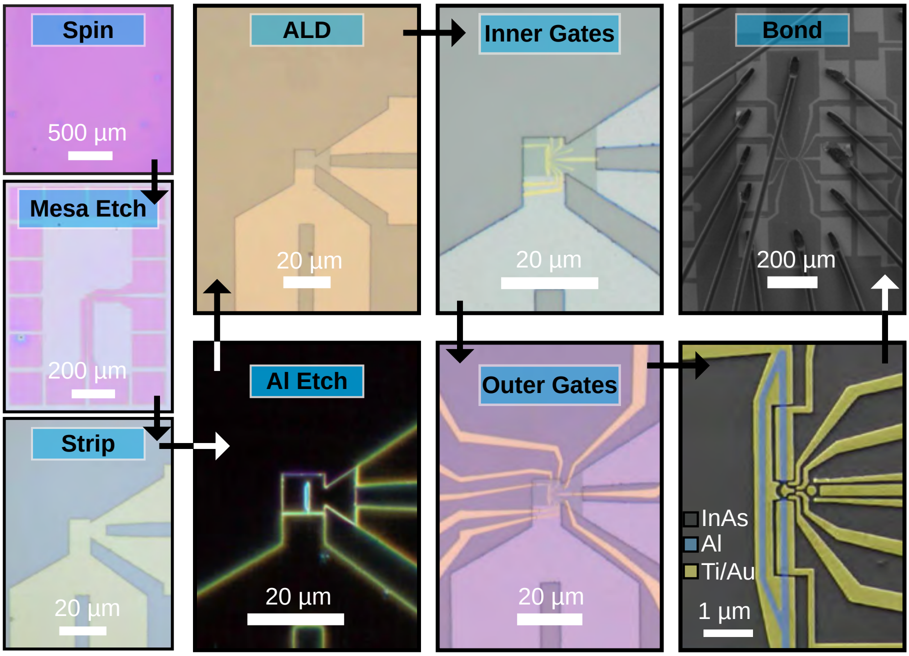

Figure 4.1: **Fabrication:** Device fabrication flow diagram shown by optical and scanning electron micrographs. Left panels show the standard e-beam lithography procedure of spinning, exposing, developing, and stripping the resist. The rest of the panels use the same procedure, with the images taken after stripping the resist. The Al Etch image is an exception, where the image is taken directly after etching in an optical dark-field microscope, where the outline of the Al etch mask can still be seen. This is a good sign that the etch went well.

the following gate stack from the 2DEG. The fine inner top gates were then deposited with a e-beam evaporator with Ti/Au (5/25 nm) and then electrically connected to the bonding pads with meanders of Ti/Au (5/300 nm) while tilting and rotating to ensure the leads crawl up the mesa side walls.

After finishing fabrication, the sample was investigated by either SEM or AFM to check alignment and etch run. The devices were then glued to a chip-carrier with PMMA, making sure chip is well aligned to the chip-carrier to have a well aligned magnetic field. Devices were contacted by bonding through the HfO_2 with a wedge bonder. The devices were then ready to be measured in a dilution refrigerator.

4.2 Measurement techniques

4.2.1 Differential conductance

The devices typically used a four Ohmic contact setup to allow for four-terminal differential conductance measurements. We used standard lock-in techniques (Stanford Research Systems SR-830) at frequencies between 30 - 180 Hz by applying the sum of a variable dc bias voltage V_{sd} and an AC excitation voltage of 3 to 10 μV to one of the ohmic contacts. The resulting differential current dI was measured by another ohmic that was grounded via a low-impedance low-noise current-to-voltage converter (Physics Basel SP-983). The four-terminal voltage $dV_{4\mathrm{T}}$ across the device was measured by an differential voltage amplifier with an input impedance of 500 MΩ. The differential conductance G $=dI/dV_{4\mathrm{T}}$ was then calculated.

4.2.2 Differential resistance

To measure the critical current of a SNS junction the setup was slightly modified. The differential resistance $R = dV_{4\mathrm{T}}/dI_{\mathrm{ac}}$ was obtained by applying an AC current bias $I_{\mathrm{ac}} < 5$ nA (using a 5 V AC excitations through a 1 GΩ resistor), superimposed on a variable DC current bias I_{dc}. The four terminal voltage was measured allowing for the differential resistance to be calculated.

4.2.3 Third harmonic technique

Majorana zero modes are zero-bias excitations inside of a topological gap as shown in Chapter 2.4. A transport signature of a MZM is a zero-bias conductance peak in tunneling spectroscopy at the ends of a Majorana wire. Conventional first harmonic lock-in techniques used to measure the differential conductance G at zero-bias cannot distinguish if the zero-bias feature is a peak or a dip in source-drain bias V_{sd}. However, by recording the third harmonic of the differential current it is possible to efficiently determine if the zero-bias feature is indeed a zero-bias peak or a zero-bias dip.

The third harmonic technique was used in wide variety of experiments to efficiently sweep large multi-dimensional parameter-spaces to identify regions where zero-bias conductance peaks occur. This technique allows for the curvature of the zero-bias conductance to be measured, and discern if the feature is a peak or a dip without varying the bias voltage V_{sd}.

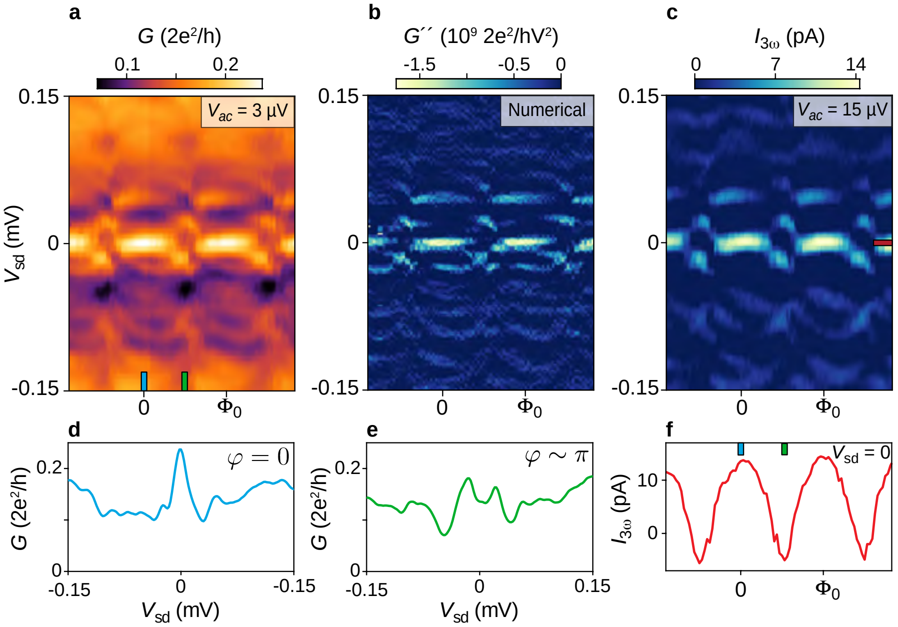

Figure 4.2: Measurement of the third harmonic of the current: a, Differential conductance G as a function of source-drain bias V_{sd} and magnetic flux Φ. **b**, Numerical second derivative of the conductance $G''(V_{\mathrm{sd}}) = (\partial^2 G/\partial V_{\mathrm{sd}}^2)|_{V_{\mathrm{sd}}}$ as a function of V_{sd} and Φ calculated from the data shown in **a**. **c**, Third harmonic of the current $I_{3\omega}$ versus V_{sd} and Φ measured by the lock-in amplifier using an excitation $V_{\mathrm{ac}} = 15$ µV. Most of the features present in panel **b** are reproduced in panel **c**. **d, e**, Line cuts of G as a function of V_{sd} taken at $\phi = 0$, π as indicated by the ticks in panel **a**. **f**, $I_{3\omega}(V_{\mathrm{sd}} = 0)$ as a function of Φ: a positive value of $I_{3\omega}(V_{\mathrm{sd}} = 0)$ indicates a ZBP in G.

To obtain information about the curvature at zero-bias a lock-in amplifier (model SR830) is used to measure the current at the third harmonic of the reference frequency ω. Typically a low $\omega < 50$Hz was used to avoid filtering of the third harmonic signal at 3ω. A sinusoidal time-dependent excitation $V(t) = V_{\mathrm{sd}} + V_{\mathrm{ac}}\sin(\omega t)$ was applied to the device, and the measured output current can be expanded in Taylor's series as:

$$I(t) \simeq I(V_{\mathrm{sd}}) + \left.\frac{\partial I}{\partial V}\right|_{V_{\mathrm{sd}}} V_{\mathrm{ac}} \sin(\omega t) + \frac{1}{2}\left.\frac{\partial^2 I}{\partial V^2}\right|_{V_{\mathrm{sd}}} [V_{\mathrm{ac}} \sin(\omega t)]^2 + \frac{1}{6}\left.\frac{\partial^3 I}{\partial V^3}\right|_{V_{\mathrm{sd}}} [V_{\mathrm{ac}} \sin(\omega t)]^3.$$

the measured third harmonic current is then*,

$$I_{3\omega}(V_{\mathrm{sd}}) = -\frac{1}{24}\left.\frac{\partial^3 I}{\partial V^3}\right|_{V_{\mathrm{sd}}} V_{\mathrm{ac}}^3 \propto -\left.\frac{\partial^2 G}{\partial V^2}\right|_{V_{\mathrm{sd}}}.$$

In order to increase the signal-to-noise ratio, the measurement of $I_{3\omega}(V_{\mathrm{sd}})$ was performed with an amplitude V_{ac} of the excitation greater than the temperature-limited full width at half maximum of a Lorentzian feature, i.e., $V_{\mathrm{ac}} \gtrsim 3.5\, k_{\mathrm{B}} T$, where k_{B} is the Boltzmann constant and $T \sim 40$ mK is the electron temperature estimated by the temperature dependence saturation of zero-bias peak conductance [81].

Figure 4.2 shows a comparison between the numerically calculated $G''(V_{\mathrm{sd}})$ and the measured $I_{3\omega}(V_{\mathrm{sd}})$. Fig. 4.2a shows tunneling spectroscopy of a S-N-S junction as a function of magnetic flux Φ threading a SQUID loop (see the next section or chapter 10 for device and measurement details). At $\Phi = 0$ the conductance is peaked at zero bias (see Fig. 4.2d), while at $\Phi = \Phi_0$ there is a zero-bias dip. Numerically calculating the second derivative of the conductance $G''(V_{\mathrm{sd}})$ gives information about the curvature, where a negative second derivative indicates a peak. Instead, if $I_{3\omega}$ is measured using the third harmonic, a similar plot is obtained (see Fig. 4.2c). This shows that not only are the zero-bias peaks correctly identified, but also the finite-bias features. This allows for $V_{\mathrm{sd}} = 0$ to be fixed and determine if the zero-bias feature is peaked in V_{sd} by obtaining a positive value of $I_{3\omega}$, as shown in Fig. 4.2f.

4.3 NORMAL LEAD SPECTROSCOPY

The initial tunneling spectroscopy experiments of one-dimensional nanowires in 2DEGs relied on a large Al lead to achieve well resolved tunneling spectroscopy [81, 101]. It is believed that the screening offered by the Al lead allows for sharp tunnel barriers to be achieved. On the other hand, S-I-S spectroscopy adds unwanted complexity to tunneling spectroscopy.

This issue was combatted with the observation that applying a small magnetic field causes the large Al lead to be populated with sub-gap conductance (due to sub-gap states) and to

---

*Using $(\sin(\omega t))^3 = 1/4\,(-\sin(3\omega t) + 3\sin(\omega t))$

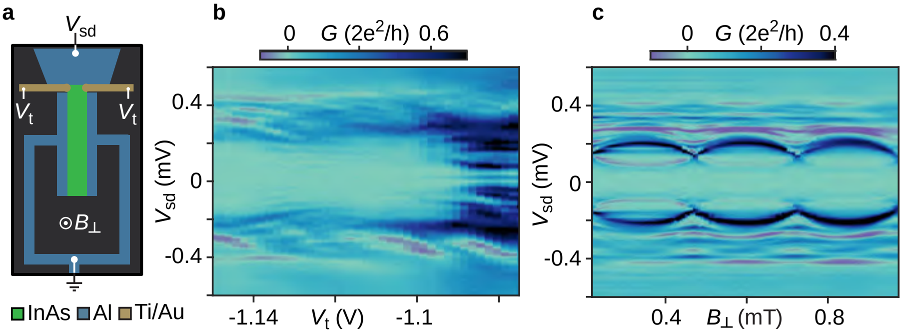

Figure 4.3: **Al lead spectroscopy:** **a**, Sketch of a S-N-S Josephson junction with an additional Al lead at the top for S-I-S tunneling spectroscopy. **b**, Differential conductance G measured as a function of bias voltage V_{sd} and tunnel barrier gate voltage V_t. An induced superconducting gap is observed. **c**, G measured as a function of a perpendicular magnetic field $B_\perp$ and V_{sd}.

effectively render it a normal lead, while the hard superconducting gap is preserved in the Al stripe due to electrostatic confinement. This allowed for N-I-S tunneling spectroscopy of nanowires in a finite magnetic field (see for example Fig. 3.5). The transition from S-I-S to N-I-S spectroscopy was detailed in Ref [101]. This transition typically occurred at a in-plane field of $B_{||} \sim 0.2$ T, while the zero-bias peak signatures of interested appeared at $B_{||} > 2$ T in nanowire geometries.

One of the prominent predictions of a topological planar Josephson junction is that a topological phase transition should occur at lower magnetic fields [35, 36]. The Al lead spectroscopy was therefore ill-suited for the devices investigated in chapter 10. This warranted a normal lead to be developed for the devices. In the following discussion, measurements with the Al plane spectroscopy technique will be shown first and then used to compare with device used to develop normal lead spectroscopy.

Figure. 4.3a shows a schematic of a RF-SQUID where two Al leads (S) confine a semiconducting region (N) to form a SNS Josephson junction. At the top-end of the junction is an additional Al lead used for spectroscopy together with a quantum point contacts (QPC) used to form a tunnel barrier with a voltage V_t (see chapter 3.3.3). The differential conductance G was measured through the QPC as a function of bias voltage V_{sd} and gate voltage V_t, where a superconducting gap is observed (see Fig. 4.3b). Applying a perpendicular magnetic field $B_\perp$ threads fluxes in the superconducting loop and modulates the superconducting gap (see Fig. 4.3b).

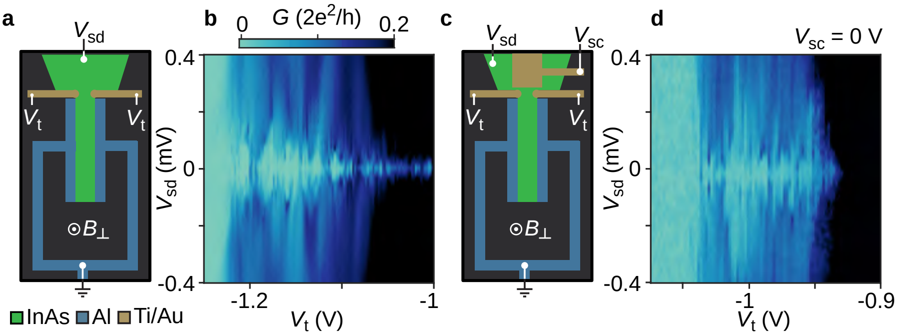

Figure 4.4: **Normal lead spectroscopy without a protrusion:** **a**, Sketch of a device with a quantum point contact tunnel probe. **b**, Differential conductance G as a function of bias voltage V_{sd} and tunnel barrier gate voltage V_t reveals disordered spectroscopy. **c**, Sketch of a device with a screening electrode operated at $V_{sc} = 0$ V and a point contact tunnel probe. **d**, Differential conductance G as a function of bias voltage V_{sd} and tunnel barrier gate voltage V_t reveals disordered spectroscopy.

In an attempt to move away from the complicated Al lead, a standard point contact geometry was invesigated(see Fig. 4.4). However, as observed in Fig. 4.4b, the tunneling spectroscopy is disordered and no superconducting features are recovered. An alternative approach is to use a gate electrode to mimic the Al screening effects as schematically drawn in Fig. 4.4c. The principle of this gate is to screen the electric fields originating from the quantum point contacts from depleting the 2DEG below the screening gate electrode (SC), allowing for a sharp tunnel barrier to be defined lithographically. However, operating this screening gate at $V_{sc} = 0$ V did not improve the tunneling spectroscopy (see Fig. 4.4d).

If instead, a small protrusion was added to the end of the screening electrode, which extends between the two point contact electrodes, a well resolved induced superconducting gap was observed (see Fig. 4.5a,e). The role of the protrusion is investigated by measuring G as a function of V_{sc} and V_t in Fig 4.5b. At $V_{sc} = 0$ V, a large $V_t = -2.5$ V is needed to close the conductance. Decreasing V_{sc} leads to a tail of conductance until $V_{sc} \sim -0.4$ V where a rectangular dependence of V_{sc} and V_t is observed. Comparing these results with a similar measurement for a screening gate without a protrusion (Fig. 4.5c, d) this tail feature is not observed and only a rectangular dependence of V_{sc} and V_t is found, with a $V_t \sim -1.1$ V

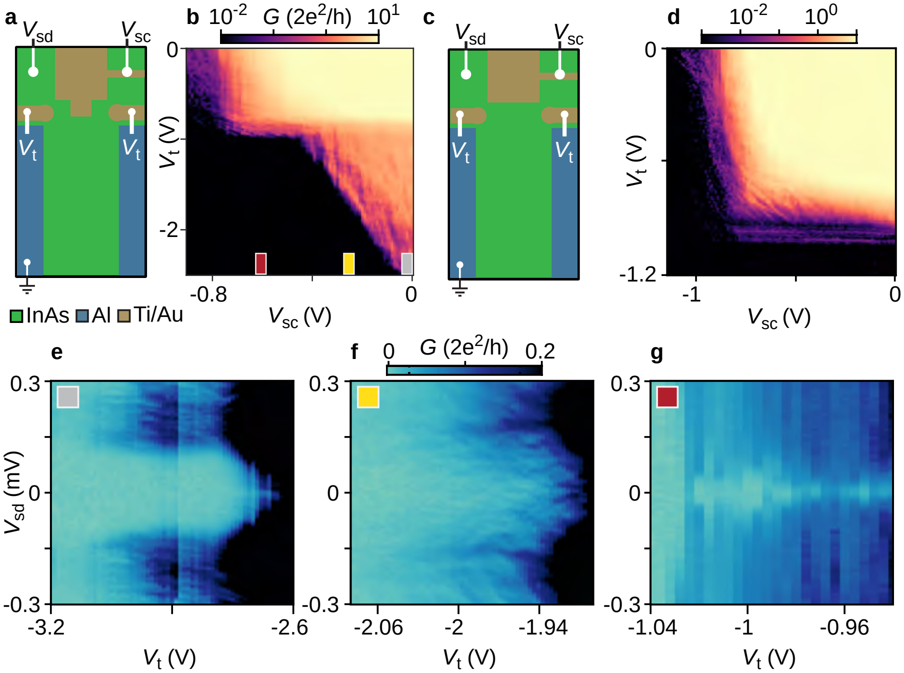

Figure 4.5: **Normal lead spectroscopy with a protrusion:** **a**, Sketch of a device with a screening electrode with a small protrusion and a point contact tunnel probe. **b**, Differential conductance G as a function of tunnel barrier gate voltage V_t and screening gate voltage $V_{sc} = 0$ for $V_{sd} = 0$ **c**, Sketch of the same device as **a** but without the protrusion. **d**, Differential conductance G as a function of tunnel barrier gate voltage V_t and screening gate voltage $V_{sc} = 0$ for $V_{sd} = 0$. **e-g**, Differential conductance G measured as a function of V_{sd} and V_t for different values of V_{sc} for the device in **a**.

pinching off (earlier than with the protrusion).

In Fig. 4.5e-g we measure G as a function of V_t and V_{sd} for different values of V_{sc}. For values of V_{sc} within the tail (Fig. 4.5f) a superconducting gap is resolved. However, for more negative values of V_{sc} outside of the tail, no induced gap is observed (Fig. 4.5e,g). Based on these results, it is believed that the protrusion is responsible for creating a narrow well-defined tunnel barrier at the top the the Josephson junction.

III

MAJORANA ISLANDS

5

SPECTROSCOPY OF SUB-GAP STATES IN MAJORANA ISLANDS

This chapter introduces the theoretical background of Majorana islands and the expected signatures of MZMs in these islands. It is shown that the superconducting Coulomb blockade peak spacing analysis allows for the energy of the lowest sub-gap state to be measured. Lastly, the Majorana island device geometry is introduced and transport characterization of the islands is shown.

5.1 PEAK SPACING ANALYSIS

Several recently proposed topological qubit architectures involve Majorana islands (floating one-dimensional topological superconductors) that have a finite charging energy, which protects the island from external quasiparticles that poison the parity of the MZMs [31–33]. The first experimental signatures of MZMs in a N-I-S-I-N geometry (Majorana island) were reported in 2016, showing signatures of the exponential protection expected for MZMs [77]. Below we will introduce the basic concepts of Majorana islands, and how to tune the device into promising regimes with zero-bias states.

At low temperatures the ground state energy of a Majorana island is $E(N)$ is minimized [109],

$$E(N) = E_c(N - N_g)^2 + \begin{cases} E_0, & \text{if N is odd} \\ 0, & \text{is N is even} \end{cases} \tag{5.1}$$

where $N_g = CV_g/e$ is the dimensionless gate voltage, where E_0 is the energy of the lowest sub-gap state. A parallel magnetic field, $B_{||}$, lowers the energy of E_0 due to the Zeeman effect. In Fig. 5.1 we show the charge parabolas for different values of E_0. At low fields where $E_0 > E_c$, charge degeneracies occur when $E(N) = E(N+2)$ for odd integers of N_g causing Coulomb peaks to be 2e periodic. This is due to charge transfer of electron pairs mediated by Andreev reflection on either end of the Majorana island [110].

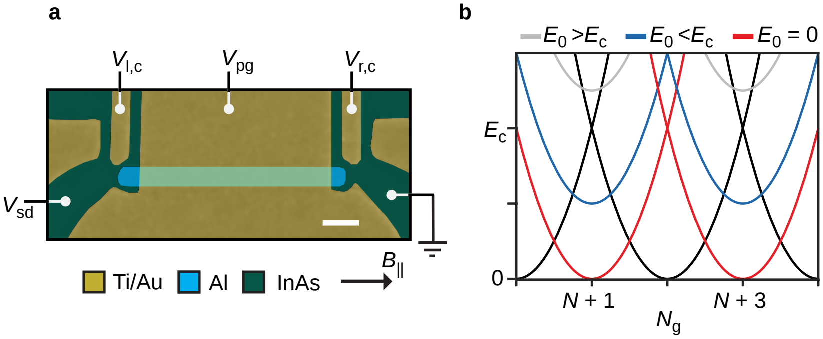

Figure 5.1: Coulomb blockade of a Majorana island: **a**, False colored electron micrograph of a Majorana island. **b**, Energy spectrum of a Majorana island displaying the characteristic charge parabolas different E_0 energies (see Eq. 5.1).

Increasing the magnetic field lowers $E_\mathrm{o} < E_\mathrm{c}$, allowing for single electrons to occupy the island at an energy cost that leads to an even-odd (e-o) peak spacing. In this regime, two charge degeneracies occur within the $2e$ window - one at $E(N) = E(N+1)$ and another at $E(N+1) = E(N+2)$. This causes Coulomb peaks to occur at [77, 109, 111],

$$N_\mathrm{g}^\mathrm{e}(N) = N + \frac{1}{2} + \frac{E_\mathrm{o}}{2E_\mathrm{c}} \quad E_\mathrm{N} = E_\mathrm{N+1} \quad ,$$

$$N_\mathrm{g}^\mathrm{o}(N) = N + \frac{3}{2} - \frac{E_\mathrm{o}}{2E_\mathrm{c}} \quad E_\mathrm{N+1} = E_\mathrm{N+2} \quad .$$

With this the distance between Coulomb peaks can be calculated. The spacing of the odd valley $\Delta N_\mathrm{g}^\mathrm{o}$ is between $E_\mathrm{N+2} = E_\mathrm{N+1}$ and $E_\mathrm{N+1} = E_\mathrm{N}$ and is therefore,

$$\Delta N_\mathrm{g}^\mathrm{o} = N_\mathrm{g}^\mathrm{o}(N) - N_\mathrm{g}^\mathrm{e}(N) = 1 - \frac{E_\mathrm{o}}{E_\mathrm{c}} \quad .$$

Similarly, the spacing of the even valley $\Delta N_\mathrm{g}^\mathrm{e}$ is found, which occurs between $E_\mathrm{N+3} = E_\mathrm{N+2}$ and $E_\mathrm{N+2} = E_\mathrm{N+1}$ giving,

$$\Delta N_\mathrm{g}^\mathrm{e} = N_\mathrm{g}^\mathrm{e}(N+2) - N_\mathrm{g}^\mathrm{o}(N) = 1 + \frac{E_\mathrm{o}}{E_\mathrm{c}} \quad .$$

Using a lever arm η, the peak spacing $\Delta N_\mathrm{g}^{e/o}$ is converted into gate-voltage spacing $S_\mathrm{e/o} = \eta^{-1} E_\mathrm{c} \Delta N_\mathrm{g}^{e/o}$. Therefore, the peak spacing difference in gate-voltage is $S = (S_\mathrm{e} - S_\mathrm{o})$ and can be used to measure E_o by,

$$E_\mathrm{o} = \frac{\eta}{2} \left(S_\mathrm{e} - S_\mathrm{o} \right) \quad .$$

In the topological regime, MZMs cause $E_\mathrm{o} = 0$, and the CB perodicity is $1e$ with $S_\mathrm{e} = S_\mathrm{o}$.

5.2 IDENTIFYING ZERO-BIAS STATES

A false-colored micrograph of a Majorana island is shown in Fig. 5.1. The device was fabricated on a hybrid quantum well with a 7 nm epitaxial Al film selectively wet etched to form a 1.2 μm long stripe. Using the gate voltage V_pg the 2DEG surrounding the stripe was depleted forming the Majorana island. The gate-voltages $V_\mathrm{l,c}$ and $V_\mathrm{r,c}$ were used to form tunneling barriers at the ends of the wire.

In Fig. 5.2 the device is tuned into the Coulomb blockade regime by measuring the differential conductance G through the Majorana island. To isolate the island from the leads, two tunnel barriers were formed on either end of the device by tuning left ($V_{\mathrm{l,c}}$) and right cutter ($V_{\mathrm{r,c}}$) gate voltages (see Fig. 5.2a). The Coulomb blockade regime was reached when discrete charge transitions coupled to both cutter gate voltages were observed. Measurements similar to Fig. 5.2 were useful to determine the symmetry of the cutter voltages. To check if the peaks are $2e$ periodic at $B_{||} = 0$ T, either a finite bias V_{sd} or a finite magnetic field is used to check for peak doubling as shown in Fig. 5.2b.

Once stable CB is achieved, the hunt for Majorana signatures started with setting the parallel magnetic field $B_{||} = 2.2$ T *. MZMs should depend strongly on V_{pg} since it tunes the chemical potential of the island. In Majorana islands, the most telling transport signatures of MZMs are: 1) stable $1e$ periodic Coulomb peaks, 2) with a discrete zero-bias peak on the charge degeneracy point. 3) Both of these signatures should also be stable in both magnetic field and for some range in chemical potential.

In Fig. 5.2c the chemical potential and the charge occupancy is tune with V_{pg} and the tunnel barriers are symmetrically tuned with $V_{\mathrm{l/r,c}}$. Promising regions of parameter space were identified by observing horizontal regions of $1e$ periodic peak spacings. Figure 5.2d shows a cut at $V_{\mathrm{tb,c}} = -0.64$ V, where the evolution of the CB peak spacing in V_{pg} is shown. At $V_{\mathrm{pg}} = -0.915$ V the CB peaks are $2e$ periodic that split to an e-o periodicity at $V_{\mathrm{pg}} \sim -0.93$ V and becomes $1e$ periodic between $-0.94\text{ V} < \mathrm{V_{pg}} < -0.93$ V.

The observation of stable $1e$ peak spacing is consistent with the presence of a discrete zero energy state, however, additional spectroscopic information is needed to elucidate the origin of $1e$ periodicity. The cause of $1e$ periodicity could be due: 1) the normal state transition, 2) enhanced quasiparticle poisoning (so-called ghost peaks) [112], or 3) a sub-gap state at zero energy [77, 109]. Therefore, $1e$ periodicity alone is not sufficient evidence to draw conclusions about MZMs. It is important to observe a transition for $2e$ which split into $1e$ peaks without seeing an increase in ghost peaks. This can be investigated by both magnetic field dependence of the CB peak spacing and by tunneling spectroscopy, which is focused on next.

Figure 5.3a studies the evolution of the CB peaks in a parallel magnetic field. We observe $2e$ periodic CB peaks for $B_{||} < 1.75$ T, which split and become $1e$ periodic above 2 T. In Fig. 5.3b the average peak spacing difference $\langle S \rangle = \langle S_{\mathrm{e}} \rangle - \langle S_{\mathrm{o}} \rangle$ is constant from $B_{||} = 0$ to 1.5 T due to $2e$ transport, which transitions to $\langle S \rangle = 0$ at 2 T. This indicates that the energy E_{o} is

---

*This is the field value where the majority of stable zero-bias peaks were found in various device geometries.

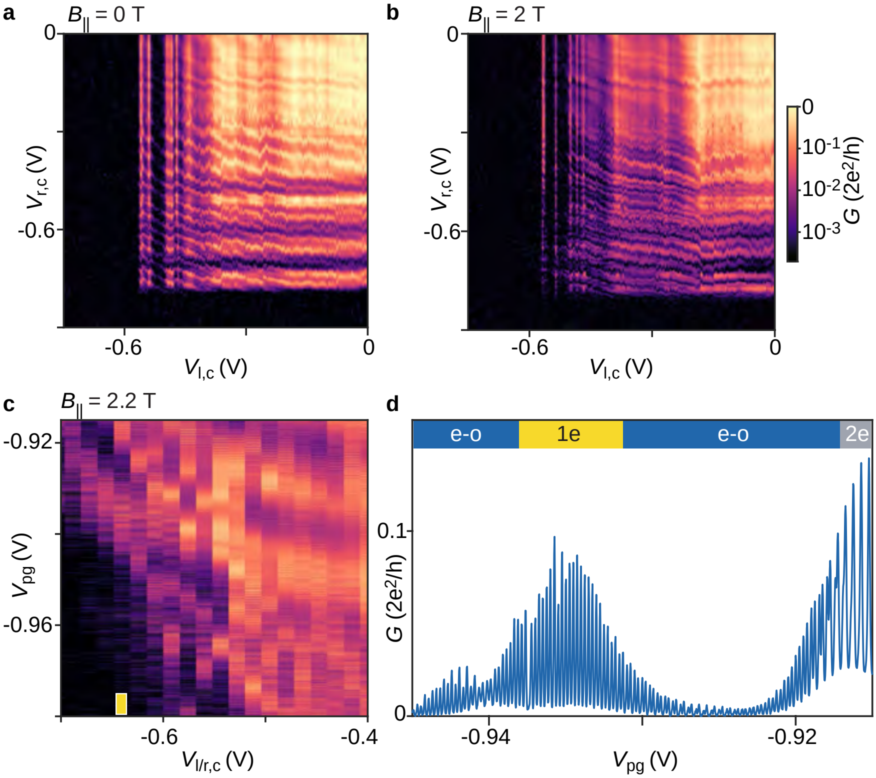

Figure 5.2: Coulomb blockade: a,b, Differential conductance G measured as a function of the two tunnel barrier voltages $V_{\mathrm{r,c}}$ and $V_{\mathrm{l,c}}$ at $B_{||} = 0$ T and $B_{||} = 2$ T. **c**, Differential conductance G measured as a function of V_{pg} and symmetric cutter voltages $V_{\mathrm{l/r,c}}$ at $B_{||} = 2.2$ T and a 1D cut at $V_{\mathrm{lr,c}} \sim -0.64$ V is shown in **d**.

lowered to zero at 2 T and remains until the normal state transition.

Measuring the conductance G as a function of bias voltage V_{sd} and V_{pg} yields spectroscopic details of the system. In Fig. 5.3c, Coulomb diamonds are measured for increasing $B_{||}$. At low fields ($B_{||} < 1.5$ T), the diamonds are $2e$ periodic at zero-bias and $1e$ periodic at finite bias. At $B_{||} = 1.75$ T, a transition to e-o, peak spacing occurs, which become $1e$ at $B_{||} = 2.5$ T. In the $1e$ regime, each of the charge degeneracy points has a zero-bias peak, indicating a discrete state zero-energy state, which is distinctly different from the normal state $1e$ periodicity at $B_{||} = 3.5$ T.

To corroborate the observation of a discrete zero-energy state, bias spectroscopy can be performed at a fixed gate voltage. The technique was introduced in Ref [113] and used in Ref [77] for sub-gap state spectroscopy. Effectively, this method tracks the energy of the excited state of the Coulomb diamond. First the gate-voltage value needs to be determined. The energy difference between $E_{\mathrm{N}+1}$ and E_{N} found to be

$$E(N+1) - E(N) = E_{\mathrm{c}}\left(2N + 1 - 2N_{\mathrm{g}}\right) + E_{\mathrm{o}} \quad .$$

By setting $N_{\mathrm{g}} = N + 1/2$, the energy to the nearest charge degeneracy occurs at $E_{\mathrm{N}+1} - E_{\mathrm{N}} = E_{\mathrm{o}}$. Therefore, fixing $N_{\mathrm{g}} = N + 1/2$ allows for spectroscopy of the lowest sub-gap state by applying a bias voltage, where $E_{\mathrm{o}} = \frac{eV_{\mathrm{sd}}}{2}$ [77, 113]. This gate voltage position corresponds to the leads aligning with the center of the superconducting gap at $B_{||} = 0$ and $V_{\mathrm{sd}} = 0$ and with the charge degeneracy of $1e$ periodicity at high field (see dashed line in Fig. 5.3a).

Figure 5.3d employs this technique to measure $E_{\mathrm{o}}(B_{||})$ by fixing V_{pg} to the dashed line in Fig. 5.3a. At $B_{||} = 1.5$ T a discrete state is observed to separate from the superconducting gap, and form a zero-bias peak above 2 T. This behaviour of E_{o} is in agreement with the Coulomb blockade peak spacing analysis of E_{o} shown Fig. 5.3b.

The observations in Fig. 5.2 and 5.3 are in support of the MZM interpretation with the the zero-bias peak arising from a discrete state in both V_{pg} and $B_{||}$. The results in Chapter 6 yield further evidence in support of the MZM interpretation, where phase coherent transport is investigated through Majorana islands.

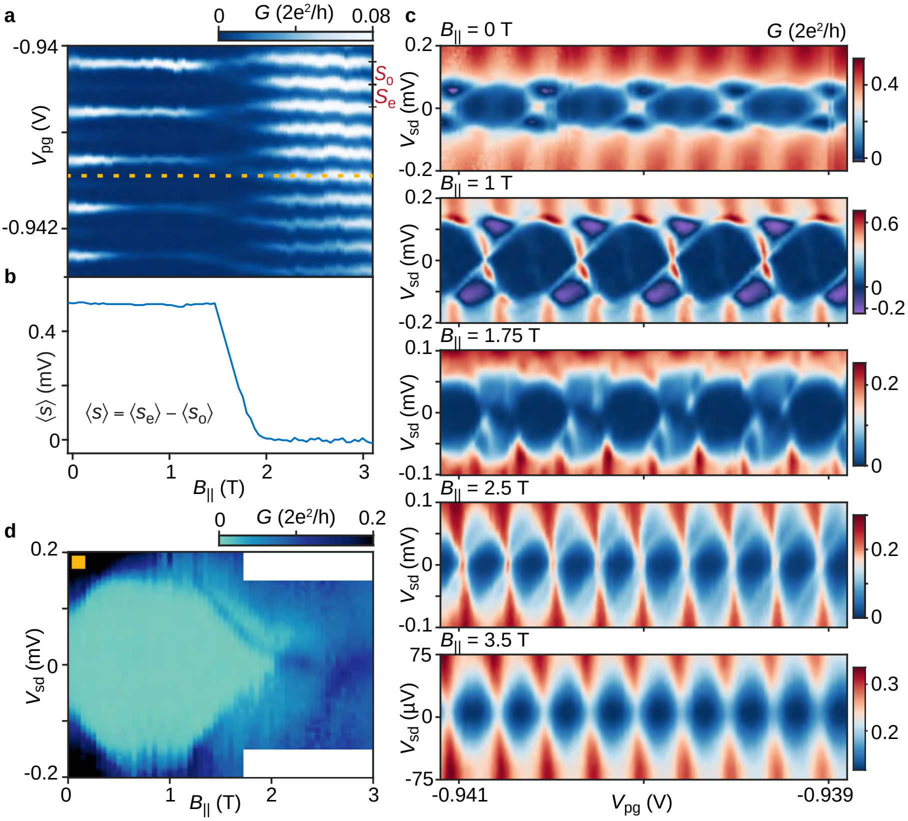

Figure 5.3: **Majorana island spectroscopy:** **a**, Zero-bias differential conductance G as a function of $B_{||}$ and V_{pg} and corresponding peak spacing analysis $\langle S\rangle = \langle S_e\rangle - \langle S_o\rangle$ is shown in **b**. **c**, Differential conductance G as a function of V_{sd} and V_{pg} showing Coulomb diamonds for $B_{||} = 0$ T, 1 T, 1.75 T, 2.5 T, 3.5 T. **d**, Differential conductance G as a function of V_{sd} and $B_{||}$ for V_{pg} fixed at the value of the dashed line in **a**.

6

COHERENT TRANSPORT THROUGH A MAJORANA ISLAND IN AN AHARONOV-BOHM INTERFEROMETER

A. M. Whiticar*, A. Fornieri*, E. C. T. O'Farrell, A. C. C. Drachmann, T. Wang, C. Thomas, S. Gronin, R. Kallaher, G. C. Gardner, M. J. Manfra, C. M. Marcus, F. Nichele

This manuscript has been submitted as: arXiv:1902.07085

Spatially separated Majorana modes are expected to allow phase-coherent single-electron transport through a topological superconducting islands via a mechanism referred to as teleportation [26]. Here we experimentally investigate such a system by patterning an elongated epitaxial InAs-Al island embedded in an Aharonov-Bohm interferometer. With increasing parallel magnetic field, a discrete sub-gap state in the island was lowered to zero energy yielding persistent 1e-periodic Coulomb blockade (CB) conductance peaks (e is the elementary charge). In this condition, conductance through the interferometer was observed to oscillate in a perpendicular magnetic field with a flux period of h/e (h is Planck's constant), indicating coherent transport of single electrons through the islands, a signature of electron teleportation via Majorana modes.

---

*These authors contributed equally to this work

6.1 INTRODUCTION

Initial experiments reporting signatures of Majorana zero modes (MZMs) in hybrid superconductor/semiconductor nanowires focussed on zero-bias conductance peaks (ZBPs) using local tunnelling spectroscopy [79–82]. Subsequently, Majorana islands provided additional evidence of MZMs based on nearly $1e$-spaced CB peaks [77], and indicated a Rashba-like spin orbit coupling with the spin-orbit field lying in-plane, perpendicular to the wire axis [50]. Under some circumstances, these signatures can be mimicked by trivial modes [88, 111], motivating a new generation of experiments that explicitly probe non-local properties, which are more difficult to mimic. For instance, non-locality of MZMs was recently investigated by measuring the energy splitting induced by the interaction of a quantum dot and a zero-energy state in a hybrid nanowire [114].

Non-locality can also be accessed by interferometric measurements of a Majorana island, where CB couples separated MZMs and fixes fermion parity [26, 29, 115–117]. In the topological regime, a Majorana island can coherently transfer a single-electron between its two ends through MZMs [26, 115]. To demonstrate the effect, a Majorana island can be embedded in the arm of an Aharonov-Bohm (AB) interferometer. If single-electron transport in both the reference arm and the Majorana island is coherent, conductance through the interferometer is expected to show oscillations with a flux period h/e [26, 118]. The same approach was used to investigate coherent transport in semiconductor quantum dots [119–122].

6.2 DEVICES

Devices were fabricated using an InAs two-dimensional electron gas (2DEG) heterostructure covered by 8 nm of epitaxially grown Al [17]. The bare 2DEG (without Al) showed a phase coherence length of $l_\varphi \sim 4\ \mu$m (see Chapter 3). Figure 6.1a shows a micrograph of device 1 with a 1.2 μm long and 0.1 μm wide superconducting Al stripe formed by wet etching. Ti/Au top-gates were evaporated on top of a 25 nm HfO_2 dielectric grown by atomic layer deposition. We studied two lithographically similar interferometers with circumferences of 5.6 μm for device 1 and 5 μm for device 2.

Applying a negative voltage, V_{pg}, to the central gate serves two purposes. It depletes the 2DEG surrounding the Al wire to form both the Majorana island and the AB ring center and also adjusts the chemical potential and charge occupancy of the island. Energizing all exterior gates confines the 2DEG into an AB interferometer by connecting the Majorana island to a normal conducting reference arm. The resistance of the reference arm was independently tuned by a negative gate voltage V_c. A source-drain bias voltage (V_{sd}) was applied to one lead and the resulting current and four-terminal voltage was recorded. The in-plane magnetic fields $B_{||}$ and B_t, and perpendicular field, $B_\perp$, were controlled by a three-axis vector magnet.

6.3 MAJORANA ISLAND SPECTROSCOPY

At low temperatures, tunneling of single electrons onto a Majorana island with a superconducting gap Δ is suppressed by CB, except at charge degeneracies. When the lowest subgap state energy, E_0, exceeds the charging energy E_c, ground-state degeneracies only occur between even-occupied states, resulting in $2e$-periodic CB conductance peaks [110]. Odd-occupied ground states are lowered into the accessible spectrum by a Zeeman field, resulting in even-odd CB peak spacing when $0 < E_0 < E_c$. The difference in peak spacings between even and odd states, $S = S_e - S_o$, is proportional to E_0 [77] (see Fig. 6.1b). For well-separated MZMs, E_0 tends exponentially toward zero, yielding $1e$ periodic CB peaks with a discrete zero-bias state at consecutive charge degeneracy point [77, 109]. Both observations are necessary for a MZM interpretation. When MZMs are not widely separated, CB peak spacings oscillate with field and chemical potential [50, 77, 111].

We first investigated the Majorana island without interferometry by depleting a segment of the reference arm (see Fig. 6.1a). Figure 6.1b shows zero-bias differential conductance $G = dI/dV$ of the island as a function of parallel magnetic field $B_{||}$ and gate voltage V_{pg}, which controls the electron occupancy and chemical potential of the island. CB peaks are $2e$ periodic at zero field and split around 2 T, becoming $1e$ periodic as the sub-gap state moves toward zero energy (see Fig. 6.3a for peak spacing analysis). Performing CB spectroscopy, that is, measuring G as a function of both source-drain bias V_{sd} and V_{pg} reveals Coulomb diamonds (Fig. 6.1c-f). At low $B_{||}$, diamonds are $2e$ periodic with distinct negative differential conductance (Fig. 6.1c), which transition to an even-odd peak spacing difference at moderate fields (Fig. 6.1d), similar to previous work on superconducting Coulomb islands [50, 77, 110, 113, 123–125]. At high fields, the $1e$ periodic diamonds show a discrete ZBP for consecutive charge degeneracy points that is well separated from the superconducting gap (Fig. 6.1e). This sub-gap feature remained at zero bias until the superconducting gap closure, and persists for 3 mV in V_{pg}, corresponding to an energy range of 0.8 meV. The stability of the zero-bias state in both magnetic field and in chemical potential is consistent

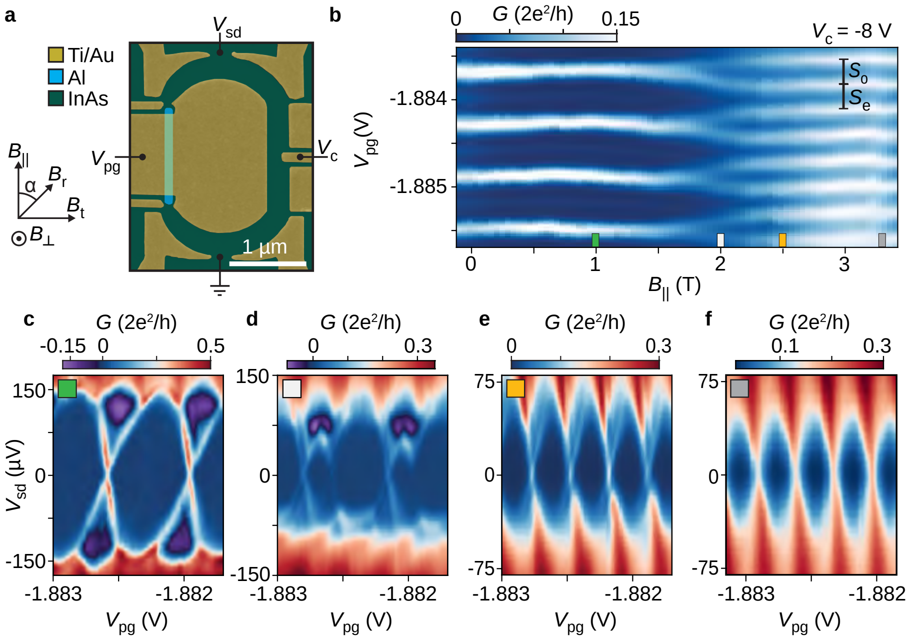

Figure 6.1: Majorana island interferometer. **a**, False-colour electron micrograph of the Majorana island interferometer where an Al wire (light blue) is embedded in a normal conducting Aharonov-Bohm interferometer (green) defined by Ti/Au gates (yellow). The gate voltage V_{pg} defines both the Majorana island and the interferometer center, and controls the electron occupancy. The gate voltage V_c controls the resistance of the reference arm and V_{sd} is the source-drain dc bias voltage. Magnetic field directions are shown with α denoting the in-plane angle measured with respect to the wire direction. **b**, Zero-bias differential conductance G as a function of $B_{||}$ and V_{pg}. S_e (S_o) is the even (odd) CB peak spacing. **c-f**, Differential conductance G as a function of V_{sd} and V_{pg} showing Coulomb diamonds for $B_{||} = 1$ T (**c**), 2 T (**d**), 2.5 T (**e**), and 3.3 T (**f**). The measurements shown in panels **b-f** were taken with the reference arm closed.

with the MZM picture (see Supplementary Fig. 6.5) [77], however, the observation of coherent single-electron transport is needed to draw conclusions about non-locality. Below, we show that the zero-bias state was sensitive to rotations of the in-plane field. The magnitude of $B_{||}$ where $1e$ periodicity is observed is in agreement with ZBPs measured in tunneling spectroscopy in InAs 2DEGs [81]. In contrast, as a function of B_t the peak spacing remained even-odd, and no consecutive ZBPs were observed (see Supplementary Fig. 6.6d-f). The normal state $1e$ regime of the Majorana island appears above $B_{||} \sim 3$ T with $E_c = 80\ \mu$eV (Fig. 6.1f), where no discrete ZBPs are observed (see Supplementary Fig. 6.5 and 6.6a-c).

6.4 INTERFEROMETRY

The reference arm of the AB interferometer was connected to the Majorana island by tuning V_c from -8 V to -3 V while V_{pg} was compensated. This lifted the overall conductance by opening a path through the reference arm (see Fig. 6.2a-d). Figure 6.2e-h shows the conductance ΔG through the full interferometer (with smooth background subtracted; see methods) as a function of $B_\perp$ and gate voltage V_{pg}, which control the flux in the interferometer and occupancy of the island, respectively. Figure 6.2e shows small oscillations in $\Delta G(B_\perp)$ at $B_{||} = 0$ T for the $2e$ periodic peaks. For $B_{||} = 2.2$ T, where the peak spacing was even-odd (Fig. 6.2f), the conductance showed moderate oscillations with a period $\Delta B_\perp = 1.5$ mT. The period $\Delta B_\perp$ is consistent with a single flux quantum h/e piercing the interferometer, indicating coherent $1e$ transport through both arms of the interferometer. At $B_{||} = 2.7$ T, the CB peak spacing was uniformly $1e$, and oscillation amplitude was maximal (see Figs. 6.2g). When the Majorana island was driven normal, $B_{||} > 3$ T, conductance oscillations were reduced, becoming comparable to the low field oscillations (Fig. 6.2h). The appearance of strong h/e periodic conductance oscillations in the $1e$ regime of the island is a key experimental signature of electron teleportation.

The strength and periodicity of the oscillations were examined more quantitatively using Fourier power spectrum (PS) analysis (see methods). In Figs. 6.2i-l, the PS of $\Delta G(B_\perp)$ are shown. Increasing $B_{||}$ led to a peak appearing around $f = 0.65\ \mathrm{mT}^{-1}$, the frequency expected for AB interference. The PS is maximized in the $1e$ regime. To quantify the oscillations amplitude, $\langle \tilde{A} \rangle$, we average the integrated PS (see methods).

We next correlate the $B_{||}$ dependence of the oscillations amplitude, $\langle \tilde{A} \rangle (B_{||})$, with the $B_{||}$ dependence of the lowest sub-gap state, $E_0(B_{||})$, of the island. The sub-gap energy is found from the difference between even and odd CB peak spacings, averaged separately, $\langle S \rangle = \langle S_e \rangle - \langle S_o \rangle$ (see Fig. 6.1b). In Figure 6.3a, $\langle S \rangle$ remains constant as a function of $B_{||}$ (indicating $2e$ transport) until a sub-gap state moves below E_c, reaching zero at 2.2 T without overshoot (as expected for well separated MZMs in a long wire [77, 109]). At low fields, where the CB periodicity was $2e$, the oscillation amplitude $\langle \tilde{A} \rangle$ is small (Fig. 6.3b). When $\langle S \rangle$ approaches zero at high fields ($B_{||} > 2$ T), $\langle \tilde{A} \rangle$ exhibits a sharp increase that coincides with the $2e$ to $1e$ transition. Above 3 T, the device was in the normal state and $\langle \tilde{A} \rangle$ returned to the low value

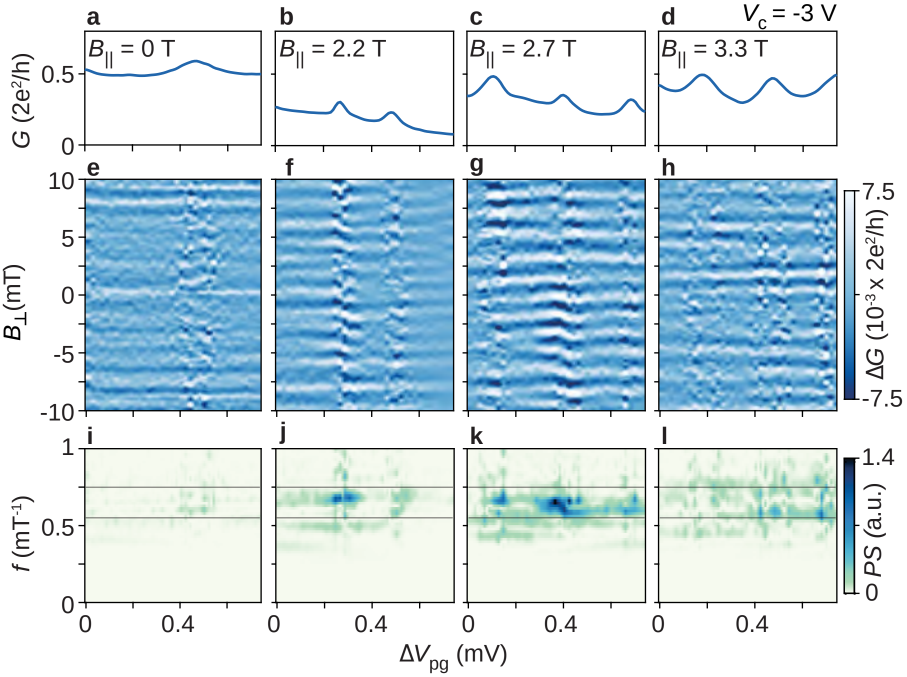

Figure 6.2: h/e **periodic conductance oscillations**. Magnetoconductance for parallel field values $B_{||} = 0$, 2.2, 2.7, and 3.3 T (left to right). **a**-**d**, Zero-bias differential conductance $G(B_\perp = 0)$ versus gate voltage $V_{\rm pg}$ used to control electron occupation. **e**-**h**, Conductance ΔG as a function of $V_{\rm pg}$ and perpendicular magnetic field $B_\perp$ controlling the flux in the interferometer with corresponding power spectrums in **i**-**l**. The solid black lines indicate the frequency window bounding the Aharonov-Bohm oscillations (see methods). ΔG is the conductance with a subtracted slowly varying background. $\Delta V_{\rm pg} = 0$ corresponds to $V_{\rm pg}$ = -1.896 V.

found in the $2e$ regime. This comparison shows that the oscillation amplitude is correlated with the energy of the lowest subgap state, and is maximal in the $1e$ superconducting regime, as expected for electron teleportation.

Figure 6.3c,d shows a similar study for device 2. In Fig. 6.3c, $\langle S\rangle$ shows strong even-odd below 1 T, fluctuates around $\langle S\rangle = 0$ between 1-2 T, then settles to $1e$ ($\langle S\rangle = 0$) above 2 T. CB spectroscopy reveals a discrete state that oscillates around zero energy in both $B_{||}$ and $V_{\rm pg}$ without forming a stable $1e$ periodic zero-bias peak (see Supplementary Fig. 6.8). This be-

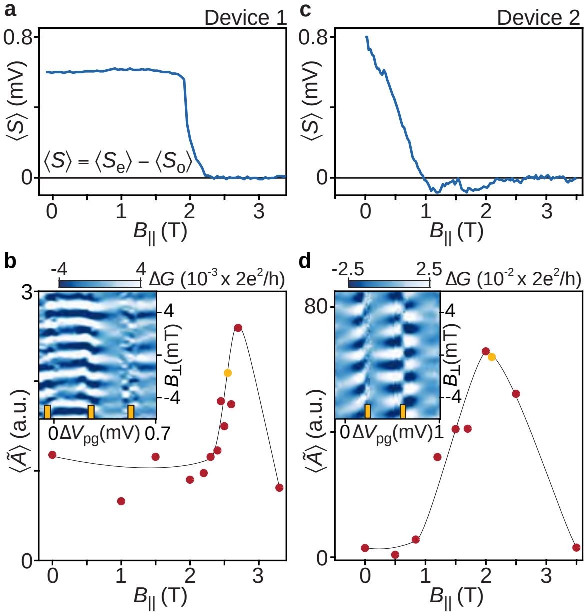

Figure 6.3: Coherent single-electron transport a,c, Peak spacing difference $\langle S\rangle$ as a function of parallel magnetic field $B_{||}$ for devices 1 and 2. **b,d**, Aharonov-Bohm oscillation amplitude $\langle\tilde{A}\rangle$ as a function of $B_{||}$. The solid line is a guide to the eye. Insets show characteristic magnetoconductance ΔG as a function of gate voltage V_{pg} controlling electron occupancy and perpendicular magnetic field $B_{\perp}$ controlling the magnetic flux in the interferometer in the $1e$ regime (indicated by yellow markers in the main panel). Yellow ticks show CB peak positions. $\Delta V_{\mathrm{pg}} = 0$ corresponds to $V_{\mathrm{pg}} =$ -1.896 V and -0.945 V for **b** and **d**, respectively.

haviour is compatible with hybridized MZMs or extended Andreev bound states (ABS) [50]. Figure 6.3d shows that phase coherent transport first appears above 1 T and $\langle\tilde{A}\rangle$ gradually increases until reaching a maximum amplitude for $1e$ peak spacing at 2.1 T, before diminishing in the normal state. In comparison to device 1, phase coherent transport appears before $1e$ peak spacing, suggesting that extended modes may also contribute to coherent transport.

6.5 TRANSMISSION PHASE SHIFTS

We observe that conductance oscillations measured on opposite sides of a CB peak in the $1e$ regime are out of phase (see yellow ticks in the insets of Fig. 6.3) indicating a transmission phase shift of π is acquired when the parity of the island is flipped (also see Fig. 6.9). This demonstrates interferometric detection of island parity, a feature of several recent topological qubit proposals [29, 32, 33]. In some cases, however, we found that the the phase shift was restored through the CB valley, such that the same sides of adjacent CB peaks have the same phase. What determines whether there is phase recovery in the CB valley is not currently understood (see Supplementary Fig. 6.9 and Fig. 6.10) [117, 120–122].

6.6 MAGNETIC FIELD ROTATIONS

The angular dependence of the in-plane magnetic field was investigated by fixing the field magnitude $B_r = 2.5$ T and rotating the field by an angle α (see Fig. 6.1). Theoretically, a rotation of the in-plane field towards the Rashba field direction is expected to close the topological gap [78]. Figure 6.4a shows $1e$ periodic Coulomb diamonds at $B_{||} = 2.5$ T with a discrete ZBP at each charge degeneracy point (similar to Fig. 6.1e). Rotating by an angle $\alpha = 5^\circ$ lifted the discrete state from zero energy, leading to even-odd peak spacing; at $\alpha = 10^\circ$, $1e$ periodicity was recovered, though without a discrete ZBP. The observed sensitivity of the zero-energy state to in-plane field rotation is consistent with MZMs [78].

Small rotations ($|\alpha| < 7.5^\circ$) reduced the oscillation amplitude, $\langle \tilde{A} \rangle$, as expected for even-odd periodicity (see Fig. 6.3). However, at larger angles ($|\alpha| > 10^\circ$) where the discrete ZBP was absent, a strong interference signal was observed (Fig. 6.4d). The observation of coherent transport in the absence of a discrete zero-energy state suggests trivial extended modes are also phase coherent over the length of the island. Therefore, the additional information provided by bias spectroscopy is needed to distinguish teleportation from other coherent transport mechanisms, as shown in Figs. 6.4a-c.

We further studied the effect of different magnetic field direction. The results are shown in Fig. 6.11. In summary, all three axes showed coherent transport, with oscillation amplitude first increasing as $\langle S \rangle$ approached zero. This shows that the oscillation amplitude is dictated by the energy E_0 in all field directions and indicates that interference is not unique to a parallel magnetic field, however, there is a distinction where the oscillation strength is maximized. This may reflect the Rashba SOI of the 2DEG (see Fig. 6.11), which leads to an anti-crossing

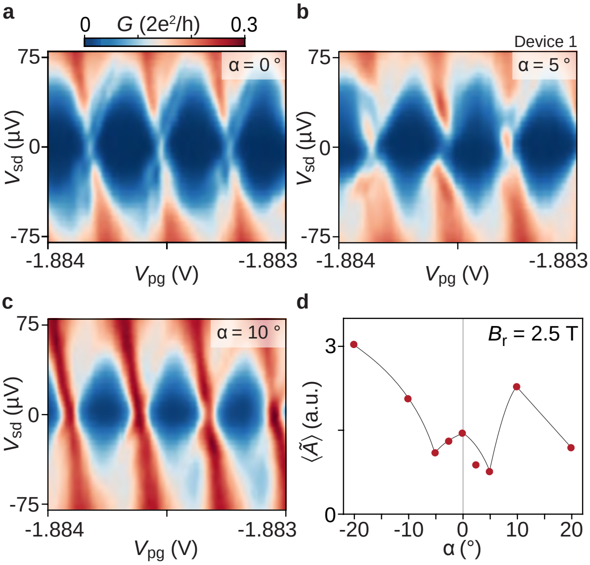

Figure 6.4: In-plane magnetic field rotations. **a-c**, Differential conductance G as a function of gate voltage V_{pg} controlling electron occupancy and source-drain bias voltage V_{sd} showing Coulomb diamonds for in-plane rotation angles of $\alpha = 0$ (**a**), 5° (**b**), and 10° (**c**) with $\alpha = 0$ corresponding to $B_{||} = 2.5$ T. **d**, Oscillation amplitude $\langle\tilde{A}\rangle$ as a function of in-plane rotation angle α for $B_r = 2.5$ T. The solid line is a guide to the eye.

of iso parity modes for $B_{||}$, while B_t (aligned to the spin-orbit field) allows for crossing of modes [50].

6.7 Discussion and conclusions

Finally, we comment on the physical mechanism that correlates the oscillation amplitude to the energy of E_o. At low fields, the Majorana island favours an even parity where transport of electrons occurs as two sequential tunneling events on either end of the island [110, 124]. The two electrons acquire the condensate phase when forming a Cooper pair, which suppresses single-electron coherence. At moderate fields, a discrete sub-gap state is brought below E_c and a single-electron transport channel is opened, allowing coherent resonant tunneling through the Majorana island. When the discrete state is brought to zero-energy, the contribution of coherent transport is increased due to electron teleportation. Finally, in the normal state, we interpret the reduction in interference signal to reflect the short coherence length in the diffusive Al wire.

In conclusion, we report signatures of single-electron teleportation via MZMs using AB interference in combination with spectroscopy of a discrete zero-energy state. Our results also reveal that coherent transport by topologically trivial modes extending over the full length of the Majorana island are allowed. These extended trivial modes may be precursors of topological states [126]. We have shown that interferometry accompanying bias spectroscopy revealing $1e$ periodic CB with discrete zero-bias states can discriminate MZMs from extended modes. Increasing the wire length to greatly exceed the diffusive coherence length $\xi = \sqrt{\xi_0 \, l_e} \sim 1\ \mu\text{m}$ (for $\Delta = 75\ \mu\text{eV}$ at $B_{||} = 2.5\ \text{T}$), where ξ_0 is the clean coherence length and $l_e \sim 300$ nm is the semiconducting mean free path [52] will suppress $1e$ transport via trivial extended modes. The observation of coherent transport through the island rules out localized ABS at the ends of the wire as the source of the studied zero-bias state. Indeed, transport flips the parity of localized modes and suppresses interference, while transport through MZMs preserves island parity and coherent transport [115, 116]. These localized modes could have been a possible interpretation of the previously observed ZBPs in single-end tunneling experiments [126].

These results suggest that InAs-Al 2DEGs are a promising route towards more complex experiments related to the braiding or fusion of MZMs. We have established coherent transport and parity readout from the transmission phase shifts in Majorana islands, two key results for future topological qubit networks [29, 32, 33]. Future devices will take advantage of improved material quality to allow for increased wire lengths to suppress coherent trivial quasiparticle transport, allowing MZM contributions to be better separated from other potential contributions.

METHODS

The devices were fabricated on wafers grown by molecular beam epitaxy on a InP substrate. The wafer stack consists of a 1 μm graded $\mathrm{In_{1-x}Al_xAs}$ insulating buffer, a 4 nm $\mathrm{In_{0.81}Ga_{0.19}As}$ bottom barrier, a 5 nm InAs quantum well, and a top barrier consisting of 5 nm $\mathrm{In_{0.9}Al_{0.1}As}$ for device 1 and 10 nm $\mathrm{In_{0.81}Ga_{0.19}As}$ for device 2. A 7 nm film of epitaxial Al was then grown in-situ without breaking the vacuum of the chamber. The InAs 2DEGs were characterized with a Hall bar geometry (Al removed), which showed a peak mobility of $\mu = 17,000\,\mathrm{cm^2V^{-1}s^{-1}}$ for an electron density of $n = 1.7\times10^{12}\,\mathrm{cm^{-2}}$ and $n = 7.5\times10^{11}\,\mathrm{cm^{-2}}$ for device 1 and device 2, respectively.

To highlight the oscillating components of the differential conductance $G(B_\perp)$, a smooth background was subtracted with a low-degree polynomial Savitzky-Golay filter resulting in ΔG [127]. Analysis of the oscillations was performed by first performing a fast Fourier transform $F(f)$ of $\Delta G(B_\perp)$ using a Hanning window then calculating the power spectral density $PS(f) = |F(f)|^2$. The oscillation amplitude $\langle\tilde{A}\rangle$ was obtained by averaging integrated power spectra. The integration was limited to a band in frequency between $f_1 = 0.55\ \mathrm{mT^{-1}}$ and $f_2 = 0.75\ \mathrm{mT^{-1}}$, spanning the range of a single flux quantum $\Phi_0 = h/e$ through the area A defined by either the central gate ($A_1 = 2.25\ \mu\mathrm{m}^2$) or the exterior gates ($A_2 = 3.1\ \mu\mathrm{m}^2$), where $f = A/\Phi_0$ (see Figs. 6.2i-l).

6.8 Supplementary Information

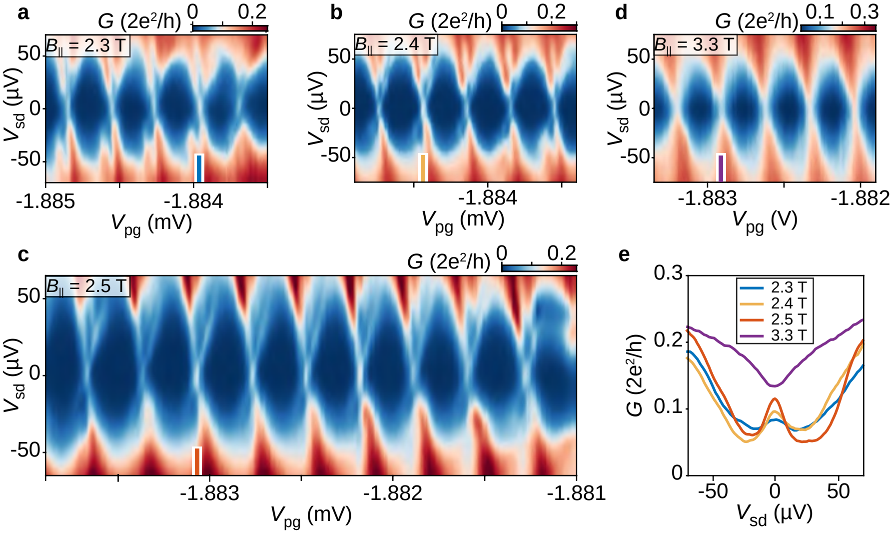

Figure 6.5: Stability of the zero-bias state c-f, Differential conductance G as a function of V_{sd} and V_{pg} showing Coulomb diamonds for $B_{\|} = 2.3$ T (**a**), 2.4 T (**b**), 2.5 T (**c**), and 3.3 T (**d**). **e**, Line cuts of G vs V_{sd} at charge degeneracy showing a discrete zero bias peak in the $1e$ regime and a zero-bias dip in the normal state. The measurements were taken in the same gate configuration as Fig. 6.1

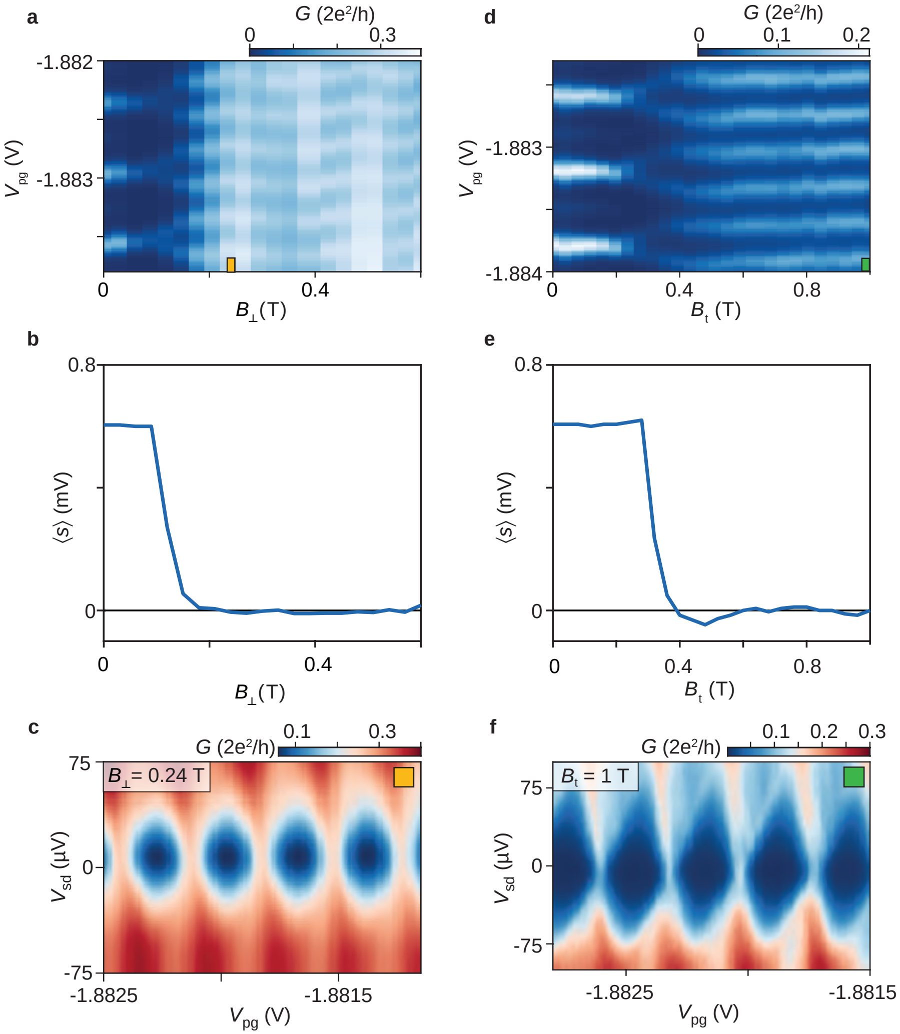

Figure 6.6: Transverse and perpendicular fields for device 1 in the regime of Fig. 6.1. **a**, Zero-bias differential conductance G as a function of gate voltage V_{pg} controlling electron occupancy and perpendicular field, $B_{\perp}$. **b**, CB peak spacing difference $\langle S \rangle$ as a function of $B_{\perp}$. **c**, Differential conductance G as a function of source-drain bias voltage V_{sd} and V_{pg} showing Coulomb diamonds for $B_{\perp} = 0.24$ T. **d**, Zero-bias differential conductance G as a function of V_{pg} and transverse field, B_{t}. **e**, CB peak spacing difference $\langle S \rangle$ as a function of B_{t}. **f**, Differential conductance G as a function of V_{sd} and V_{pg} showing Coulomb diamonds for $B_{\mathrm{t}} = 1$ T. The field directions are represented in Fig. 6.1a.

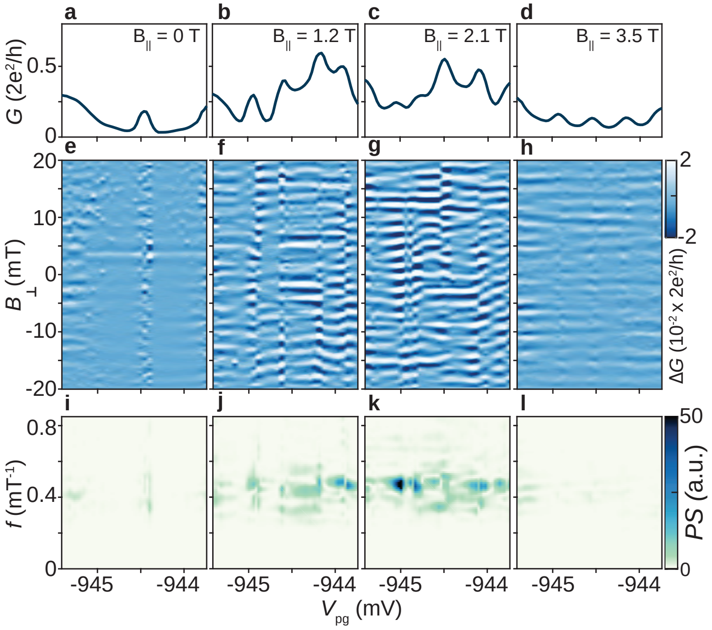

Figure 6.7: Conductance oscillations evolutions in parallel field for Device 2. Magnetoconductance for parallel field values $B_{\|} = 0$, 1.2, 2.1, and 3.5 T (left to right). **a**-**d**, Zero-bias differential conductance $G(B_{\perp} = 0)$ versus gate voltage V_{pg} controlling electron occupation. **e**-**h**, Magnetoconductance ΔG as a function of V_{pg} and perpendicular field $B_{\perp}$ controlling the flux in the interferometer with corresponding power spectra in **i**-**l**. A single flux quantum piercing the loop area $A_{\mathrm{loop}} \sim 1.8\ \mu\mathrm{m}^2$ corresponds to a frequency $f_{\mathrm{loop}} = A_{\mathrm{loop}}/(h/e) \sim 0.44$ mT^{-1}. **e**-**l**, a slowly varying background has been subtracted.

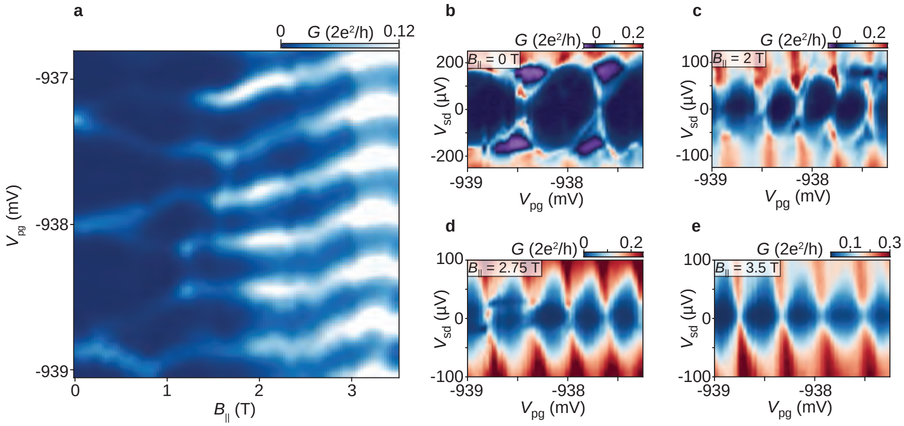

Figure 6.8: Coulomb blockade for device 2. **a**, Zero-bias differential conductance G as a function of parallel magnetic field $B_{||}$ and gate voltage V_{pg} controlling the electron occupancy with the reference arm closed. **b-e**, Differential conductance G as a function of voltage bias V_{sd} and V_{pg} for $B_{||} = 0$ T (**b**), 2 T (**c**), 2.75 T (**d**), and 3.5 T (**e**).

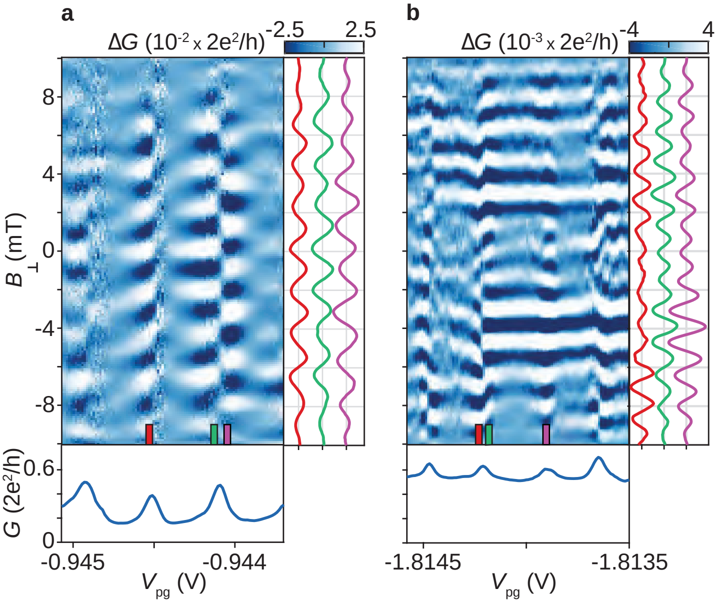

Figure 6.9: Transmission phase shifts: Top: Magnetoconductance ΔG as a function of V_{pg} and perpendicular magnetic field $B_\perp$ controlling the flux in the interferometer in the $1e$ regime for device 2 (**a**) and device 1(**b**) in the second gate configuration of device 1 (see Fig. 6.10). Bottom: $G(B_\perp = 0)$ versus gate voltage V_{pg} used to control electron occupation.

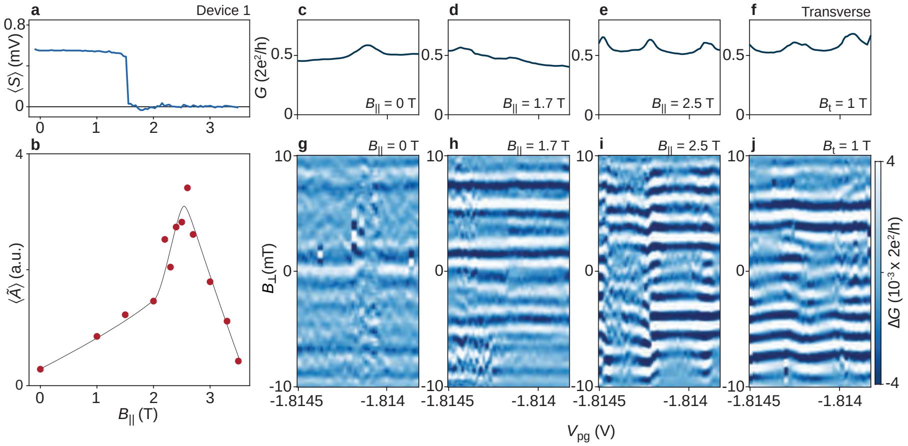

Figure 6.10: Second gate configuration of device 1. **a**, Peak spacing difference $\langle S \rangle$ as a function of parallel magnetic field $B_{||}$. **b**, Aharonov-Bohm oscillation amplitude $\langle \tilde{A} \rangle$ as a function of $B_{||}$. The solid line is a guide to the eye. **c-j**, Magnetoconductance for parallel magnetic fields $B_{||} = 0$ T, 1.7 T, and 2.5 T and transverse magnetic field $B_\mathrm{t} = 1$ T (left to right). **c-f**, Zero-bias differential conductance $G(B_\perp = 0)$ versus gate voltage V_pg used to control electron occupation. **g-j**, Magnetoconductance ΔG as a function of V_pg and perpendicular magnetic field $B_\perp$ controlling the flux in the interferometer.

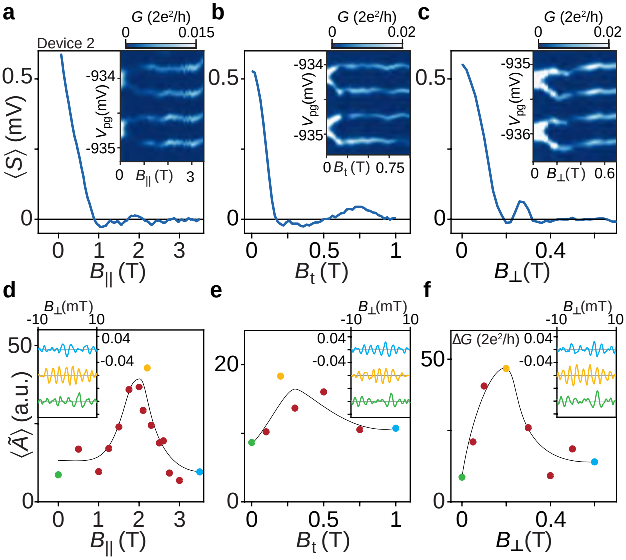

Figure 6.11: Orthogonal magnetic fields. **a**-**c**, Peak spacing difference $\langle S \rangle$ as a function of magnetic fields $B_{||}$, B_t, and $B_\perp$ for **a**, **b**, and **c**, respectively. Insets show the zero-bias differential conductance G as a function of magnetic field and gate voltage V_{pg} controlling electron occupancy with the reference arm closed. **d**-**f**, Oscillation amplitude $\langle \tilde{A} \rangle$ as a function of magnetic fields $B_{||}$, B_t, and $B_\perp$ for **d**, **e**, and **f**, respectively. The solid lines are a guide to the eye. Insets show magnetoconductance ΔG traces as a function of small perpendicular magnetic field $B_\perp$. Curves with the largest AB oscillation amplitude are shown for specific magnetic fields indicated by the marker color in the main panel.

IV

TOWARDS PARITY READOUT OF MAJORANA ZERO MODES

7

INTRODUCTION TO THE LOOP QUBIT

The experimental evidence of Majorana non-locality presented in chapter 6 was a prerequisite before moving towards the more challenging Majorana parity detection experiments. The following chapter will outline the parity-to-charge conversion scheme we are currently implementing in attempts to detect the joint parity of two MZMs. In chapters 8 and 9 I will expand upon the results of this chapter and discuss the progresses towards realizing Majorana parity readout in hybrid quantum well heterostructures.

7.1 MAJORANA PARITY

The prospect of utilizing MZMs to build a fault tolerant quantum computer relies on the ability to readout and manipulate quantum information stored in a fermionic parity of a non-local state. Figure 7.1 shows a single topological superconductor with two well separated MZMs γ_1 and γ_2 at the ends of the one-dimensional nanowire. These two MZMs constitute a single fermionic mode, which can be either occupied or unoccupied (see Chapter 1.2). The parity p of the MZMs is defined as,

$$p_{1,2} = i\gamma_1\gamma_2 = \begin{cases} 1, & \text{if occupied} \\ -1, & \text{if empty} \end{cases} .$$

Figure 7.1: Single topological nanowire with two Majorana zero modes γ_1 and γ_2

The Majorana parity is protected from local external perturbations by the topological gap [128]. For two well separated MZMs the two parity states are degenerate [30, 31, 128]. This degeneracy can be lifted by hybridizing two MZMs, causing a parity dependent energy splitting [30, 32]. This enables parity readout by parity-to-charge conversion mechanisms, such as Coulomb blockade [31], quantum dot hybridization [32, 33, 128] or interferometry [26, 29].

In the case of two topological wires, as depicted in Fig. 7.2a, the hybridization between the two inner Majoranas, γ_2 and γ_3, is mediated by a quantum dot (QD). This controlled hybridization forms the basis of the parity readout scheme envisioned by several 'measurement only' topological qubit proposals [32–34]. The qubit operation is referred to as measurement only because measurements are both used to readout and manipulate the quantum information stored in the Majorana parity.

Figure 7.2a shows a schematic representation of a device where two topological wires are connected by a trivial superconducting loop. This device geometry is referred to as a Loop Qubit and allows for the joint parity $i\gamma_2\gamma_3$ to be measured. By bringing a QD level into resonance allows for the inner Majoranas to hybridize. This causes a parity dependent energy splitting, which in turn alters the average occupation of the QD. This enables charge detection

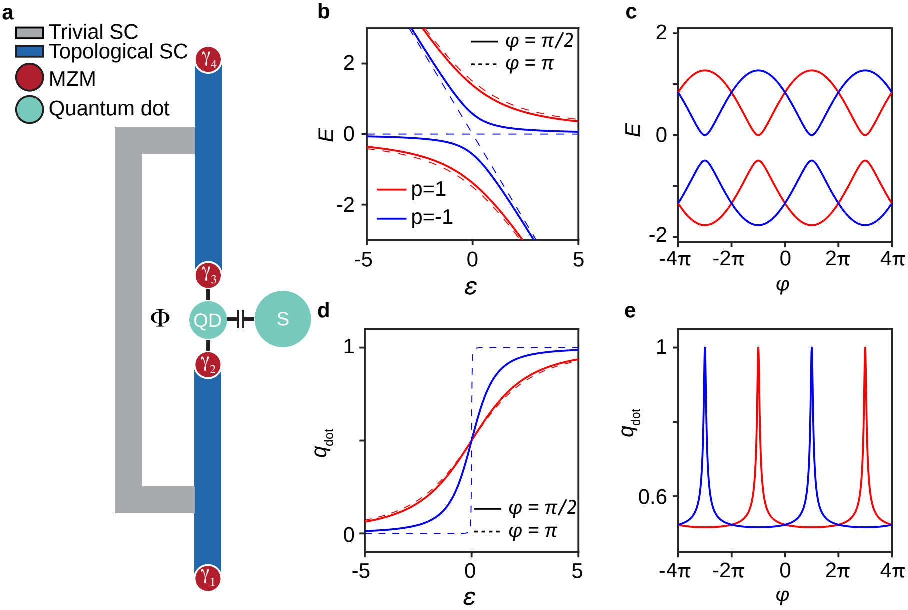

Figure 7.2: Loop Qubit: **a**, Schematic of a Majorana loop qubit. Two topological one-dimensional nanowires are connected by a trivial superconducting (SC) loop with four MZMs γ_1,γ_2,γ_3,γ_4. A quantum dot (QD) is used to control the hybridization of γ_2 and γ_3. The parity $p_{2,3}$ is readout by a nearby charge sensor (S). **b**, Parity dependent ground-state energy as a function of level detuning of the QD ε with different parities shown in red and blue and solid lines are for $\phi = \pi/2$ and dashed lines for $\phi = \pi$. **c**, Ground-state energies as a function of ϕ for $\varepsilon \sim 0$. **d,e**, Parity dependent charge occupation of the QD q_{dot} as a function of detuning ε (**d**) and phase different ϕ (**e**).

of joint parity measurements by employing charge sensing techniques.

A model of this system is constructed with two Majorana wires coupled by a QD with charging energy E_c, which forms a Josephson junction with a phase difference ϕ between the two topological wires. This system is described by the Hamiltonian [30, 32, 33],

$$H_{\text{tot}} = H_0 + H_{\text{QD}} + H_{\text{tunn}}$$

where H_0 describes a grounded s-wave proximitized Rashba nanowire tuned into the topological phase (see Chapter 2.4). In a low energy approximation (temperature $T \ll \Delta, E_c$), the superconductor contains only four MZMs: $\gamma_1, \gamma_2, \gamma_3, \gamma_4$ as shown in Fig. 7.2a. The charging energy associated with having n_f electrons on the QD is

$$H_\mathrm{QD} = E_\mathrm{c}\left(n_\mathrm{f} - n_\mathrm{g}\right)^2 \quad ,$$

where the offset charge $n_\mathrm{g} = C_\mathrm{g}V_\mathrm{g}/e$ is tuned by a gate voltage V_g and capacitance C_g. The QD is positioned between the two topological wires and is tunnel coupled to the inner MZMs, γ_2 and γ_3. The tunneling term,

$$H_\mathrm{tunn} = -i\frac{e^{i\varphi/2}}{2}\left(t_2 d^\dagger \gamma_2 + t_3 d^\dagger \gamma_3\right) + \mathrm{H.c.} \quad ,$$

describes a fermion hopping from the QD to the fermionic modes in the topological superconductor. The operators, $\frac{1}{2}e^{i\varphi/2}$ and $d^\dagger$ add an electron to the Majorana γ_i and QD, respectively [32, 33]. The hybridization of Majorana γ_i and the QD is determined by the tunneling amplitude t_i. The initial state of the system is considered to have tunneling turned off and the QD to be occupied while $\gamma_2\gamma_3$ is empty. Turning on the tunneling between the QD and the MZMs allows for a fermion to tunnel back and forth from the QD to a MZM, mixing the ground (QD occupancy) and excited states (MZM occupancy), which causes a shift on the ground state energy of the system that depends on the parity of the Majoranas (occupied or unoccupied) [30, 32] *. The spectrum of the system is given by [30],

$$E = -\frac{\varepsilon}{2} \pm \sqrt{\left(\frac{\varepsilon}{2}\right)^2 + t_2^2 + t_3^2 + 2p_{2,3}|t_2 t_3| \sin\left(\varphi/2\right)} \tag{7.1}$$

where ε is the detuning of the QD and the joint parity $p_{2,3} = \pm 1$. For $\varepsilon = 0$, the QD is on resonance. In Fig. 7.2b the spectrum is plotted as a function of detuning, showing that the energy separation between the two parities increases as the QD is brought into resonance†. In Fig. 7.2c, the spectrum is plotted in the vicinity of $\varepsilon = 0$ as a function of phase difference ϕ, where each parity branch oscillates with a 4π periodicity. The parity degeneracy can be restored by setting $\phi = 2n\pi$ for n as an integer. The maximum visibility between the two parity states is achieved for $\varepsilon = 0$ and $\phi = (2n+1)\pi$.

The parity dependence of the energy levels (shown in Fig. 7.2b,c) affects the occupancy of the QD, since either the electron is occupying the QD or the MZMs. Therefore, since the

---

*It is assumed that the length of the topological segments is long to avoid hybridization between $\gamma_1\gamma_2$ and $\gamma_3\gamma_4$ [25]

†We assume here that the tunneling amplitudes t_2, t_3 are symmetric, however, asymmetry or lower amplitudes will decrease the visibility

occupancy of the QD is sensitive to whether $\gamma_2\gamma_3$ is occupied, a capacitively coupled charge sensor can detect $p_{2,3}$. To illustrate the parity-to-charge conversion, the charge q_{dot} of the QD is calculated as a function of detuning and phase difference. The charge q_{dot} depends on the ground state of the spectrum as [25, 32]*,

$$q_{\mathrm{dot}} = e(n_{\mathrm{g}} - \frac{1}{2E_{\mathrm{c}}}\frac{\partial E_{\mathrm{GS}}}{\partial n_{\mathrm{g}}}) \quad .$$

Figure 7.2d,e shows that the different parity branches are distinguishable by the charge of the QD. In this case the maximum visibility between the two parity states is achieved for $\phi = (2n+1)\pi$ while ε needs to be slightly tuned away from zero. Since the measurement is performed in the ground state, an ideal measurement of q_{dot} is 4π periodic (see Fig. 7.2e). If poisoning processes are present, then the parity of the island will change on a timescale τ_p where the island will switch between the two parity states and a 2π periodicity is recovered.

7.2 TRIVIAL SUPERCONDUCTING LOOP

Quasiparticle poisoning can arise from both external and internal sources, leading to decoherence of the Majorana qubit. This is because a poisoning event will flip the Majorana parity and destroy the quantum information. External sources of poisoning include single electrons entering the island from the leads or similar mechanisms, which change the total parity of the island. External sources of poisoning can be reduced by having a finite charging energy [32], or by employing filter-gate techniques [129]. Internal sources can arise from non-equilibrium quasiparticle excitations or low energy sub-gap states that can be addressed by 1) going to sufficiently low temperatures to reduce thermally activated quasiparticles and 2) by ensuring the superconducting loop is a trivial superconductor without sub-gap states (the loop is colored grey in Fig. 7.2a). If there are sub-gap states present in the superconducting loop, they can cause unwanted hybridization between the MZMs or be a source of quasiparticle poisoning. In the following discussion it is shown how these low energy sub-gap states can be avoided in the construction of the superconducting loop.

A clear starting point for fabricating the superconducting loop for the loop qubit is to use the epitaxial Al. This avoids the detrimental ex-situ evaporation of Al or other superconductors, which involves aggressive and harmful milling procedures that lead to poisoning [129]. However, a challenge arises due to the Rashba SOI of the semiconductor and the alignment

---

*This is calculated by using the Hellmann-Feynman theorem of the magnetic field. To construct the loop, it is necessary to have a segment of the loop oriented perpendicular with respect to the topological wires. This segment will experience a transverse component of the applied external magnetic field used to drive the nanowires into the topological regime. A transverse magnetic field is parallel to the Rashba spin-orbit field of a one-dimensional wire and therefore the superconducting gap will close at much lower magnetic fields (see Chapters 2.2.2 and 2.4) [78].

To overcome the challenge of unwanted sub-gap states in the superconducting loop, it is investigated if sufficient depletion of the transverse segment could allow for a hard superconducting gap at high magnetic field. In Fig. 7.3a a Coulomb island is shown with a 20° rotation away from the parallel magnetic field, with a length of 900 nm and a width of 100 nm. Applying a purely parallel magnetic field will then impose a transverse component to the rotated wire. Typically, a parallel magnetic field $B_{||} \sim 2$ T is required to observe signatures of MZMs in one-dimensional nanowires, therefore, it is necessary for the loop to remain a bulk gapped superconductor until this magnetic field value [101, 106].

The energy of the lowest sub-gap state E_0 is examined using Coulomb blockade peak spacing difference $\langle S\rangle = \langle S_e\rangle - \langle S_o\rangle$ (see Chapter 5.1). Figure 7.3b-d shows the differential conductance G as a function of gate voltage V_{pg} and parallel magnetic field $B_{||}$, where the Coulomb island is tuned into the Coulomb blockade regime with a charging energy $E_c = 45\ \mu\text{eV}$. At $V_{pg} = -2$ V the peak spacing was $2e$ periodic when $B_{||} = 0$ T. Increasing $B_{||}$ caused the $2e$ periodic peaks to split at 0.68 T and become $1e$ periodic with strong oscillations in the peak spacing with field. This is due to a sub-gap state being lowered in energy below E_c (see Chapter 5.1). The normal state transition of the epitaxial Al film was independently measured to be $B_{||,c} = 2.5$ T [*]. If the Coulomb island was depleted further with $V_{pg} = -3$ V, the $2e$ to $1e$ transition was driven to higher magnetic fields (see Fig. 7.3c) with the $1e$ transition occurring above $B_{||} = 2$ T. Decreasing V_{pg} by a further -200 mV, the $1e$ transition occurs at $B_{||} \sim 2.4$ T.

The persistence of the $2e$ periodic peaks until $B_{||} \sim 2.4$ T is interpreted to indicate that the semiconductor below the Al Coulomb island is fully depleted, removing the presence of any unwanted of sub-gap states. This demonstrates that a 20° rotated segment can remain a superconductor without sub-gap states below 45 μeV when V_{pg} is sufficiently depleted.

---

[*] The lower critical field of $B_{||,c} = 2.5\ T$ observed in this wafer compared to the value reported in Chapter 3 is attributed to a thicker growth of Al on this wafer

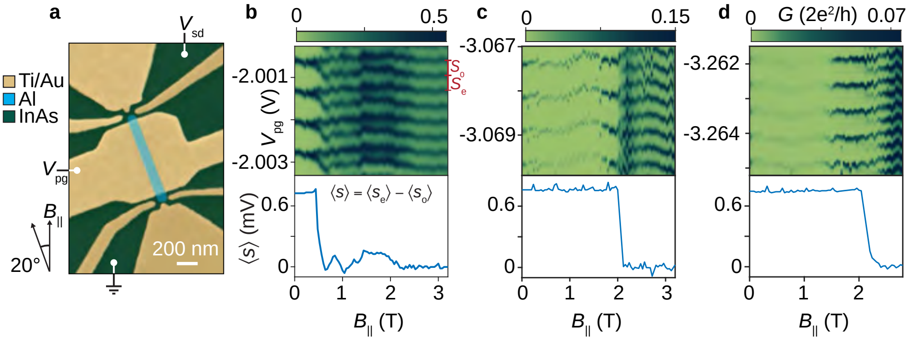

Figure 7.3: Rotated Coulomb island: a, False-coloured electron micrograph of a Coulomb island rotated 20° from a parallel axis. **b-d**, (Top panels) Differential conductance G as a function parallel magnetic field $B_{||}$ and gate voltage V_{pg} used to control the charge occupancy of the QD and the density in the Coulomb island. (Bottom panels) Coulomb blockade peak spacing analysis showing peak spacing difference $\langle S\rangle = \langle S_e\rangle - \langle S_o\rangle$ as a function of parallel magnetic field $B_{||}$. Note the lower magnetic field range in **d**.

8

MAGNETIC FIELD AND FLUX DRIVEN 0-π PHASE TRANSITION IN A SPINFUL JOSEPHSON JUNCTION

This chapter implements the rotated Coulomb island to construct a superconducting loop that connects two superconducting nanowires. This allows for the device schematic in Fig. 7.2a to be realized. This chapter investigates how to control and measure the quantum dot that is coupled to the two superconducting nanowires. A normal lead is used to perform tunneling spectroscopy of the formed between the two nanowires. Transport signatures of a spinful Josephson junction are observed consistent with a quantum dot confined between the two nanowires. Additionally, 0-π *phase transitions are observed by inducing zero-bias crossings that are tunable with magnetic field and the phase difference between the two nanowires.*

8.1 INTRODUCTION

The coexistence of magnetism and superconductivity in a Josephson junction can lead to a 0-π phase transition [58]. Quantum dots (QDs) can serve as spin impurities that can be controllably coupled to a superconductor (S) [130]. Here, the Andreev spectrum of a hybrid S-QD-S Josephson junction is probed by performing tunneling spectroscopy with a weakly coupled normal lead. A gate-voltage-induced transition from a singlet to a doublet ground-state is identified, where the Andreev spectrum develops a π-phase shift. Control of the 0-π transition is demonstrated using the superconducting phase difference across the junction and an external magnetic field. Parity transitions are identified by measuring zero-bias crossings induced by a magnetic field, phase difference, and gate voltage.

The proximity effect describes how superconducting order leaks into a material and form a unique hybrid system composed of properties of the constituents [53]. This allows for an innovative method for studying unconventional superconductivity without resorting to bulk material. Recently, the growth of epitaxial Al has led to highly transparent interfaces necessary for achieving a well-defined proximity effect (see chapter 2.3.3) [90, 94, 102].

When two superconductors (S) are connected by a short normal weak link (N), a supercurrent is carried by a discrete spectrum of Andreev bound states (ABS) existing below the superconducting gap Δ with energy E_{ABS} [63] (see chapter 2.3.4). These S-N-S junctions are objects of intense research and are the fundamental component of gate-tunable superconducting qubits and Andreev qubits, both requiring a few highly transmitting modes [131–133]. The Andreev spectrum is modified when magnetic order is induced into the weak link and can cause a transition from a non-magnetic 0-junction to a magnetic π-junction [134]. For instance, a ferromagnetic weak link induces an oscillating order parameter, which can lead to a phase difference $\phi = \pi$ across the junction [135].

An alternative approach to study the effect of magnetism on superconductivity is to confine a QD in the weak link [136–138]. The charging energy of the QD stabilizes single electron occupancies that form Yu-Shiba-Rusinov [139–141] bound states through exchange interaction with the S leads [142–144]. In a S-QD-S Josephson junction, where the QD consists of a single spin degenerate orbital level, two ground-states (GSs) are possible [145–147] (see supplementary Fig. 8.5). For an odd occupancy, the GS can either be a spin-degenerate magnetic doublet or a non-magnetic singlet. While the precise boundary between the two GSs is the result of a competition of microscopic details of the junction [145], experimentally it can clearly be distinguished by a fermion parity transition marked by a zero-bias crossing

(ZBC) [130]. In a S-QD-S junction, sub-gap resonances occur at E_{ABS} matching the energy difference between the GS and the excited state (ES) [130]. When the ES is brought to zero-energy, the GS and ES are degenerate and a 0-π phase transition occurs due to a fermionic parity change of the S-QD ground state (see yellow arrow in Fig. 8.5b) [148]. The tunneling of single-electrons into the junction yields spectroscopic information of the Andreev spectrum and allows for a 0-π transition to be identified by a ZBC [145, 148].

Previous experiments relied on a node in the critical current of a S-QD-S junction as an experimental signature of a 0-π transition. However, additional orbital effects may complicate this interpretation [149–151] (also see Fig. 10.6). Additional signatures involving the observation of supercurrent reversal using a superconducting quantum interference device (SQUID) [143, 152, 153] or by directly probing the Andreev spectrum [146, 147] can result in clearer experimental signatures. Indeed, tunneling spectroscopy in a N-QD-S geometry revealed a 0-π transition that is induced by a magnetic field [130] and in a S-QD-S Josephson junction by controlling the phase difference [147]. Theoretical studies of the QD-S system have predicted that a 0-π transition is possible with 1) a gate voltage, 2) magnetic field, and 3) phase difference [134, 145, 148]. To the best of our knowledge, this work is the first experiment addressing the combination of these three parameters on the 0-π phase transition.

In this chapter, the Andreev spectrum of a S-QD-S is directly measured by tunneling spectroscopy. This includes the observation of a singlet to doublet GS transitions by controlling the QD charge occupancy with a gate-voltage. In the singlet GS, a magnetic field induced 0-π transition is observed, which is lowered in magnetic field by controlling the phase difference across the junction, reaching $B_{||} = 0\,\text{T}$ at $\phi = \pi$. Within the gate-controlled doublet GS, the Andreev spectrum obtained a π-shift and a reduced phase dependence of E_{ABS} was observed. We determine the evolution of the 0-π phase transition by measuring ZBCs as a function of gate-voltage, magnetic field and phase difference.

8.2 DEVICE

Devices were fabricated using an InAs two-dimensional electron gas (2DEG) heterostructure covered by 8 nm of epitaxially grown Al, with an induced superconducting gap of $\Delta^* = 220\ \mu\text{eV}$. Figure 8.1a shows a micrograph of the device, where a superconducting loop has been selectively wet etched from the Al film. Ti/Au top-gates were evaporated on a 15 nm HfO_2 dielectric grown by atomic layer deposition. Applying negative gate voltages $V_{S,1/2}$ the two superconducting leads were defined, forming a ballistic Josephson junction. The QD be-

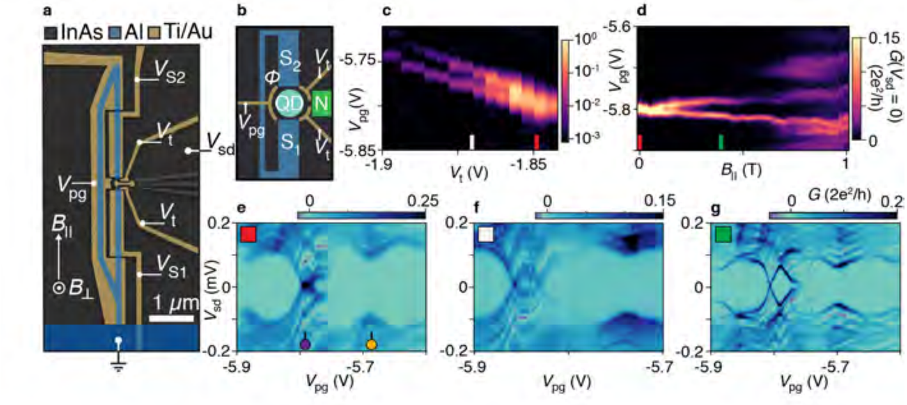

Figure 8.1: Spinful Josephson junction: **a**, False-colour electron micrograph of the superconductor-quantum dot-superconductor Josephson junction where an Al loop (blue) forms a Josephson junction with an embedded quantum dot defined by Ti/Au gates (yellow) with gate voltage V_{pg}. The tunnel barriers to the normal lead and superconducting leads are controlled by gate voltage V_t. A bias voltage V_{sd} is applied to the normal lead and the superconducting loop is grounded. Magnetic field directions are shown where $B_\perp$ is used to thread fluxes in the superconducting loop. **b**, Simplified sketch of the device. **c**, Zero-bias differential conductance G as a function of V_t and V_{pg}. **d**, Zero-bias G as a function of $B_{||}$ and V_{pg}. **e**, G as a function of V_{sd} and V_{pg} for $B_{||} = 0$ T and $V_t = -1.85$ V. **f**, G as a function of V_{sd} and V_{pg} for $B_{||} = 0$ T and $V_t = -1.87$ V. **g**, G as a function of V_{sd} and V_{pg} for $B_{||} = 0.4$ T and $V_t = -1.85$ V.

tween the two S leads was defined with a negative voltages V_{pg}. In Fig. 8.1b, a schematic of the transport configuration is shown, where a voltage bias was applied to a normal (N) lead and the resulting current and four-terminal voltage was recorded with the S loop grounded. The tunnel barriers to the N and S leads were controlled by gate voltage V_t, allowing for tunneling spectroscopy of the S-QD-S junction. The in-plane magnetic fields $B_{||}$ and perpendicular field, $B_\perp$, were controlled by a three-axis vector magnet. The superconducting phase difference ϕ across the junction was controlled by threading magnetic fluxes through the S loop with $B_\perp$. Previous measurements on similar material revealed a near unity transmission of the ABS in an SNS junction [94].

8.3 RESULTS AND DISCUSSION

Tunneling spectroscopy of the S-QD-S junction was performed by forming a tunnel barrier to the normal lead with $V_t = -1.85$ V (see Fig. 8.1b). In Fig. 8.1e the differential conductance, $G = dI/dV$, is shown as a function of the bias voltage V_{sd} and the gate voltage V_{pg} used to tune the occupancy of the QD. A superconducting gap $\Delta = 150\ \mu\text{eV} < \Delta^*$ is found, which indicates a strong QD-S hybridization. By changing V_{pg}, two distinct sub-gap features are observed. The first occurred at $V_{pg} \sim -5.7$ V (yellow marker), where E_{ABS} is reduced to 100 μeV. This is a signature of a Shiba-state and a parity conserving transition. Alternatively, by varying V_{pg} through -5.8 V (purple marker), a ZBC was observed. This crossing indicates a degeneracy between the singlet GS and doublet ES, and a gate-induced 0-π transition.

The doublet GS origin of the ZBC is verified by studying the dependence of the ZBC with V_t and parallel magnetic field $B_{||}$. Fixing $V_{sd} = 0$ in Fig. 8.1c shows that the ZBC splits and expands in V_{pg} with more negative V_t voltages. This reflects a decrease in coupling to the superconducting leads, which stabilizes the doublet GS in gate voltage (see supplementary Fig. 8.5a) [130, 145]. Moreover, applying $B_{||}$ lifts the spin degeneracy of the doublet, leading to the splitting observed in both Fig. 8.1d,g. In the following discussion the behaviour of the parity conserving transition (yellow marker) and the odd parity transition (purple marker) is investigated as a function of magnetic field and phase (see Fig. 8.1e for markers) .

8.3.1 EVEN PARITY GROUND STATE

We first investigate the even parity GS by fixing $V_{pg} = -5.69$ V. In Fig. 8.2a, the differential conductance G is measured as a function of ϕ and V_{sd}. As the phase difference across the junction is increased from 0 to π, the doublet ES moves to lower energy and crosses zero-bias at $\phi = \pi$. The strong dispersion of $E_{ABS}(\phi)$ indicates a highly transparent junction [63]. Applying a small parallel field, $B_{||}$, spin splits the doublet ES, leading to a gap opening about $\phi = \pi$ (marked by two ZBCs in Fig 8.2b). This gap indicates a phase tunable 0-π transition that grows with increasing field (see In Fig. 8.2a-d) [145].

Focusing on the $B_{||}$ dependence in the absence of a phase difference ($\phi = 0$) the zero-bias conductance $G(V_{sd} = 0)$ transitions from a minimum at $B_{||} = 0$ T to a maximum at 0.8 T. That is, the doublet ES is lowered with $B_{||}$ and a ZBC occurs at 0.8 T (see Fig.8.2d). At $B_{||} = 0.8$ T we observe that E_{ABS} acquires a π-shifted phase dependence compared to zero field, which is a predicted signature of a magnetic π-junction. In Fig. 8.2e, the ϕ and

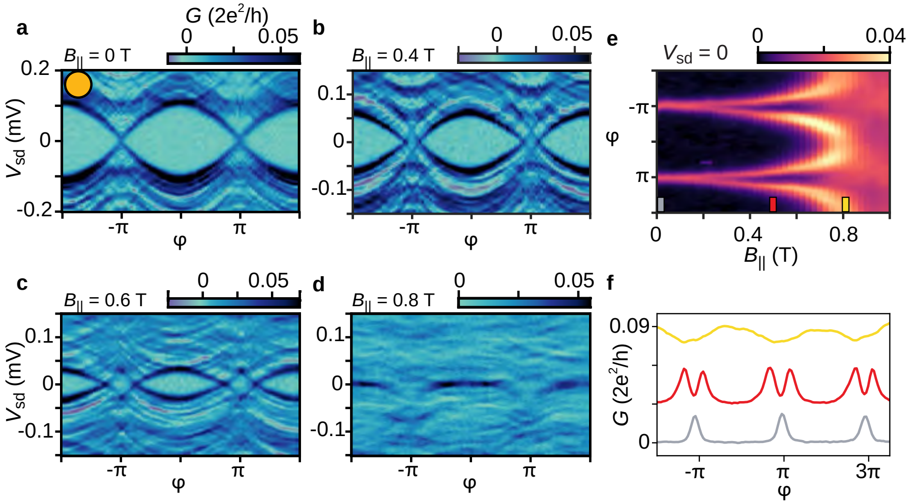

Figure 8.2: Even parity ground state: Differential conductance G as a function of superconducting phase difference ϕ and voltage-bias V_{sd} for $B_{||} = 0$ T (**a**), $B_{||} = 0.4$ T (**b**), $B_{||} = 0.6$ T (**c**), $B_{||} = 0.8$ T (**d**). **e**, Zero-bias G as a function of ϕ and $B_{||}$ with corresponding cuts in **f**.

$B_{||}$ dependence of the 0-π transition is captured by measuring $G(V_{\mathrm{sd}} = 0)$. Increasing the field causes the zero-bias crossing at $\phi = \pi$ to split, stabilizing a doublet GS in phase. At $B_{||} = 0.8$ T a ZBC occurs at $\phi = 0$. These results indicate that the combination of a magnetic field and a phase difference can control the 0-π transition in an even parity GS.

8.3.2 ODD PARITY GROUND STATE

The odd parity transition is investigated in Figure. 8.3 by fixing $V_{\mathrm{pg}} = -5.8$ V (see Fig. 8.1). Figure 8.3a shows the ABS crossing at $\phi = 0$ due to the spinful occupancy of the QD, which is π-shifted compared to Fig. 8.2. A reduced $E_{\mathrm{ABS}}(\phi)$ dependence is observed, similar to previous results on this system [147]. This weakened phase dependence is attributed to higher order transport processes associated with tunneling across a spinful junction [154]. Applying $B_{||} = 0.2$ T in Fig. 8.3b causes the singlet ES to move to finite bias, where a gap develops at zero-bias for all ϕ. In comparison to Fig. 8.2, no spin splitting of the ES is observed. This behaviour is explained by the decreasing energy of the doublet GS with increasing magnetic

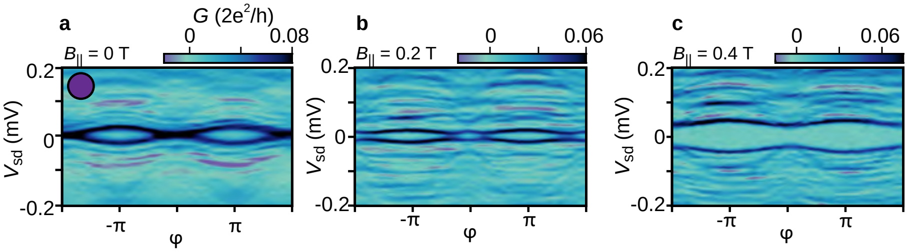

Figure 8.3: Odd parity ground state: Differential conductance G as a function of superconducting phase difference ϕ and voltage-bias V_{sd} for $B_{||} = 0$ T (**a**), $B_{||} = 0.2$ T (**b**), $B_{||} = 0.4$ T (**c**).

field due to spin splitting [130]. This in turn causes an increase in E_{ABS} with magnetic field, leading to the gap forming for all ϕ observed in Figure. 8.3c.

8.3.3 ZERO-BIAS CROSSINGS

We identify 0-π transitions by measuring ZBCs induced by a magnetic field, phase difference, and gate voltage in Fig. 8.4. At $B_{||} = 0$, the parity conserving transition observed in Fig. 8.2 is observed at $V_{\mathrm{pg}} = -5.7$ V marked by the ZBCs occurring at $\phi = \pi$. The odd parity transition examined in Fig. 8.3 is identified with the vertical band at $V_{\mathrm{pg}} = -5.8$ V. Indeed, the odd parity transition develops a π-shifted Andreev spectrum compared to the even parity ground state (see Fig 8.4b). Increasing $B_{||} = 0.2$ T causes the odd occupancy ZBC to split, stabilizing a doublet GS in both ϕ and V_{pg}. Further increasing $B_{||} = 0.4$ T causes the even parity ZBC at $\phi = \pi$ to split in both ϕ and V_{pg}. With increasing magnetic field, the doublet GS expands in both ϕ and V_{pg}, while the singlet GS shrinks.

8.4 CONCLUSION

In summary, the Andreev spectrum of a S-QD-S Josephson junction under the influence of gate voltage, magnetic field, and superconducting phase difference was measured. The combination of a magnetic field and a phase difference was observed to stabilize a π-junction. These results are important for the development of novel means of manipulating the spin of the ABS for coherent control of Andreev qubits.

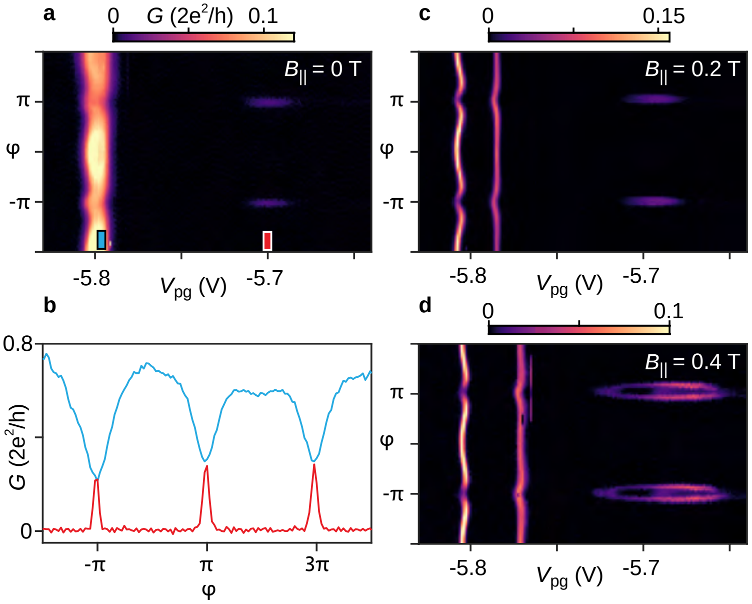

Figure 8.4: Zero-bias crossings: Zero-bias differential conductance G as a function of superconducting phase difference ϕ and gate voltage V_{pg} for $B_{\|} = 0$ T (**a**), $B_{\|} = 0.2$ T (**c**), $B_{\|} = 0.4$ T (**d**). **b**, Cuts of **a** for an even parity (red) and odd parity (blue) ground state.

8.5 Supplementary

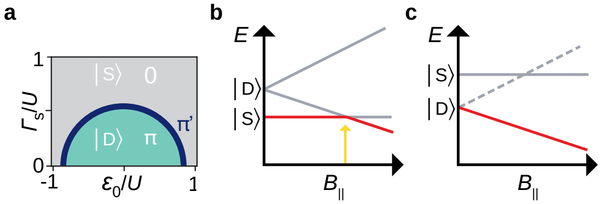

Figure 8.5: 0-π phase transitions: **a**, Qualitative phase diagram showing the singlet ($|S\rangle$) and doublet ($|D\rangle$) ground states as a function of coupling to the superconducting leads Γ_S and level detuning of the QD ε_0, where U is the charging energy. A more complete phase diagram of the S-QD-S system is shown in Ref. [145]. **b,c**, Magnetic field dependence of a singlet $|S\rangle$ (**b**) and doublet $|D\rangle$ (**c**) ground state. The yellow arrow marks the position where the $|D\rangle$ excited state is degenerate with the $|S\rangle$ ground state.

9

SIGNATURES OF ZERO ENERGY MODE HYBRIDIZATION

This chapter shows the preliminary results of a high magnetic field compatible loop qubit device. The results shown here build upon the previous two chapters. A quantum dot (QD) is used as a spectrometer of the top and bottom superconducting one-dimensional wires to identify zero-bias states. When zero-bias states were identified in both wires, controlling the charge occupancy of the QD, showed signatures of avoided crossings when on resonance with the QD. These avoided crossings oscillate periodically by controlling the phase difference between the two superconducting wires. The observations are compatible with the theoretical picture of hybridizing zero-energy modes presented in Chapter 7.

9.1 INTRODUCTION

Chapter 8 illustrated the ability to form and control the coupling between a quantum dot (QD) and two superconducting nanowires (S). Another important result was the ability to perform tunneling spectroscopy of a S-QD-S junction, which will be necessary for identifying putative zero-bias states. However, the device had several limitations. First, the superconducting gap of the junction closed at $B_{\parallel} \sim 1$ T, hindering the exploration of MZMs in the superconducting nanowire leads. Secondly, due to the strong QD-S coupling, it was not possible to resolve sub-gap states in the nanowires. These challenges were overcome by a slight redesign of the gate geometry used to define the QD.

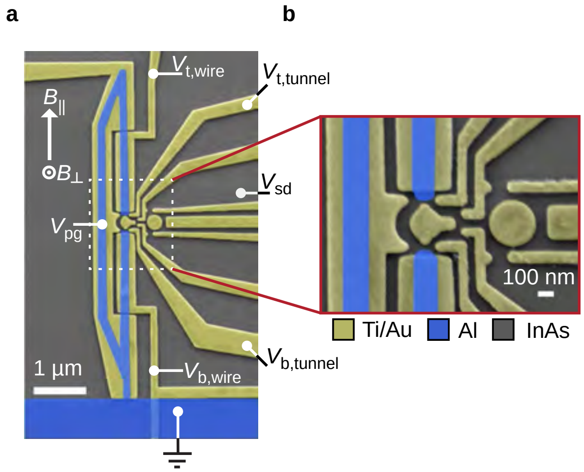

Figure 9.1: **Loop qubit device:** False-colour electron micrograph of the superconductor-quantum dot-superconductor Josephson junction where a QD is embedded between the two wires (top and bottom), which form a superconducting Al loop (blue). The chemical potential of the top (bottom) wire is controlled by a Ti/Au gate (yellow) with voltage $V_{\mathrm{t,wire}}$ ($V_{\mathrm{b,wire}}$) and the tunnel barrier is controlled by voltage $V_{\mathrm{t,tunnel}}$ ($V_{\mathrm{b,tunnel}}$). A bias voltage V_{sd} is applied to the normal lead and the superconducting loop is grounded. Magnetic field directions are shown where $B_{\perp}$ is used to thread fluxes in the superconducting loop.

The device studied in this chapter is shown in Fig. 9.1. It was fabricated on an InAs two-dimensional electron gas (2DEG) covered by 7 nm of epitaxially grown Al, similar to the device in Chapter 8. The most prominent change was two additional electrodes operated with gate voltages $V_{\mathrm{t,tunnel}}$ and $V_{\mathrm{b,tunnel}}$. The addition of these gates allowed for stronger confinement of the QD and a reduced coupling to the superconducting leads. For the detection of MZMs in one-dimensional nanowires, it was necessary to tune the chemical potential of each nanowire [80]. This was achieved by controlling gate voltages $V_{\mathrm{t,wire}}$ and $V_{\mathrm{b,wire}}$ for each wire independently. Tunneling spectroscopy was performed by measuring the differential conductance G from the normal lead (right side of Fig. 9.1a) through a tunneling construction into the S-QD-S junction as a function of V_{sd} with the superconducting loop grounded.

9.2 Tunneling spectroscopy

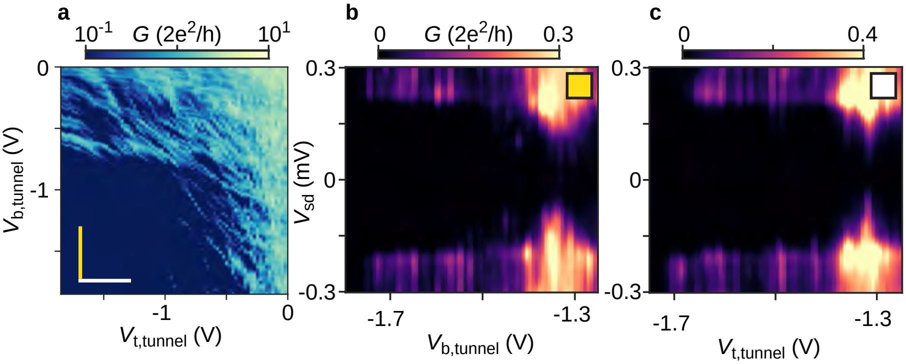

Figure 9.2: **Independent spectroscopy of each nanowure:** **a**, Differential conductance G as a function of gate voltages $V_{\mathrm{t,tunnel}}$ and $V_{\mathrm{b,tunnel}}$. **b**, G as a function $V_{\mathrm{b,tunnel}}$ and voltage bias V_{sd} revealing the superconducting gap of the bottom wire. **c**, G as a function $V_{\mathrm{t,tunnel}}$ and voltage bias V_{sd} showing the superconducting gap of the top wire.

The additional gate electrodes increased the control over the device, offering the flexibility to independently control the tunneling barriers for each nanowire segment. This is illustrated in Fig. 9.2, where the gate voltages $V_{\mathrm{t/b,tunnels}}$ are used to open and close each wire. In Fig. 9.2a, the zero-bias conductance G is measured as a function of $V_{\mathrm{t,tunnel}}$ and $V_{\mathrm{b,tunnel}}$. Importantly, it is observed that the conductance can only be pinched off with a combination of both $V_{\mathrm{t,tunnel}}$ and $V_{\mathrm{b,tunnel}}$. To show independent spectroscopy of each wire, first both wires are pinched off with $V_{\mathrm{t/b,tunnels}} \sim -1.75$ V. Then, by only reopening with one tunnel barrier at a time allows for independent interrogation of each wire. In Fig. 9.2b the differential conductance

G is measured as a function of $V_{\mathrm{b,tunnel}}$ and V_{sd} starting from -1.75 V where both wires are pinched off. Increasing only $V_{\mathrm{b,tunnel}}$ reveals a superconducting gap of $\Delta = 220$ μeV, which is interpreted to reflect tunneling spectroscopy of the bottom wire. A similar measurement for the top wire is shown in Fig. 9.2c. These results indicate that independent spectroscopy can be performed on either wire.

A requirement for Majorana parity readout is to have a well-defined QD between the two superconducting nanowires to allow for controllable hybridization of MZMs [32]. Using the results from chapter 8, the S-N-S junction was confined into a QD using the surrounding gate electrodes. Figure 9.3a shows the differential conductance G as a function of gate voltage V_{pg} used to tune to occupancy of the QD and the voltage bias V_{sd}, showing a series of Coulomb diamonds with a regular periodicity. The QD is used to perform spectroscopy of the nanowire segments using co-tunneling transport [80]. That is, by using the Coulomb valley as a tunnel barrier to perform spectroscopy. Figure 9.3b shows G at $B_{||} = 2.9$ T as a function of V_{pg} and V_{sd} where discrete states are observed extending through the Coulomb valleys, which are interpreted to be sub-gap states of the nanowires.

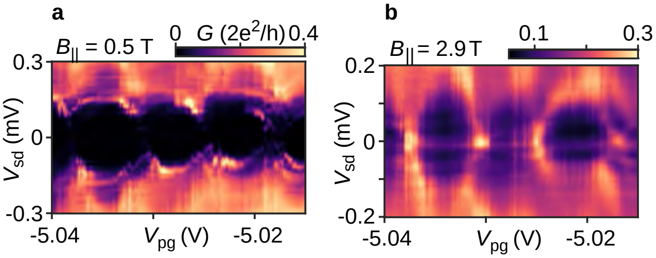

Figure 9.3: **Coulomb blockade:** Differential conductance G as a function of gate voltage V_{pg} and voltage bias V_{sd} for $B_{||} = 0.5$ T (**a**) and $B_{||} = 2.9$ T (**b**).

We proceed to study each wire independently in an N-QD-S configuration by closing one nanowire and performing tunneling spectroscopy on the other. Figure 9.4a shows G as a function of $V_{\mathrm{t,wire}}$ and $V_{\mathrm{t,tunnel}}$ revealing Coulomb blockade peaks (bottom wire closed). In order to efficiently explore the gate-voltage parameter space, the third harmonic technique discussed in chapter 4.2.3 is employed. In summary, a measurement of the third harmonic of the current $I_{3\omega} \propto -\frac{\partial^2 G}{\partial V^2}$ at $V_{\mathrm{sd}} = 0$. Therefore, a positive third harmonic current $I_{3\omega}$ indicates a zero-bias peak (ZBP).

To determine if the ZBP is stable in both gate voltage and magnetic field (as expected for MZMs), $I_{3\omega}$ is measured as a function of $V_{\mathrm{t,wire}}$ and $V_{\mathrm{t,tunnel}}$ for magnetic fields ranging from $B_{||} = 2$ to 3 T in 100 mT steps. Then a numerical average is calculated $\langle I_{3\omega} \rangle$ of all eleven $V_{\mathrm{t,wire}}$ and $V_{\mathrm{t,tunnel}}$ maps. Figure 9.4b shows $\langle I_{3\omega} \rangle$, where positive regions (red) are indications of stable ZBPs.

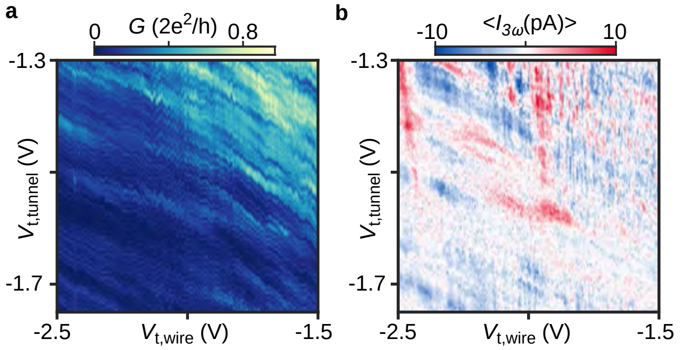

Figure 9.4: Third harmonic: **a**, Differential conductance G as a function of gate voltages $V_{\mathrm{t,wire}}$ and $V_{\mathrm{t,tunnel}}$. **b**, Numerically averaged third harmonic current $\langle I_{3\omega} \rangle$. See text for description.

Based on the third harmonic measurements, $V_{\mathrm{t,wire}}$ and $V_{\mathrm{t,tunnel}}$ are set to regions of stable ZBPs. Measuring the differential conductance G as a function of $V_{\mathrm{t,wire}}$ and V_{sd} in Fig. 9.5a reveals a ZBP extending through multiple Coulomb valleys at $B_{||} \sim 3$ T. Due to the Coulomb peaks having a field behaviour, it is necessary to measure Coulomb diamonds from $B_{||} = (0$ to $3)$ T to reconstruct the field dependence in the Coulomb valley. In Fig. 9.5a the reconstruction shows the emergence of a ZBP after the closure of a gap at $B_{||} \sim 2$ T. To perform a similar investigation of the bottom wire, the top wire is closed with $V_{\mathrm{t,tunnel}}$. To identify stable ZBPs in $V_{\mathrm{b,wire}}$ and $V_{\mathrm{b,tunnel}}$ a similar procedure outlined above is used for the top wire. Figure 9.5c reveals a ZBP at $V_{\mathrm{b,wire}} \sim -1.99$ V. The reconstructed parallel magnetic field dependence is shown in Fig. 9.5d, showing a ZBP emerging at $B_{||} = 2.5$ T and persisting until the closure of the gap at ~ 3 T. The observation of a stable zero-energy state above a critical parallel magnetic field is consistent with a topological phase transition and the appearance of MZMs in both the top and bottom nanowires.

The observation of zero-bias states in each wire enables the investigation of MZM hy-

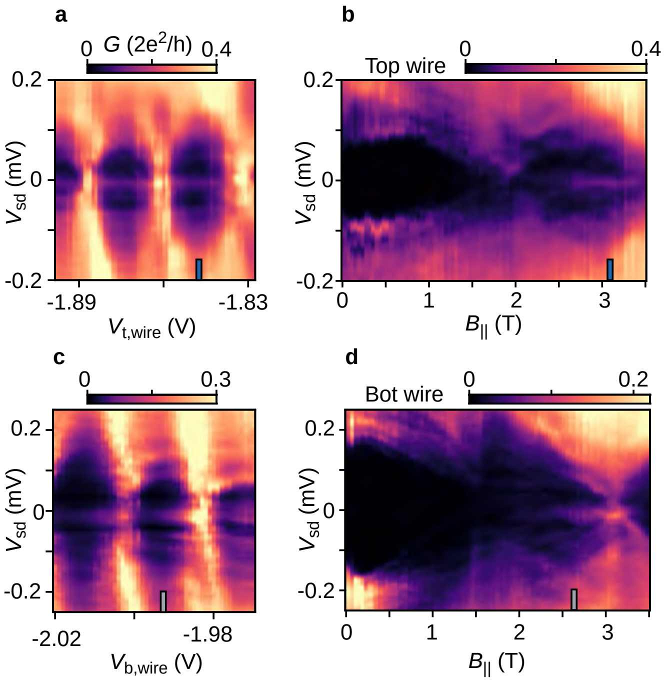

Figure 9.5: **Zero-bias peaks:** **a**, Differential conductance G as a function of gate voltage $V_{\text{t,wire}}$ and voltage bias V_{sd} for a parallel magnetic field $B_{||} = 3.1$ T. **b**, G as a function of $B_{||}$ and V_{sd} reconstructed from the Coulomb valley marked in **a**. **c**, G as a function of gate voltage $V_{\text{b,wire}}$ and V_{sd} for $B_{||} = 2.6$ T. **b**, G as a function of $B_{||}$ and V_{sd} reconstructed from the Coulomb valley marked in **c**.

bridization. To investigate the hybridization of the zero-bias states, the tunnel barriers to each wire are opened by setting $V_{\text{t,tunnel}} = V_{\text{b,tunnel}} \sim -1.25$ V. In Fig. 9.6b, G is shown as a function of $V_{\text{t,wire}}$ (used to tune the occupancy of the QD) and V_{sd}, where distinctly different behaviours on Coulomb peaks and in Coulomb valleys are observed. Deep in the valleys a few near ZBPs (see blue tick marker) are found. Figure 9.6a shows the reconstructed parallel magnetic field dependence in the Coulomb valley. At $B_{||} \sim 2$ T, a partial closure of the superconducting gap is observed, which coincides with the appearance of a ZBP for increasing $B_{||}$. It appears that increasing $B_{||}$ causes an additional state to move near zero-bias, however the reduced conductance in the Coulomb valley hinders the visibility of the states. The two near ZBPs can be seen more clearly at the blue marker in Fig. 9.6e.

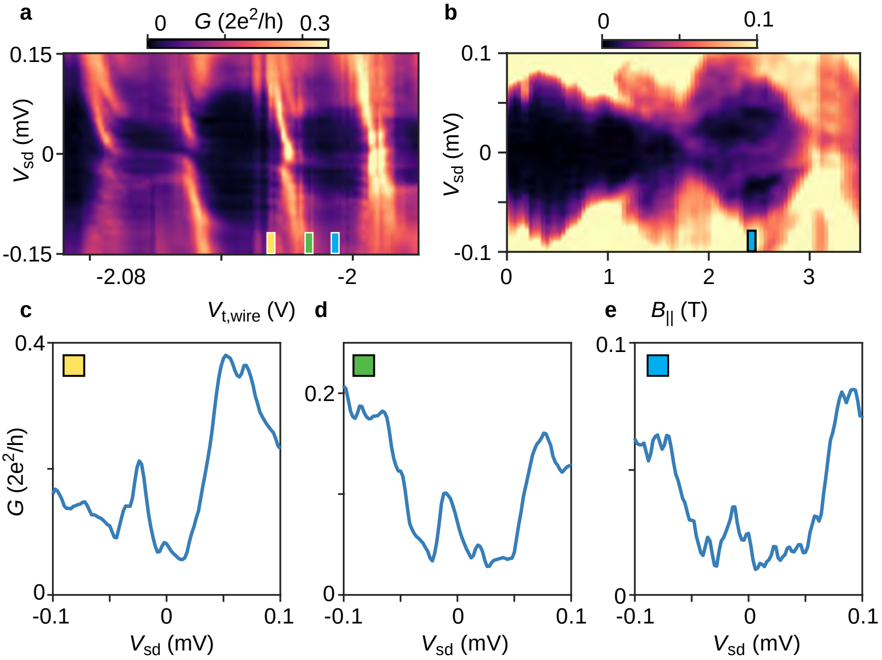

Figure 9.6: **Two-wire spectroscopy: a**, Differential G as a function of $B_{||}$ and V_{sd} reconstructed from the Coulomb valley marked in **b**. **b**, Differential conductance G as a function of gate voltage $V_{\mathrm{t,wire}}$ and voltage bias V_{sd} for a parallel magnetic field $B_{||} = 2.7$ T.

Next the attention is drawn to the behaviour of these two near zero-bias states when the QD is brought into resonance (see Fig. 9.6b). Focusing on the Coulomb peak to the left of the blue marker ($V_{\mathrm{t,wire}} = -2.02$ V), it is observed that the two near zero-bias states on the positive side of the Coulomb peak diverge towards positive V_{sd}, while approaching the Coulomb peak from the opposite side causes a divergence to negative V_{sd}. This behaviour leads to the formation of an avoided crossing when on resonance with the QD. This behaviour is also observed for other Coulomb peaks in Fig. 9.6b.

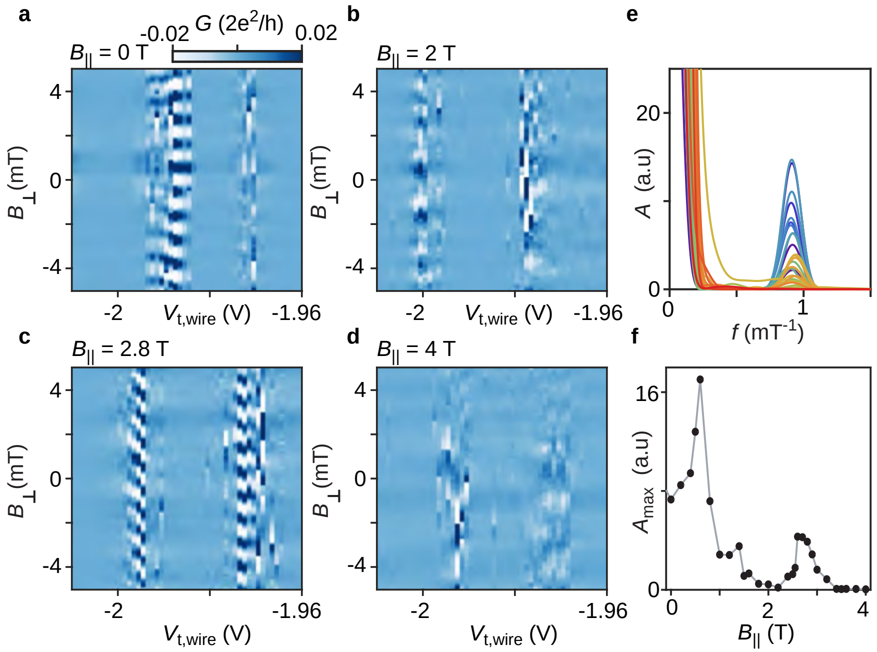

Figure 9.7: **Periodic conductance oscillations**. **a-d**, Differential conductance ΔG as a function of gate voltage $V_{\mathrm{t,wire}}$ and perpendicular magnetic field $B_\perp$ controlling the flux in the superconducting loop for parallel magnetic fields $B_{||} = 0$ T, $B_{||} = 2$ T, $B_{||} = 2.8$ T, $B_{||} = 4$ T. Power spectrum (**e**) and maximum oscillation amplitude (**f**) as a function of $B_{||}$. The oscillation amplitude is measured from the power spectra from a series of measurements similar to **a-d** at each $B_{||}$. G is the conductance with a subtracted slowly varying background. The Coulomb peaks studied here correspond to the two rightmost peaks in Fig. 9.6b and are shifted due to gate hysteresis.

9.3 Periodic conductance oscillations

In chapter 7 it was observed that the hybridization of MZMs should depend on the phase difference across the S-QD-S junction. To investigate this effect on the avoided crossing, a perpendicular magnetic field is applied to tune the superconducting phase difference ϕ between the two wires. In Fig. 9.7a-d, the differential conductance G (slowly varying background removed), is shown as a function of $V_{\mathrm{t,wire}}$ and a perpendicular magnetic field, $B_\perp$, used to thread fluxes through the superconducting loop and tune the superconducting phase difference. At $B_{||} = 0$ T, strong conductance oscillations are observed when on resonance with the QD with a periodicity $\Delta B_{\perp} = 1$ mT, corresponding to a flux $h/2e$ threading the superconducting loop (see Fig. 9.7a). As the magnetic field is increased, the conductance oscillations gradually decrease in amplitude, coming to a minimum at 2 T. After $B_{||} = 2$ T, the conductance oscillations revive, reaching a local maximum at $B_{||} = 2.8$ T (see Fig. 9.7c) before decaying in the normal state. Figure 9.7,e,f show the power spectrum and maximum oscillation amplitude for each magnetic field displaying the gradual decrease and the revival of the oscillation amplitude with parallel magnetic field. The suppression of the conductance oscillations coincides with the magnetic field where the partial gap closure was observed in Fig. 9.6a, and the revival corresponds to the field where the zero-bias states emerged. The conductance oscillations were observed when the QD was brought into resonance and absent in the Coulomb valley. The reentrance of phase coherent transport at $B_{||} \sim 2.5$ T indicates an additional coherent transport mechanism was turned on with the appearance of zero-bias states.

9.4 Discussion and conclusion

The observed behaviour of the ZBP avoided crossing in the vicinity of a Coulomb peak is comparable with the theoretical picture of MZM hybridization outlined in Chapter 7. This can be understood by considering two different scenarios. I first consider the case of a system consisting of a single topological nanowire with a QD coupled at one end. The isolated MZM-QD interaction in this setup has been proposed as a method to assess the quality of the MZM non-locality [155, 156]. When the MZM wavefunctions of a single wire are not overlapping, the MZMs are considered non-local. In this case, the isolated MZM-QD interaction does not lead to an energy splitting. Instead, if there is a wavefunction overlap, this cause a finite energy splitting of the zero-energy state when on resonance with the QD. This system has recently been studied experimentally in Ref [114].

In the loop qubit geometry investigated here, the purpose of the QD is to mediate the hybridization of γ_2 and γ_3 as shown in Chapter 7.1. In this case, γ_2 and γ_3 constitute a single-fermionic mode that has a parity dependent interaction with the QD [157]. When the QD is on resonance, the two MZMs can hybridize, which leads to an energy splitting due to the wavefunction overlap as discussed in Chapter 2.4 (also see Fig. 7.2).

This theoretical picture is compatible with the observations of Fig. 9.6b. When the QD is brought into resonance, it causes an avoided crossing between the ZBPs, while when off resonance the energy of the states goes back to near zero-bias *. Additionally, this avoided crossing was observed to oscillate as a function of phase difference across the junction as expected for the case of MZM hybridization. However, this behaviour could also arise due to the interaction of the QD with a trivial localized Andreev bound state located in the vicinity of the QD. Therefore stronger evidence is needed before drawing conclusions about the hybridization of MZM. For example, an important missing observation is the oscillations of the avoided crossing in bias voltage V_{sd}, in addition to the conductance oscillations observed in Fig. 9.7. An additional prediction of Chapter 7.1 is that in the absence of poisoning the periodicity of each Majorana parity branch should be 4π in ϕ. For the results shown above, the 4π periodicity is inaccessible in the current measurement scheme because electron transport is a source of poisoning for the MZMs. Therefore, in transport both parity branches are recovered and the periodicity is 2π periodicity or $h/2e$ in flux threading the loop. To gain access to 4π periodicity measurements, the QD must be isolated from the normal lead.

In summary, a promising platform and device geometry has been introduced for investigating the hybridization of zero energy states by tunneling spectroscopy. Future experiments will focus on charge detection of the QD to investigate joint parity measurements of MZMs with the additional charge sensor seen on the right-hand side of Fig. 9.1.

---

*The splitting in the Coulomb valley can be explained by a residual hybridization of the MZMs due to not achieving a fully detuned QD before the next Coulomb peak [157]

V

Topological Josephson junctions

10

EVIDENCE OF TOPOLOGICAL SUPERCONDUCTIVITY IN PLANAR JOSEPHSON JUNCTIONS

A. Fornieri*, A.M. Whiticar*, F. Setiawan, E. Marin, A. Drachmann, A. Keselman, S. Gronin, C. Thomas, T. Wang, R. Kallaher, G. Gardner, E. Berg, M. Manfra, A. Stern, C.M. Marcus, F. Nichele

This manuscript has been published as: Nature vol. 569, pg. 89 - 92 (2019)

A drawback of the one-dimensional nanowires platform introduced in chapter 2.4 and discussed in Chapters 5 through 9 is the dependence of the topological phase transition on chemical potential [87, 158]. In 2017, two theoretical proposal offered an alternative purely two-dimensional system predicted to be less sensitive to the microscopic details of the system [35, 36]. The proposed device geometry is based on planar Josephson junctions, where Al leads confine a quasi one-dimensional channel. This system adds an additional control parameter - the phase difference across the junction - enabling additional control over the topological phase. This system differs from nanowire junctions that are expected to show the 4π Josephson effect as discussed in Chapters 7. Instead, it is predicted that MZMs are created at the ends of an elongated Josephson junction. Experimental evidence supporting the existence of a topological phase in a planar Josephson junction will be shown.

---

*Equal Contribution

10.1 INTRODUCTION

Majorana zero modes are quasiparticle states localized at the boundaries of topological superconductors that are expected to be ideal building blocks for fault-tolerant quantum computing [9, 159]. Several observations of zero-bias conductance peaks measured in tunneling spectroscopy above a critical magnetic field have been reported as experimental indications of Majorana zero modes in superconductor/semiconductor nanowires [79, 80, 82, 101, 106]. On the other hand, two dimensional systems offer the alternative approach to confine Majorana channels within planar Josephson junctions, in which the phase difference ϕ between the superconducting leads represents an additional tuning knob predicted to drive the system into the topological phase at lower magnetic fields [35, 36]. Here, we report the observation of phase-dependent zero-bias conductance peaks measured by tunneling spectroscopy at the end of Josephson junctions realized on a InAs/Al heterostructure. Biasing the junction to $\phi \sim \pi$ significantly reduces the critical field at which the zero-bias peak appears, with respect to $\phi = 0$. The phase and magnetic field dependence of the zero-energy states is consistent with a model of Majorana zero modes in finite-size Josephson junctions. Besides providing experimental evidence of phase-tuned topological superconductivity, our devices are compatible with superconducting quantum electrodynamics architectures [98] and scalable to complex geometries needed for topological quantum computing [35, 37, 160].

The Josephson junctions (JJs) studied in this work were fabricated from a planar heterostructure comprising of a thin Al layer epitaxially covering a high mobility InAs two- dimensional electron gas (2DEG) [17]. As a consequence of the highly transparent superconductor/ semiconductor interface [90], a hard superconducting gap is induced in the InAs layer [61, 94]. Selectively removing an Al stripe of width W_1 and length L_1 defines a normal InAs region, laterally contacted by superconducting leads, as shown in Fig 10.1a. Superconducting gaps $\Delta\exp(\pm i\phi/2)$ opening below the Al planes on the right- and left-hand side [53, 59], respectively, confine low energy quasiparticles within the normal InAs channel. Owing to the strong spin-orbit interaction in InAs [17], together with the lateral confinement, the JJ of Fig 10.1a is predicted to undergo a topological transition at high magnetic field $B_{||}$ parallel to the junction [35], with Majorana modes isolated from the continuum forming at the end points (crosses in Fig 10.1a), similarly to conventional nanowires [15, 16]. Most strikingly, phase control offers an additional tuning parameter to enter the topological regime not explored so far. Biasing the JJ to $\phi = \pi$ was predicted to significantly reduce the critical magnetic field of the topological transition, and to enlarge its phase boundaries in chemical potential [36].

Here we investigate planar JJs as schematically shown in Fig 10.1a as a function of $B_{||}$, chemical potential μ and phase difference ϕ. Phase biasing is obtained by embedding the JJ in a direct-current superconducting quantum interference device (DC SQUID) threaded by a magnetic flux [52]. A robust zero-bias peak (ZBP) exhibiting strong dependence on ϕ is measured via tunneling spectroscopy using a laterally coupled quantum point contact (QPC), as schematically shown in Fig 10.1a. The ZBP behavior is consistent with a Majorana mode in a finite-size topological JJ (see Supplementary Fig. 10.8).

10.2 DEVICE

Figure 10.1b shows a schematic of our device, which consists of a three-terminal asymmetric SQUID with two JJs, labeled 1 and 2, and a tunneling probe coupling to a normal lead on the top end of JJ1. Figure 10.1c shows an electron micrograph in the surrounding of JJ1. The junctions are characterized by Josephson critical currents $I_{c,2} > I_{c,1}$, such that the phase difference ϕ across JJ1 can be tuned from 0 to $\sim \pi$ by threading the SQUID loop with a magnetic flux Φ (generated by the out-of-plane field $B_\perp$) varying from 0 to $\Phi_0/2$, where $\Phi_0 = h/2e$ is the superconducting flux quantum (e is the electron charge and h the Planck constant). For details on the phase biasing in a SQUID see Chapter 2.3.7. The SQUID is laterally connected to two superconducting leads that serve as ground and allows the Josephson critical current of the interferometer to be measured (see Supplementary Fig. 10.9). The SQUID loop is obtained by a combination of deep wet etching on the semiconductor heterostructure and selective wet etching of the top Al layer. A HfO_2 dielectric layer is deposited over the entire sample for gate isolation, followed by lift-off of the Ti/Au gate structures. Top gates V_1 and V_2 control the chemical potential in JJ1 and JJ2, respectively. Split gates deposited at the top end of JJ1 form a QPC. In the tunneling regime, the QPC serves as spectroscopic probe revealing the local density of states of JJ1. The uppermost gate extends between the QPC gates and helps defining a sharp tunnel barrier when operated at a voltage $V_{\text{top}} \sim 0$ (see Chapter 4.3 for more details). To ensure a hard superconducting gap in high parallel fields, the QPC gates additionally confine the 2DEG beneath the narrow Al leads [101, 106] (see Fig 10.1c). We present data for a device with $W_1 = 80$, $W_2 = 40$ nm, $L_1 = 1.6$ µm and $L_2 = 5$ µm. The width of the superconducting leads is $W_{S1} = W_{S2} = 160$ nm for both JJs, and SQUID loop area ~ 8 µm^2. Data was reproduced for two additional devices with $W_1 = 80$ and 120 nm respectively. Differential conductance G was measured in a four-terminal configuration by standard AC lock-in techniques in a dilution refrigerator with an electron base temperature of about 40 mK.

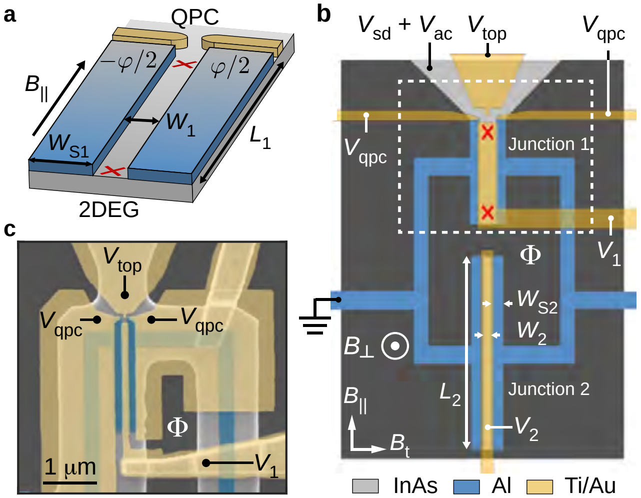

Figure 10.1: Topological Josephson junction. **a**, Schematic of a planar JJ formed by two epitaxial superconducting layers (represented in blue) covering a 2DEG with strong spin-orbit interaction (grey). A one-dimensional channel, defined between the superconducting leads, can be tuned into the topological regime with Majorana modes (red crosses) at its ends by the parallel field $B_{||}$, the 2DEG chemical potential μ and the phase difference between the superconductors ϕ. Majorana modes can be probed in tunneling spectroscopy using a QPC located at one end of the JJ. **b**, Schematic of the measured device (not to scale) consisting of a superconducting loop interrupted by two JJs (labeled 1 and 2) in parallel. The interferometer is formed by InAs 2DEG (light grey) and epitaxial Al (blue). Five Ti/Au gates (yellow) allow independent tuning of the chemical potential in JJ1 (gate voltage V_1), the chemical potential in JJ2 (V_2) and the transmission of a tunnel barrier at the top end of JJ1 (V_{qpc} and V_{top}). The applied AC and DC bias voltages are also indicated, together with the direction of magnetic field parallel ($B_{||}$) and transverse (B_{t}) to the JJ, and the magnetic flux Φ. **c**, False color scanning electron micrograph of the top part of a typical device, as in the dashed box shown in panel **b**. The colors are the same as those used in panel **b**.

10.3 Tunneling spectroscopy

Figure 10.2a shows G as a function of the bias voltage V_{sd} and Φ at $B_{||} = 0$. The induced superconducting gap $\Delta(\Phi = 0) \simeq 150$ μeV periodically oscillates as a function of Φ and is reduced by approximately 50 % at $\Phi = (2n + 1)\Phi_0/2$, where n is an integer. This behavior indicates phase-coherent transport through JJ1 generated by Andreev reflection processes [60, 161] at the interfaces between the bare 2DEG and the proximitized leads. The flux modulation of the whole continuum of states outside the gap is expected for JJs with narrow superconducting leads ($W_{\mathrm{S1}} \ll \xi_{\mathrm{S}}$, where $\xi_{\mathrm{S}} = \hbar v_{\mathrm{F}}/\pi\Delta \sim 1.5$ μm is the superconducting coherence length and v_{F} is the Fermi velocity in the semiconductor), while the non-complete closure of the gap at $\Phi = (2n + 1)\Phi_0/2$ is associated to the finite length L_1 of the junction and to possible unintended asymmetries in the etched superconducting leads (see Supplementary Fig. 10.8 for further details). The finite sub-gap conductance at $B_{||} = 0$ (see Fig. 10.2f) is due to a relatively high tunneling transmission and can be suppressed by tuning V_{qpc} more negative, as shown in Supplementary Figs. 10.10.

As $B_{||}$ is increased, discrete Andreev bound states (ABSs) enter the gap and move towards zero energy, as shown in Fig. 10.2b for $B_{||} = 250$ mT. We note that these states have an asymmetric flux dependence. We attribute this behavior to the presence of a strong spin-orbit interaction and a finite Zeeman field, similarly to what has been predicted and observed for quasi-one-dimensional systems [162, 163].

At higher values of $B_{||}$ a ZBP in conductance appears at $\Phi = (2n + 1)\Phi_0/2$ (corresponding to $\phi \sim \pi$), while it vanishes when Φ is set to $2n\Phi_0$, i.e. when $\phi = 0$, as shown in Fig. 10.2c for $B_{||} = 525$ mT. The phase dependence of the ZBP is highlighted in Fig. 10.2g, which displays the conductance line-cuts for $\phi = 0,\ \pi$.

At even higher fields, from 600 mT to 1 T the ZBP extends over the whole ϕ range, except at $\phi \sim \pi$ where a relative minimum is observed (Figs. 10.2d,e,h). In this range of $B_{||}$ the state sticks at zero energy for $\phi = 0$, as shown in Fig. 10.2h, while it oscillates and moves to higher energies for $\phi = \pi$ (see Supplementary Fig. 10.10f). Above $B_{||} = 1$ T the induced gap softens and the phase dependence of sub-gap states gradually disappears as the JJs of the SQUID reach the resistive state.

The observed behavior of the ZBP in field and phase is in good qualitative agreement with the calculated spectrum of a finite-size topological JJ, as shown in Supplementary Fig. 10.8. As the Zeeman field is increased, two discrete sub-gap states are expected to merge at zero energy for $\phi = \pi$ and gradually extend in phase until reaching $\phi = 0$. The calculated gapped zero-

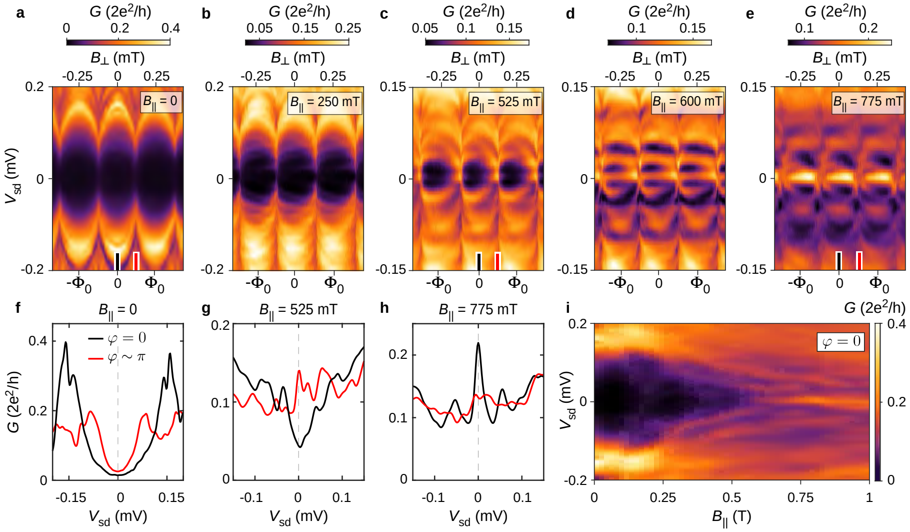

Figure 10.2: Evolution of the zero-bias peak in parallel field. **a-e**, Differential conductance G as a function of magnetic flux, Φ, piercing the SQUID loop and source-drain bias, V_{sd}, measured at different values of magnetic field, $B_{||}$, parallel to the junction. The flux is generated by the out-of-plane field $B_{\perp}$. The values of $B_{\perp}$ have been shifted to remove offsets. **f-h**, Line-cuts of G versus V_{sd} at different values of $B_{||}$ for phase bias $\phi = 0$ (black lines) and $\phi \sim \pi$ (red lines), as indicated by the ticks in panels **a**, **c** and **e**. **i**, G as a function of V_{sd} and $B_{||}$ at $\phi = 0$. The plot was reconstructed from line-cuts as the ones shown in panels **f-g**. The measurements were taken at the top gate voltage $V_1 = V_1^{\star} = -118.5$ mV.

energy state around $\phi = 0$ is characterized by a Majorana wave function localized at the edges of the JJ (see Supplementary Fig. 10.8h). The oscillations in energy of the observed state at $\phi \sim \pi$ are reproduced by the simulations and can be understood in terms of hybridization of the Majorana modes (Supplementary Fig. 10.8i), since at this value of ϕ the induced gap is minimized and, as a result, the coherence length is maximized.

10.4 ZERO-BIAS PEAK STABILITY

One of the most interesting features predicted for a perfectly transparent JJ is the significant expansion of the topological phase in magnetic field and chemical potential at $\phi = \pi$ [36]. We therefore investigated the stability of the ZBP, starting from its dependence on the gate voltage V_1, which controls the chemical potential in JJ1. In order to explore efficiently our 4-dimensional parameter space, we recorded the third harmonic $I_{3\omega}(V_{\mathrm{sd}})$ of the current measured by the lock-in amplifier, where $I_{3\omega}(V_{\mathrm{sd}}) \propto -G''(V_{\mathrm{sd}}) = -(\partial^2 G/\partial V^2)|_{V_{\mathrm{sd}}}$ (see Chapter 4.2.3). A ZBP in conductance is therefore identified by a positive value of $I_{3\omega}(V_{\mathrm{sd}} = 0)$, i.e., by a negative value of $G''(V_{\mathrm{sd}} = 0)$, which indicates a negative curvature around $V_{\mathrm{sd}} = 0$.

Figure 10.3 displays $I_{3\omega}(V_{\mathrm{sd}} = 0)$ as a function of Φ and V_1 for different values of $B_{||}$. At $B_{||} = 500$ mT horizontal stripes showing positive values of $I_{3\omega}(V_{\mathrm{sd}} = 0)$ are visible at $\phi \simeq (2n+1)\pi$. Increasing the field causes the region of negative curvature to expand around the voltage $V_1^\star = -118.5$ mV by ~ 2 mV and in phase extending to $2n\pi$. For $B_{||} = 650$ mT the ZBP region expands further around $V_1^\star$, while a maximum develops at $\phi \simeq (2n + 1)\pi$, indicating that the ZBP has split to finite energy. The ZBP region covers a maximum range of 10 mV at 775 mT and remains extended in phase for $\phi \neq (2n + 1)\pi$.

The finite range of V_1 over which the ZBP is stable is explained by the narrow width $W_{\mathrm{S1}} \ll \xi_{\mathrm{S}}$ of the superconducting leads, which effectively decrease the ratio between Andreev and normal reflection probabilities, thus reducing the size of the topological phase as a function of μ (see Fig. 10.8a). Although this geometry causes a deviation from the predicted behavior of a topological JJ, in our devices the finite width is necessary to guarantee a well-defined induced gap up to 1 T (to be discussed in the Outlook section below).

The complementary study of the ZBP stability in Φ and $B_{||}$ for different values of V_1 is shown in Fig. 10.4. At $V_1 = -116$ mV (Fig. 10.4a) extended regions of positive $I_{3\omega}(V_{\mathrm{sd}} = 0)$ indicating a stable ZBP appear above an oscillating critical field $B_{\mathrm{c}}(\phi)$, which reaches a minimum value $B_{\mathrm{c}}([2n+1]\pi) = 570$ mT, as indicated by the blue arrow. On the other hand,

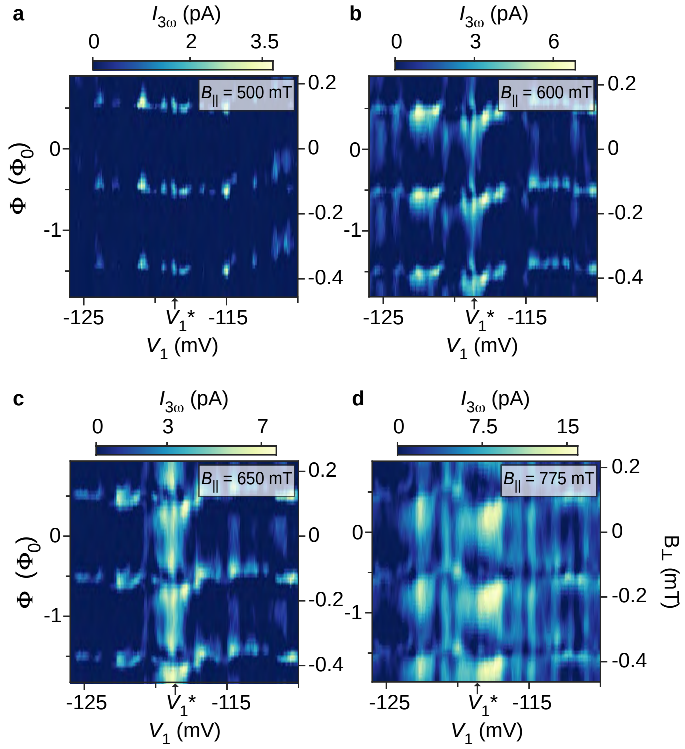

Figure 10.3: Stability of the zero-bias peak. a-d, Third harmonic of the current $I_{3\omega}(V_{\mathrm{sd}} = 0)$ measured by the lock-in amplifier at zero bias as a function of top gate voltage, V_1, and magnetic flux, Φ, for different values of magnetic field, $B_{||}$, parallel to the junction. The flux is generated by the out-of-plane field $B_\perp$. The values of $B_\perp$ have been shifted to remove offsets.

the vertical stripe visible at $\sim$ 0.4 T is due to ABSs crossing zero energy without sticking. Similarly to what was observed above as a function of the chemical potential, the negative curvature region significantly expands in terms of $B_{||}$ range for $V_1 = V_1^\star$, where $B_c([2n+1]\pi) = 435$ mT (Fig. 10.4b). At more negative V_1 the ZBP regime contracts again ($B_c([2n+1]\pi) = 480$ mT, Fig 10.4c), consistent with the stability maps shown in Fig. 10.3.

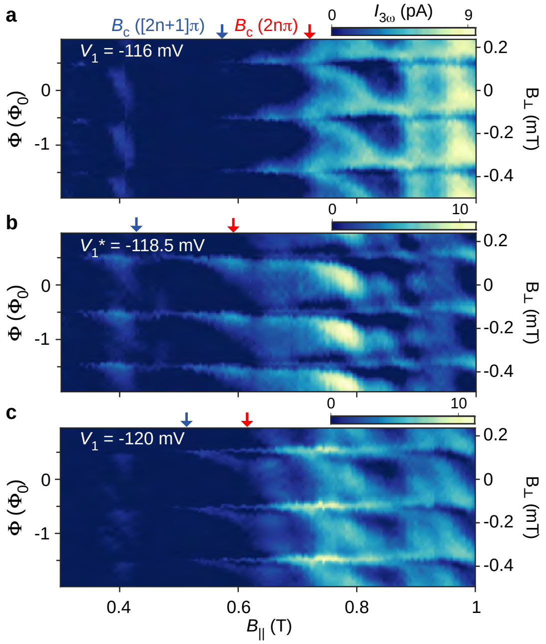

Figure 10.4: Phase dependence of the critical field. a-c, Third harmonic of the current $I_{3\omega}(V_{sd} = 0)$ measured by the lock-in amplifier at zero bias as a function of magnetic field, $B_{||}$, applied parallel to the junction and magnetic flux, Φ, for different values of top gate voltage V_1. The flux is generated by the out-of-plane field $B_\perp$. The values of $B_\perp$ have been shifted to remove offsets. A positive value of $I_{3\omega}(V_{sd} = 0)$ corresponds to a ZBP in conductance as a function of V_{sd}.

10.5 Discussion

The combined results shown in Figs. 10.3 and 10.4 indicate the expansion of the ZBP region from $\phi \sim \pi$ to the full phase range as $B_{||}$ is increased. This behavior is in qualitative agreement with the topological phase diagrams calculated for our system (see Supplementary Figs. 10.8a,b). We note that for specific values of chemical potential, the model of a perfectly symmetric and clean JJ predicts a topological phase transition close to zero field [36], while experimentally a ZBP is observed only above 400 mT, as discussed above. This discrepancy could be ascribed to non-idealities of JJ1, such as disorder [99, 164] and unintended asymmetries in the superconducting leads. A broken left-right symmetry in JJ1 could also explain the observed asymmetry in the phase dependence of the ZBP region at different values of V_1 (Fig. 10.4). Although we do not observe a reduction of the critical field down to zero, our design decreases B_c by about a factor of four compared to previous experiments on one-dimensional Majorana wires defined below Al stripes in similar heterostructures [101, 106]. This is due to the increased g-factor of the bare InAs Majorana channel and to the phase dependence of the observed ZBP. As expected, the amplitude of the B_c modulations depends on the value of V_1 and a maximum visibility $(B_c(2n\pi)-B_c([2n+1]\pi)/B_c([2n+1]\pi) \sim 37\%$ is obtained for $V_1 = V_1^\star$. Lastly, we note that the ZBP is robust over a range of $\sim$ 70 mV in V_{qpc} and in V_{top}, which modify the above-gap conductance by approximately one order of magnitude, as shown in Supplementary Fig. 10.10c,d.

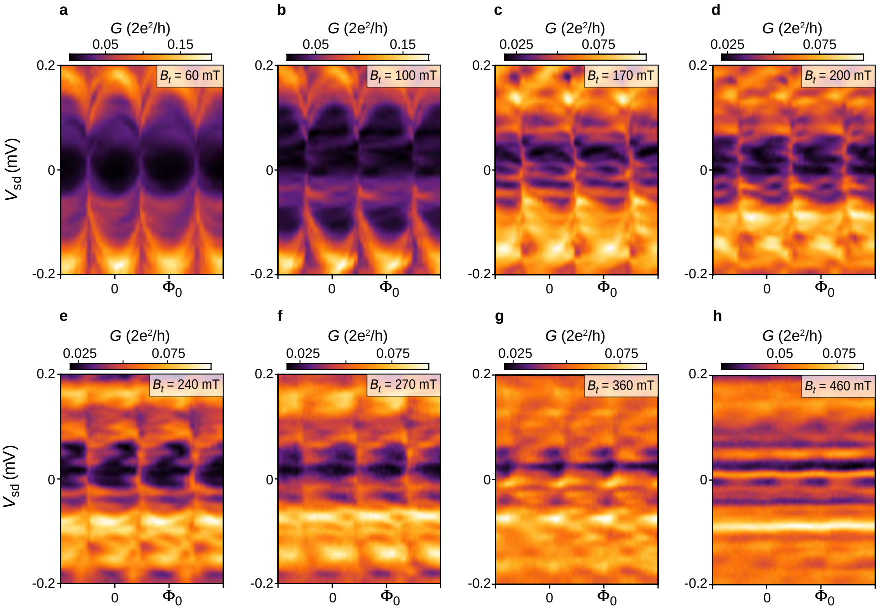

Figure 10.5: Transport spectroscopy in transverse field for device 1. a-h, Differential conductance G as a function of the magnetic flux, Φ, threading the SQUID loop and source-drain bias, V_{sd}, measured at different values of the transverse magnetic field B_{t} (applied in plane orthogonally to the junction) in device 1. Several ABSs enter the gap without sticking to zero energy. The induced gap collapses at $\sim$ 360 mT.

As another interesting test of the topological nature of the observed ZBPs, we performed spectroscopy as a function of the magnetic field B_t applied in the plane of the 2DEG but orthogonal to the one dimensional channel defined by JJ1 (see Fig. 10.1b). In order to induce a topological phase transition, the external magnetic field must be aligned perpendicular to the Rashba SOI. This is expected for a parallel magnetic field $B_{||}$ as discussed above [35, 36]. For a transverse magnetic field B_t a closure of the superconducting and topological gap is expected (see Chapter 2.4) [78]. Applying a transverse magnetic field we do not observe any discrete state sticking at zero energy before the suppression of the induced gap, which occurs at $B_t \sim 360$ mT (see Fig. 10.5).

Finally, it is worth noting that a first-order topological transition is expected for a planar JJ in presence of strong parallel fields. This transition should manifest itself with a minimum of the Josephson critical current [165] when the Zeeman energy reaches a value comparable to the Thouless energy E_T [36]. In our case, however, this limit cannot be reached since $E_T \sim 2.8$ meV is one order of magnitude larger than Δ. In Fig. 10.6a-c we measure the differential resistance R_1 of JJ1 by applying an AC current of $I_{ac} = 5$ nA with the reference junction JJ2 closed. For a width of the superconducting leads $W_{S1} = 160$ nm (as studied above), we observe that $B_{||}$ first reduces the supercurrent to zero at $B_{||} = 1.5$ T and then causes a revival of the supercurrent at $B_{||} \sim 2$ T (see Fig 10.6a). Increasing W_{S1} to 500 nm causes multiple periodic revivals of the supercurrent with $B_{||}$ with a periodicity of ~ 300 mT (shown in Fig. 10.6b). In Fig. 10.6c W_{S1} is increased to 1000 nm and the periodicity is reduced to ~ 150 mT. From the results shown in Fig. 10.6a-c, we observe that the periodicity is correlated to W_{S1} and we ascribe this behavior to trivial orbital effects of the in-plane magnetic field in the proximitized 2DEG underneath the superconducting leads [36]. We corroborate this interpretation by measuring R_1 as a function of I_{dc} and $B_{||}$ ($B_{\perp} = 0$) for $W_{S1} = 500$ nm and 1000 nm, revealing a clear Fraunhofer pattern (see Fig. 10.6d,e).

10.6 Conclusion

In summary, we have investigated phase-dependent ZBPs in tunneling conductance measured at the edge of a JJ patterned in a two-dimensional InAs/Al heterostructure. The critical field at which the ZBP appears depends on the phase bias and is minimal at $\phi \sim \pi$, as expected for a topological JJ. We studied the ZBP stability as a function of field $B_{||}$, phase ϕ and chemical potential μ, obtaining results qualitatively consistent with the topological phase diagram of a finite-size junction.

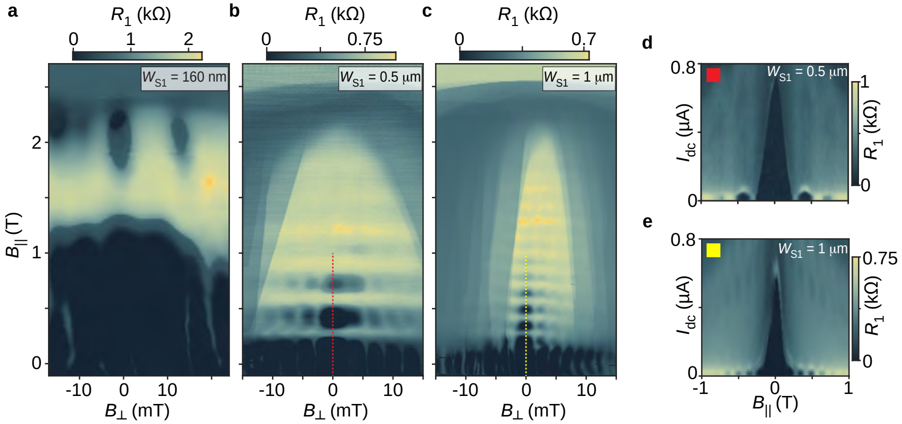

Figure 10.6: Josephson current revival in parallel field. **a**-**c**, Differential resistance R_1 of JJ1 as a function of out-of-plane magnetic field $B_\perp$ and parallel magnetic field $B_{||}$ for superconducting lead widths $W_{S1} = 160$ nm **a**, $W_{S1} = 500$ nm **b**, $W_{S1} = 1000$ nm **c**. **d, e**, R_1 as a function of I_{dc} and $B_{||}$ for $B_\perp = 0$ measured for $W_{S1} = 500$ nm **b**, $W_{S1} = 1000$ nm **c**, as shown by the dashed lines in panels **b** and **c**. The measurements were performed with the QPC and junction 2 pinched off.

OUTLOOK

The finite stability of the zero-bias in chemical potential shown in Fig. 10.3 is related to the narrow superconducting leads. A recent theoretical work addressed this issue, where narrow superconducting leads reduce the effects of ϕ, while increasing the dependence on μ as the nanowire limit is approached [166] *. To achieve the theoretically predicted reduced chemical potential sensitivity, it is necessary to maximize the probability of Andreev reflections. This is achieved by increasing the width of the superconducting leads to $W_{S1} \sim \xi_S \sim 1.5\,\mu$m. However, by making the superconducting leads wider, we encountered that the induced superconducting gap closed at low $B_{||}$. In Fig. 10.7 we show tunneling spectroscopy of Josephson junctions with varying superconducting lead widths W_{S1}. Figure 10.7b shows the differential conductance G as a function of parallel magnetic field $B_{||}$ and bias voltage V_{sd} for $W_{S1} = 160$ nm, revealing a superconducting gap that persists until $\sim$ 0.8 T. However,

---

*For a nanowire system, there is no phase dependence since there is no Josephson junction and there is a large chemical potential dependence.

when W_{S1} was increased to $W_{S1} = 0.5$ μm or 1 μm, the superconducting gap collapsed at $B_{||} \sim 0.2$ T. We believe this is related to the reduced confinement of the 2DEG below the Al, leading to a population of electrons with a higher g-factor. Therefore, for future devices to take full advantage of the planar Josephson junction geometry, this soft gap issue needs to be remedied. Possible resolutions may involve ex-situ superconductor evaporation, etching of the 2DEG below the Al leads, or changing substrates from InP to GaSb to allow for backgating to deplete the 2DEG.

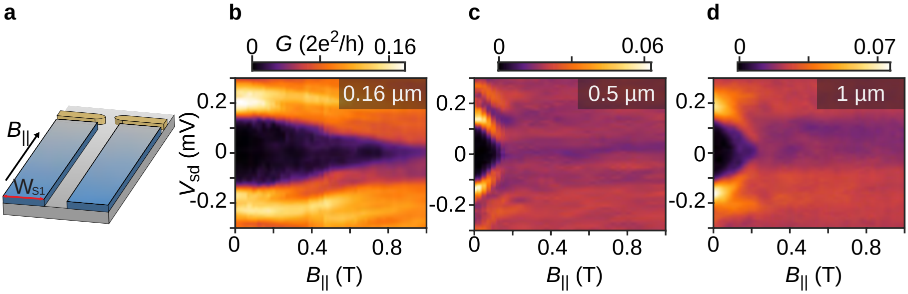

Figure 10.7: Large leads. **a-c**, Differential conductance G as a function of parallel magnetic field $B_{||}$ and bias voltage V_{sd} for $W_{S1} = 160$ nm **b**, $W_{S1} = 500$ nm **c**, $W_{S1} = 1000$ nm **d**, revealing tunneling spectroscopy of Josephson junctions with a width of $W_1 = 80$ nm

METHODS

Material characterization performed in a Hall bar geometry where the Al was removed revealed an electron mobility peak $\mu = 43,000$ cm^{2}V^{-1}s^{-1} for an electron density $n = 8 \times 10^{11}$ cm^{-2}, corresponding to an electron mean free path of $l_\mathrm{e} \sim 600$ nm. Electron transport through JJ1 is therefore expected to be ballistic along the width direction $(l_\mathrm{e} \gg W_1)$ and diffusive along the length direction $(L_1 > l_\mathrm{e})$. Characterization of a large area Al film revealed a critical magnetic field of 2.5 T when the field is applied in the plane of the 2DEG.

We studied seven devices characterized by different dimensions of JJ1. Devices 1 and 2 have $W_1 = 80$ nm and $W_{\mathrm{S}1} = 160$ nm, device 3 has $W_1 = 120$ nm and $W_{\mathrm{S}1} = 160$ nm, device 4 has $W_1 = 40$ nm and $W_{\mathrm{S}1} = 160$ nm, device 5 has $W_1 = 160$ nm and $W_{\mathrm{S}1} = 160$ nm, device 6 has $W_1 = 80$ nm and $W_{\mathrm{S}1} = 500$ nm, whereas device 7 has $W_1 = 80$ nm and $W_{\mathrm{S}1} = 1$ µm. All the devices were designed with $L_1 = 1.6$ µm, $W_2 = 40$ nm, $L_2 = 5$ µm and $W_{\mathrm{S}2} = 160$ nm. Results consistent with those presented in the main text were obtained in devices 1, 2 and 3, while devices 4 and 5 did not show robust ZBPs in field. In devices 6 and 7 the induced superconducting gap collapsed at $B_{||} \sim 200$ mT without showing any robust ZBP. The behavior of devices 6 and 7 is consistent with the softening of the induced gap in low parallel fields observed below wide superconducting leads [61, 101].

10.7 SUPPLEMENTARY

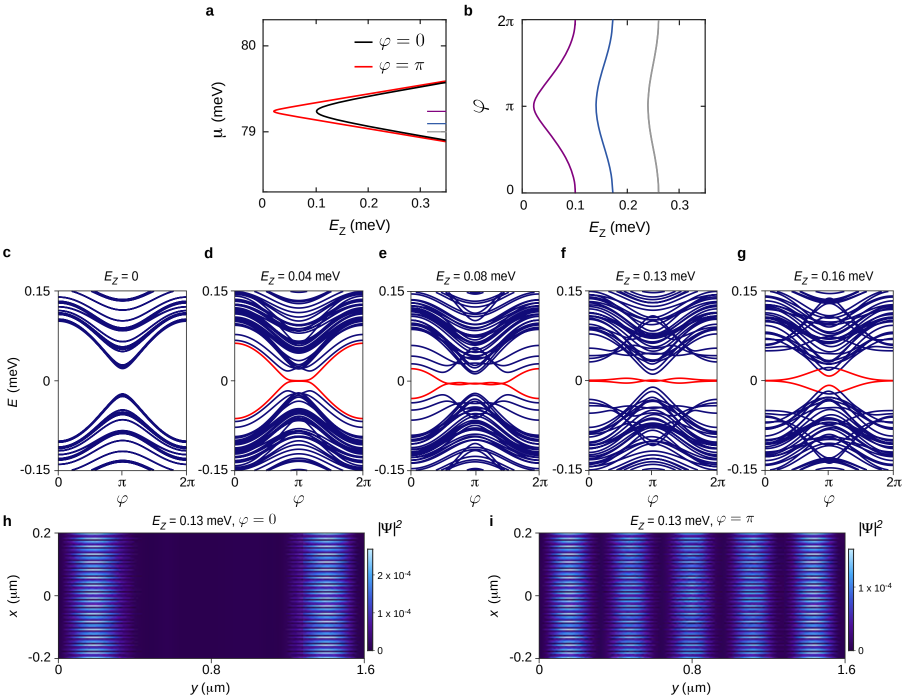

Figure 10.8: Device spectra. Calculated topological phase diagrams and energy spectra for a left-right asymmetric junction (here the asymmetry is introduced by having $\Delta_\mathrm{L} \neq \Delta_\mathrm{R}$). The left-right symmetry may be broken by disorder [99, 164], different geometric sizes of the superconducting leads, or different coupling of the 2DEG to the superconductors on the two sides of the junctions. **a**, Topological phase diagram as a function of the Zeeman energy E_Z and the 2DEG chemical potential μ for phase bias $\phi = 0, \pi$, calculated from the tight-binding Hamiltonian for JJ1 with infinite length (see Methods). **b**, Topological phase diagram as a function of E_Z and ϕ for different values of μ, as indicated by the horizontal ticks in panel **a**. The diagrams were calculated for a junction with width $W_1 = 80$ nm, superconducting lead width $W_{\mathrm{S}1} = 160$ nm, left-induced gap $\Delta_\mathrm{L} = 150$ μeV, right-induced gap $\Delta_\mathrm{R} = 100$ μeV and Rashba spin-orbit coupling constant $\alpha = 100$ meV Å. **c-g**, Calculated energy spectra as a function of ϕ for different values of the Zeeman energy. The spectra were obtained for the same parameters used in panels **a** and **b**, except for $L_1 = 1.6$ μm. For the chosen parameters, the system undergoes a topological transition at $E_\mathrm{Z} = 0.02$ meV for $\phi = \pi$ and at $E_\mathrm{Z} = 0.1$ meV for $\phi = 0$. The lowest subgap states are shown in red and indicate two Majorana zero modes at the edges of the junction in the topological regime. The behavior of the calculated Majorana modes is qualitatively consistent with that of the observed zero-bias peaks in tunneling conductance. **h, i**, Probability density $|\Psi|^2$ of the Majorana wavefunction calculated as a function of the spatial directions x and y in JJ1 for $E_\mathrm{Z} = 0.13$ meV and $\phi = 0, \pi$.

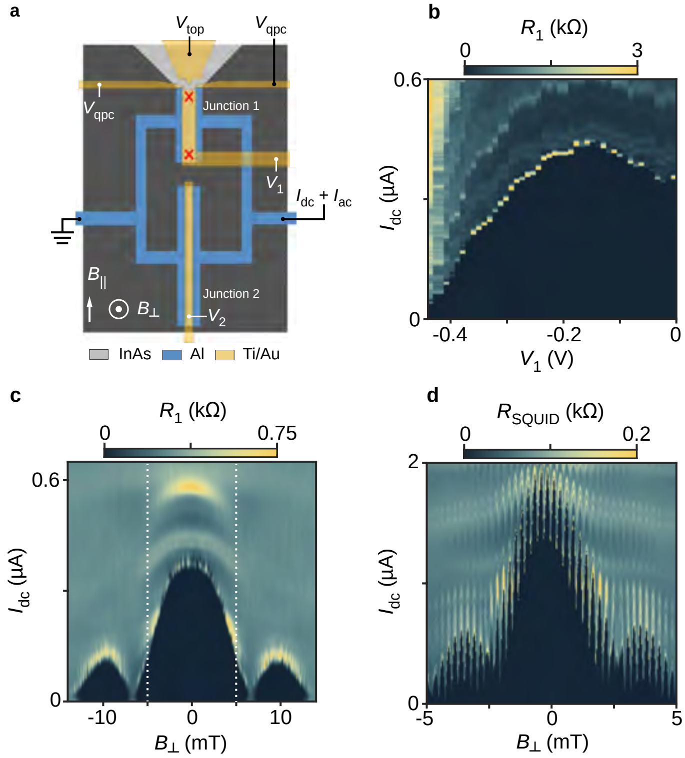

Figure 10.9: Behavior of the Josephson critical current at $B_{||} = 0$. **a**, In order to investigate the behavior of the Josephson current in our device, we measured the differential resistance $R = dV/dI$ of the SQUID with a conventional four-probe technique by applying an AC current bias $I_{ac} < 5$ nA, superimposed to a variable DC current bias I_{DC}, to one of the superconducting leads of the interferometer. During these measurements the QPC was pinched off at $V_{qpc} = -5$ V. The Josephson critical current of JJ1 can be measured independently by pinching off JJ2.**b**, Differential resistance R_1 of JJ1 as a function of the DC bias current I_{dc} and gate voltage V_1 measured in device 2. The region of zero resistance indicates that a dissipationless Josephson current due to Cooper pair transport is flowing through the junction. **b**, R_1 as a function of I_{dc} and the out-of-plane field $B_\perp$ displaying a characteristic Fraunhofer pattern, with a periodicity compatible with the area of JJ1 $W_1 \times L_1 \simeq 0.13$ μm^2. For both the measurements displayed in panels **a** and **c**, JJ2 was pinched off by setting the gate voltage $V_2 = -1.5$ V. **d**, When JJ2 was open ($V_2 = 0$), the differential resistance of the SQUID R_{SQUID} showed periodic oscillations (periodicity of 250 μT, consistent with the area of the superconducting loop, ~ 8 μm^2) superimposed to the Fraunhofer patterns of both junctions. The ratio between the critical currents of the junctions at zero field is extracted from the average value of the SQUID critical current and the semi-amplitude of the SQUID oscillations, resulting in $I_{c,2}(0)/I_{c,1}(0) = 5.2$.

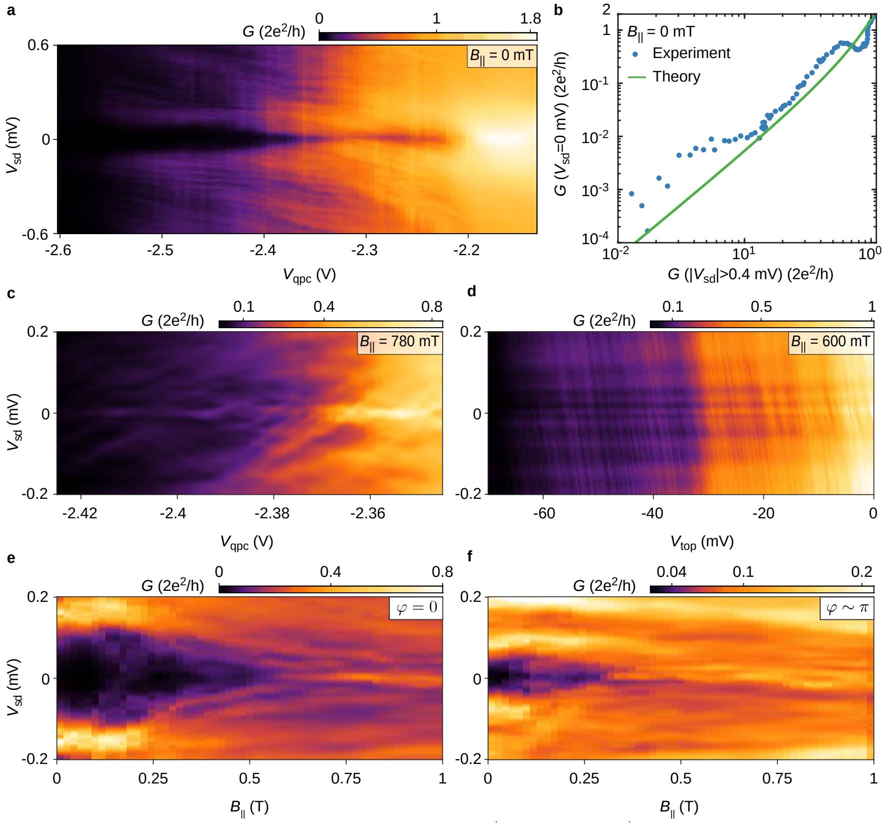

Figure 10.10: Quantum point contact characterization and stability of the zero-bias peak. **a**, Differential conductance G as a function of source-drain bias, V_{sd}, and QPC voltage, V_{qpc}, at zero field in device 1. **b**, Differential conductance at zero source-drain bias, $G(V_{\mathrm{sd}} = 0\ \mathrm{mV})$, versus averaged differential conductance at finite source-drain bias, $G(|V_{\mathrm{sd}}| > 0.4\ \mathrm{mV})$. The green line is the theoretically predicted conductance in an Andreev enhanced QPC, $G_{\mathrm{S}} = 2G_0 \frac{G_{\mathrm{N}}^2}{(2G_0 - G_{\mathrm{N}})^2}$ (Ref. [167]), where G_{S} is the sub-gap conductance, G_{N} is the above-gap conductance and $G_0 = 2e^2/h$ is the quantum of conductance. No fitting parameters have been used. **c**, G as a function of V_{sd} and V_{qpc} at parallel field $B_{||} = 780$ mT and phase bias $\phi \sim 0.8\pi$ for gate voltages $V_1 = -110$ mV and $V_{\mathrm{top}} = -35$ mV. **d**, G as a function of V_{sd} and V_{top} at $B_{||} = 600$ mT and $\phi \sim 0$ for $V_1 = -118.5$ mV and $V_{\mathrm{qpc}} = -2.366$ mV. In both panels **c** and **d**, the ZBP is robust against variation of the above gap conductance of about one order of magnitude. **e**-**f**, Differential conductance G as a function of source-drain bias, V_{sd}, and parallel magnetic field, $B_{||}$, for different values of phase bias ϕ in device 1. The plots have been reconstructed from measurements similar to the ones shown in Fig. 10.2 of the Main Text. For $\phi \sim \pi$ a ZBP forms at $B_{||} = 0.35$ T, while for $\phi = 0$ it appears at $B_{||} = 575$ mT. The ZBP at $\phi \sim \pi$ oscillates and moves away from zero energy as the field is increased.

A

FABRICATION RECIPE

CLEAVING AND CLEANING

1. **Cleaving:**
    (a) Spin A4 for 45 s @ 4000 RPM using dynamic deposition
    (b) Bake @ 185°C for 2 mins
    (c) Manual Scriber: Cleave 3x5mm pieces, long edge parallel to major flat.
2. Choose a chip, preferably from near the center of the wafer
3. **Cleaning:**
    (a) Sonicate in 1-3 Dioxolane, $f = 80$ kHz, PWR = 50-70 %, 5 mins
    (b) Acetone and IPA rinse, 30 s each
    (c) Blow dry well

MESA ETCH

1. **Spin Resist:**
    - (a) Spin A4 for 45 s @ 4000 RPM using dynamic deposition.
    - (b) Bake @ 185°C for 2 mins
2. **Exposure:**
    - (a) Expose fine features with: 500 pA, Beamer settings: InAs 200 nm PEC, write field: 150 μm, dots: 60k, dose: 0.085 μs/dot, area dose: 680 μC/cm^2
    - (b) Expose outer features with: 20 nA, Beamer settings: InAs 200 nm PEC, write field: 600 μm, dots: 20k, dose: 0.34 μs/dot, area dose: 640 μC/cm^2
3. **Processing:**
    - (a) Develop: 60s 1:3 MIBK, rinse 5s IPA, blowdry
    - (b) Oxygen plasma ash: 60s
    - (c) Post bake: 2 mins @ 120°C
4. **Al Etch:**
    - (a) Preparation: Set hot-bath to 53°C. Place in 1 beaker Transene-D Al etch, and 1 beaker MQ water with liquid level matching level in hot-bath. Wait until heated to 50°C. Place one large beaker of MQ outside hot-bath for rinsing.
    - (b) Etching: 5s dip in Transene Al Etch D @ 50°C - Swirl rigorously
    - (c) 20s in MQ @ 50°C - Swirl rigorously
    - (d) 40s in MQ @ Room temperature - Swirl rigorously
    - (e) Blowdry
5. **Mesa Etch:**
    - (a) Preparation: Using a large beaker with a magnetic stirrer, mix together $H_2O : C_6H_8O_7 : H_3PO_4 : H_2O_2$ (220:55:3:3) add in this order and mix for 5 mins.
    - (b) Etch 9 mins for $\sim$ 300 nm - rotating the chip around in the beaker
    - (c) 60s in MQ @ Room temperature - Swirl rigorously
    - (d) Blowdry
    - (e) Strip resist: 20 mins in 1,3-Dioxolane; Acetone and IPA rinse, 30 s each
    - (f) Measure the Mesa height

AL ETCH

1. **Spin Resist:**
    - (a) Spin A4 for 45 s @ 4000 RPM using dynamic deposition.
    - (b) Bake @ 185°C for 2 mins
2. **Exposure:**
    - (a) Expose fine features with: 100 pA, Beamer settings: InAs 200 nm PEC, write field: 150 μm, dots: 60k, dose: 0.4 μs/dot, area dose: 640 μC/cm^2
3. **Processing:**
    - (a) Develop: 45s 1:3 MIBK, rinse 5s IPA, no swirling - blowdry
    - (b) Oxygen plasma ash: 45s
    - (c) Post bake: 2 mins @ 120°C
4. **Al Etch:**
    - (a) Preparation: Set hot-bath to 53°C. Place in 1 beaker Transene D Al etch, and 1 beaker MQ water with liquid level matching level in hot-bath. Wait until heated to 50°C. Place one large beaker of MQ outside hot-bath for rinsing.
    - (b) Etching: 5s dip in Transene Al Etch D @ 50°C - Swirl rigorously
    - (c) 20s in MQ @ 50°C - Swirl rigorously
    - (d) 40s in MQ @ Room temperature - Swirl rigorously
    - (e) Strip resist: 30 mins in 1,3-Dioxolane; Acetone and IPA rinse, 30 s each
5. Transfer directly to ALD

ATOMIC LAYER DEPOSITION

1. **HfO_2:**
   (a) Grow 15 nm of HfO_2 at 90 °C

FINE GATE DEPOSITION

1. **Spin Resist:**
   (a) Spin A4 for 45 s @ 4000 RPM using dynamic deposition.
   (b) Bake @ 185°C for 2 mins
2. **Exposure:**
   (a) Expose fine features with: 100 pA, Beamer settings: InP 200 nm PEC, write field: 150 μm, dots: 60k, dose: 0.38 μs/dot, area dose: 608 $\mu C/cm^2$
3. **Processing:**
   (a) Develop: 45s 1:3 MIBK, rinse 5s IPA, no swirling - blowdry
   (b) Oxygen plasma ash: 45s
4. **Ti/Au Evaporation:**
   (a) Evaporate: 5 nm Ti, 25 nm Au, no tilt or rotation
5. **Liftoff:**
   (a) Overnight liftoff in 1,3-Dioxolane
   (b) Check if liftoff is complete with a microscope while in IPA. Sometimes a gentle squirt of Acetone can help.
   (c) Acetone and IPA rinse, 30 s each
   (d) Blowdry

OUTER GATE DEPOSITION

1. **Spin Resist:**
    (a) Spin El9 for 45 s @ 4000 RPM using dynamic deposition.
    (b) Bake @ 185°C for 2 mins
    (c) Spin El9 for 45 s @ 4000 RPM using dynamic deposition.
    (d) Bake @ 185°C for 2 mins
    (e) Spin A4 for 45 s @ 4000 RPM using dynamic deposition.
    (f) Bake @ 185°C for 2 mins
2. **Exposure:**
    (a) Expose fine features with: 500 pA, Beamer settings: InP 200 nm PEC - 100% Uniform Clearing, write field: 300 μm, dots: 60k, dose: 0.32 μs/dot, area dose: 640 μC/cm^2
    (b) Expose outer features with: 20 nA, Beamer settings: InP 200 nm PEC- 100% Uniform Clearing, write field: 600 μm, dots: 20k, dose: 0.34 μs/dot, area dose: 640 μC/cm^2
3. **Processing:**
    (a) Develop: 45s 1:3 MIBK, rinse 5s IPA, no swirling - blowdry
    (b) Oxygen plasma ash: 60s
4. **Ti/Au Evaporation:** The height of the outer gate evaporation should match the Mesa height
    (a) Evaporate: 10 nm Ti, 5° tilt and rotation
    (b) Evaporate: 25 nm Au, 5° tilt and rotation
    (c) Evaporate: 285 nm Au, 0° tilt
    (d) Evaporate: 50 nm Au, 10° tilt and rotation
5. **Liftoff:**
    (a) Overnight liftoff in 1,3-Dioxolane
    (b) Check if liftoff is complete with a microscope while in IPA. Sometimes a gentle squirt of Acetone can help.
    (c) Acetone and IPA rinse, 30 s each
    (d) Blowdry

B

TUNNELING SPECTROSCOPY

In the tunneling regime, the current flowing between two metals is proportional to the density of occupied states on one lead and to the density of unoccupied states on the other. Consider a system similar to Giaever's experiment, where a N-lead with a constant density of states D_N is separated by a tunnel barrier from another lead with an unknown DOS $D_2(E)$. The resulting tunneling current from a bias voltage V_{sd} is [52, 53],

$$I = \frac{G_0}{e} \int_{-\infty}^{\infty} dE \, D_2(E) D_N \left(f(E - eV_{\mathrm{sd}}) - f(E) \right)$$

where f is the Fermi-Dirac distribution and G_0 is the quantum of conductance follow the Landauer formula $G_0 = 2e^2/h \sum_n^m \mathrm{T}_n$ where T_n is the energy independent transmission for mode n with a total of m modes. The differential conductance then gives,

$$G(V_{\mathrm{sd}}) = \frac{dI}{dV_{\mathrm{sd}}} = G_0 \int_{-\infty}^{\infty} dE \, \frac{df(E - eV_{\mathrm{sd}})}{dV_{\mathrm{sd}}} D_2(E) D_N$$

This expression is simplified by considering that at low temperatures, f is a Heaviside step function and therefore $\frac{d\,f(E - V_{\mathrm{sd}})}{dV_{\mathrm{sd}})} = \delta(E - eV_{\mathrm{sd}})$ [23] which gives,

$$G(V_{\mathrm{sd}}) = G_0 \, D_N \, D_2(eV_{\mathrm{sd}}) \quad .$$

REFERENCES

[1] Koch, J. *et al.* Charge-insensitive qubit design derived from the Cooper pair box. *Physical Review A* **76**, 042319 (2007).

[2] Kjaergaard, M. *et al.* Superconducting qubits: Current state of play. *arXiv preprint arXiv:1905.13641* (2019).

[3] Arute, F. *et al.* Quantum supremacy using a programmable superconducting processor. *Nature* **574**, 505–510 (2019).

[4] Klitzing, K. v., Dorda, G. & Pepper, M. New method for high-accuracy determination of the fine-structure constant based on quantized hall resistance. *Physical Review Letters* **45**, 494 (1980).

[5] Avron, J. E., Osadchy, D. & Seiler, R. A topological look at the quantum hall effect. *Physics today* **56**, 38–42 (2003).

[6] Sarma, S. D., Freedman, M. & Nayak, C. Topological quantum computation. *Physics Today* **59**, 32–38 (2006).

[7] Schwarzschild, B. Physics Nobel Prize goes to Tsui, Stormer and Laughlin for the fractional quantum Hall effect. *Physics Today* **51**, 17–19 (1998).

[8] Lahtinen, V. & Pachos, J. K. A short introduction to topological quantum computation. *SciPost Physics* **3** (2017).

[9] Kitaev, A. Y. Fault-tolerant quantum computation by anyons. *Annals of Physics* **303**, 2–30 (2003).

[10] Stanescu, T. D. *Introduction to Topological Quantum Matter & Quantum Computation* (CRC Press, 2016).

[11] Leijnse, M. & Flensberg, K. Introduction to topological superconductivity and Majorana fermions. *Semiconductor Science and Technology* **27**, 124003 (2012).

[12] Ueno, Y., Yamakage, A., Tanaka, Y. & Sato, M. Symmetry-protected Majorana fermions in topological crystalline superconductors: theory and application to Sr_2RuO_4. *Physical review letters* **111**, 087002 (2013).

[13] Ran, S. *et al.* Nearly ferromagnetic spin-triplet superconductivity. *Science* **365**, 684–687 (2019).

[14] Fu, L. & Kane, C. L. Superconducting proximity effect and Majorana fermions at the surface of a topological insulator. *Physical review letters* **100**, 096407 (2008).

[15] Oreg, Y., Refael, G. & von Oppen, F. Helical liquids and Majorana bound states in quantum wires. *Physical review letters* **105**, 177002 (2010).

[16] Lutchyn, R. M., Sau, J. D. & Sarma, S. D. Majorana fermions and a topological phase transition in semiconductor-superconductor heterostructures. *Physical review letters* **105**, 077001 (2010).

[17] Shabani, J. *et al.* Two-dimensional epitaxial superconductor-semiconductor heterostructures: A platform for topological superconducting networks. *Physical Review B* **93**, 155402 (2016).

[18] Majorana, E. Teoria simmetrica dell-elettrone e del positrone. *Il Nuovo Cimento (1924-1942)* **14**, 171 (1937).

[19] Beenakker, C. & Kouwenhoven, L. A road to reality with topological superconductors. *Nature Physics* **12**, 618 (2016).

[20] Elliott, S. R. & Franz, M. Colloquium: Majorana fermions in nuclear, particle, and solid-state physics. *Reviews of Modern Physics* **87**, 137 (2015).

[21] Read, N. & Green, D. Paired states of fermions in two dimensions with breaking of parity and time-reversal symmetries and the fractional quantum Hall effect. *Physical Review B* **61**, 10267 (2000).

[22] Kitaev, A. Y. Unpaired Majorana fermions in quantum wires. *Physics-Uspekhi* **44**, 131 (2001).

[23] Bruus, H. & Flensberg, K. *Many-body quantum theory in condensed matter physics: an introduction* (Oxford university press, 2004).

[24] Sarma, S. D., Freedman, M. & Nayak, C. Majorana zero modes and topological quantum computation. *npj Quantum Information* **1**, 15001 (2015).

[25] Knapp, C., Karzig, T., Lutchyn, R. M. & Nayak, C. Dephasing of Majorana-based qubits. *Physical Review B* **97**, 125404 (2018).

[26] Fu, L. Electron teleportation via Majorana bound states in a mesoscopic superconductor. *Physical review letters* **104**, 056402 (2010).

[27] Nakamura, Y., Pashkin, Y. A. & Tsai, J. S. Coherent control of macroscopic quantum states in a single-cooper-pair box. *Nature* **398**, 786–788 (1999).

[28] Alicea, J., Oreg, Y., Refael, G., Von Oppen, F. & Fisher, M. P. Non-Abelian statistics and topological quantum information processing in 1D wire networks. *Nature Physics* **7**, 412 (2011).

[29] Vijay, S. & Fu, L. Teleportation-based quantum information processing with Majorana zero modes. *Physical Review B* **94**, 235446 (2016).

[30] Flensberg, K. Non-Abelian operations on Majorana fermions via single-charge control. *Physical review letters* **106**, 090503 (2011).

[31] Aasen, D. *et al.* Milestones toward Majorana-based quantum computing. *Physical Review X* **6**, 031016 (2016).

[32] Karzig, T. *et al.* Scalable designs for quasiparticle-poisoning-protected topological quantum computation with Majorana zero modes. *Physical Review B* **95**, 235305 (2017).

[33] Plugge, S., Rasmussen, A., Egger, R. & Flensberg, K. Majorana box qubits. *New Journal of Physics* **19**, 012001 (2017).

[34] Bonderson, P., Freedman, M. & Nayak, C. Measurement-only topological quantum computation. *Physical review letters* **101**, 010501 (2008).

[35] Hell, M., Leijnse, M. & Flensberg, K. Two-dimensional platform for networks of Majorana bound states. *Physical review letters* **118**, 107701 (2017).

[36] Pientka, F. *et al.* Topological superconductivity in a planar Josephson junction. *Physical Review X* **7**, 021032 (2017).

[37] Stern, A. & Berg, E. Fractional Josephson Vortices and Braiding of Majorana Zero Modes in Planar Superconductor-Semiconductor Heterostructures. *Physical review letters* **122**, 107701 (2019).

[38] Tsui, D. C., Stormer, H. L. & Gossard, A. C. Two-dimensional magnetotransport in the extreme quantum limit. *Physical Review Letters* **48**, 1559 (1982).

[39] Van Wees, B. *et al.* Quantized conductance of point contacts in a two-dimensional electron gas. *Physical Review Letters* **60**, 848 (1988).

[40] Harmans, C. *Mesoscopic Physics: An Introduction: TN385.* (TU Delft, 1997).

[41] Nazarov, Y. V., Nazarov, Y. & Blanter, Y. M. *Quantum transport: introduction to nanoscience* (Cambridge University Press, 2009).

[42] Ihn, T. *Semiconductor Nanostructures: Quantum states and electronic transport* (Oxford University Press, 2010).

[43] Chapman, M. & De Melo, C. S. Atomic physics: Atoms playing dress-up. *Nature* **471**, 41 (2011).

[44] De Andrada e Silva, E., La Rocca, G. & Bassani, F. Spin-split subbands and magneto-oscillations in III-V asymmetric heterostructures. *Physical Review B* **50**, 8523–8533 (1994).

[45] Středa, P. & Šeba, P. Antisymmetric spin filtering in one-dimensional electron systems with uniform spin-orbit coupling. *Physical review letters* **90**, 256601 (2003).

[46] Bercioux, D. & Lucignano, P. Quantum transport in Rashba spin-orbit materials: a review. *Reports on Progress in Physics* **78**, 106001 (2015).

[47] Groth, C. W., Wimmer, M., Akhmerov, A. R. & Waintal, X. Kwant: a software package for quantum transport. *New Journal of Physics* **16**, 063065 (2014).

[48] Winkler, R. Spin-orbit coupling effects in two-dimensional electron and hole systems. *Springer Tracts in Modern Physics* **191** (2003).

[49] Wickramasinghe, K. S. *et al.* Transport properties of near surface inas two-dimensional heterostructures. *Applied Physics Letters* **113**, 262104 (2018).

[50] O'Farrell, E. C. T. *et al.* Hybridization of sub-gap states in one-dimensional superconductor/semiconductor Coulomb islands. *Physical Review Letters* **121**, 256803 (2018).

[51] Bardeen, J., Cooper, L. N. & Schrieffer, J. R. Microscopic theory of superconductivity. *Physical Review* **106**, 162 (1957).

[52] Tinkham, M. *Introduction to superconductivity* (Courier Corporation, 2004).

[53] Klapwijk, T. Proximity effect from an Andreev perspective. *Journal of superconductivity* **17**, 593–611 (2004).

[54] Schäpers, T. *Superconductor/semiconductor junctions*, vol. 174 (Springer Tracts in Modern Physics, 2001).

[55] Beenakker, C. Three "universal" mesoscopic Josephson effects. In *Transport Phenomena in Mesoscopic Systems*, 235–253 (Springer, 1992).

[56] Giaever, I. Energy gap in superconductors measured by electron tunneling. *Physical Review Letters* **5**, 147 (1960).

[57] Nicol, J., Shapiro, S. & Smith, P. H. Direct measurement of the superconducting energy gap. *Physical Review Letters* **5**, 461 (1960).

[58] Eschrig, M. Spin-polarized supercurrents for spintronics. *Phys. Today* **64**, 43 (2011).

[59] Blonder, G., Tinkham, M. & Klapwijk, T. Transition from metallic to tunneling regimes in superconducting microconstrictions: Excess current, charge imbalance, and supercurrent conversion. *Physical Review B* **25**, 4515 (1982).

[60] Andreev, A. F. The thermal conductivity of the intermediate state in superconductors. *Sov. Phys. JETP* **19**, 1228–1231 (1964).

[61] Kjærgaard, M. *et al.* Quantized conductance doubling and hard gap in a two-dimensional semiconductor–superconductor heterostructure. *Nature communications* **7**, 12841 (2016).

[62] Zhang, H. *et al.* Ballistic superconductivity in semiconductor nanowires. *Nature communications* **8**, 16025 (2017).

[63] Beenakker, C. Universal limit of critical-current fluctuations in mesoscopic Josephson junctions. *Physical review letters* **67**, 3836 (1991).

[64] Josephson, B. D. Possible new effects in superconductive tunnelling. *Physics letters* **1**, 251–253 (1962).

[65] Schwartz, B. *Superconductor applications: SQUIDs and machines*, vol. 21 (Springer Science & Business Media, 2013).

[66] Gross, R. & Marx, A. Applied superconductivity: Josephson effect and superconducting electronics (2005). *Lecture notes* (2005).

[67] Josephson, B. D. The discovery of tunnelling supercurrents. *Reviews of Modern Physics* **46**, 251 (1974).

[68] Beenakker, C. & Van Houten, H. Josephson current through a superconducting quantum point contact shorter than the coherence length. *Physical review letters* **66**, 3056 (1991).

[69] Anderson, P. W. & Rowell, J. M. Probable observation of the Josephson superconducting tunneling effect. *Physical Review Letters* **10**, 230 (1963).

[70] Deaver Jr, B. S. & Fairbank, W. M. Experimental evidence for quantized flux in superconducting cylinders. *Physical Review Letters* **7**, 43 (1961).

[71] Doll, R. & Näbauer, M. Experimental proof of magnetic flux quantization in a superconducting ring. *Physical Review Letters* **7**, 51 (1961).

[72] Della Rocca, M. *et al.* Measurement of the current-phase relation of superconducting atomic contacts. *Physical review letters* **99**, 127005 (2007).

[73] Peng, Y., Pientka, F., Berg, E., Oreg, Y. & von Oppen, F. Signatures of topological Josephson junctions. *Physical Review B* **94**, 085409 (2016).

[74] Mishmash, R. V., Aasen, D., Higginbotham, A. P. & Alicea, J. Approaching a topological phase transition in Majorana nanowires. *Physical Review B* **93**, 245404 (2016).

[75] von Oppen, F., Peng, Y. & Pientka, F. Topological superconducting phases in one dimension. *Lecture Notes of the Les Houches Summer School: Topological Aspects of Condensed Matter Physics* 387–447 (2017).

[76] Sarma, S. D., Sau, J. D. & Stanescu, T. D. Splitting of the zero-bias conductance peak as smoking gun evidence for the existence of the Majorana mode in a superconductor-semiconductor nanowire. *Physical Review B* **86**, 220506 (2012).

[77] Albrecht, S. M. *et al.* Exponential protection of zero modes in Majorana islands. *Nature* **531**, 206–209 (2016).

[78] Osca, J., Ruiz, D. & Serra, L. Effects of tilting the magnetic field in one-dimensional Majorana nanowires. *Phys. Rev. B* **89**, 245405 (2014).

[79] Mourik, V. *et al.* Signatures of Majorana fermions in hybrid superconductor-semiconductor nanowire devices. *Science* **336**, 1003–1007 (2012).

[80] Deng, M. *et al.* Majorana bound state in a coupled quantum-dot hybrid-nanowire system. *Science* **354**, 1557–1562 (2016).

[81] Nichele, F. *et al.* Scaling of Majorana zero-bias conductance peaks. *Phys. Rev. Lett.* **119**, 136803 (2017).

[82] Zhang, H. *et al.* Quantized Majorana conductance. *Nature* **556**, 74–79 (2018).

[83] Dmytruk, O. & Klinovaja, J. Suppression of the overlap between Majorana fermions by orbital magnetic effects in semiconducting-superconducting nanowires. *Physical Review B* **97**, 155409 (2018).

[84] Winkler, G. W. *et al.* Orbital contributions to the electron g factor in semiconductor nanowires. *Physical review letters* **119**, 037701 (2017).

[85] Vaitiekėnas, S., Deng, M.-T., Nygård, J., Krogstrup, P. & Marcus, C. Effective g factor of subgap states in hybrid nanowires. *Physical review letters* **121**, 037703 (2018).

[86] Antipov, A. E. *et al.* Effects of gate-induced electric fields on semiconductor Majorana nanowires. *Physical Review X* **8**, 031041 (2018).

[87] Winkler, G. W. *et al.* Unified numerical approach to topological semiconductor-superconductor heterostructures. *Physical Review B* **99**, 245408 (2019).

[88] Moore, C., Stanescu, T. D. & Tewari, S. Two-terminal charge tunneling: Disentangling Majorana zero modes from partially separated Andreev bound states in semiconductor-superconductor heterostructures. *Physical Review B* **97**, 165302 (2018).

[89] Chang, W. *et al.* Hard gap in epitaxial semiconductor–superconductor nanowires. *Nature nanotechnology* **10**, 232 (2015).

[90] Krogstrup, P. *et al.* Epitaxy of semiconductor–superconductor nanowires. *Nature materials* **14**, 400 (2015).

[91] Krizek, F. *et al.* Field effect enhancement in buffered quantum nanowire networks. *Physical Review Materials* **2**, 093401 (2018).

[92] Vaitiekėnas, S. *et al.* Selective-area-grown semiconductor-superconductor hybrids: A basis for topological networks. *Physical review letters* **121**, 147701 (2018).

[93] Drachmann, A. *et al.* Proximity effect transfer from NbTi into a semiconductor heterostructure via epitaxial Aluminum. *Nano letters* **17**, 1200–1203 (2017).

[94] Kjærgaard, M. *et al.* Transparent semiconductor-superconductor interface and induced gap in an epitaxial heterostructure Josephson junction. *Physical Review Applied* **7**, 034029 (2017).

[95] Lee, J. S. *et al.* Transport studies of epi-al/inas two-dimensional electron gas systems for required building-blocks in topological superconductor networks. *Nano letters* **19**, 3083–3090 (2019).

[96] Mayer, W. *et al.* Superconducting proximity effect in epitaxial al-inas heterostructures. *Applied Physics Letters* **114**, 103104 (2019).

[97] Bøttcher, C. *et al.* Superconducting, insulating and anomalous metallic regimes in a gated two-dimensional semiconductor–superconductor array. *Nature Physics* **14**, 1138 (2018).

[98] Casparis, L. *et al.* Superconducting gatemon qubit based on a proximitized two-dimensional electron gas. *Nature nanotechnology* **13**, 915 (2018).

[99] Suominen, H. *et al.* Anomalous Fraunhofer interference in epitaxial superconductor-semiconductor Josephson junctions. *Physical Review B* **95**, 035307 (2017).

[100] de Vries, F. K. *et al.* h/e superconducting quantum interference through trivial edge states in inas. *Physical review letters* **120**, 047702 (2018).

[101] Suominen, H. J. *et al.* Zero-energy modes from coalescing Andreev states in a two-dimensional semiconductor-superconductor hybrid platform. *Physical review letters* **119**, 176805 (2017).

[102] Fornieri, A. *et al.* Evidence of topological superconductivity in planar Josephson junctions. *Nature* **569**, 89 (2019).

[103] Thomas, C. *et al.* High-mobility InAs 2DEGs on GaSb substrates: A platform for mesoscopic quantum transport. *Physical Review Materials* **2**, 104602 (2018).

[104] Pauka, S. *et al.* Repairing the Surface of InAs-based Topological Heterostructures. *arXiv preprint arXiv:1908.08689* (2019).

[105] Meservey, R. & Tedrow, P. Properties of very thin aluminum films. *Journal of Applied Physics* **42**, 51–53 (1971).

[106] Nichele, F. *et al.* Scaling of Majorana zero-bias conductance peaks. *Physical review letters* **119**, 136803 (2017).

[107] Ludwig, T. & Mirlin, A. D. Interaction-induced dephasing of Aharonov-Bohm oscillations. *Phys. Rev. B* **69**, 193306 (2004).

[108] Kjaergaard, M. Proximity induced superconducting properties in one and two dimensional semiconductors. *University of Copenhagen* (2015).

[109] Van Heck, B., Lutchyn, R. & Glazman, L. Conductance of a proximitized nanowire in the coulomb blockade regime. *Physical Review B* **93**, 235431 (2016).

[110] Hekking, F. W. J., Glazman, L. I., Matveev, K. A. & Shekhter, R. I. Coulomb blockade of two-electron tunneling. *Phys. Rev. Lett.* **70**, 4138 (1993).

[111] Chiu, C.-K., Sau, J. D. & Sarma, S. D. Conductance of a superconducting Coulomb-blockaded Majorana nanowire. *Phys. Rev. B* **96**, 054504 (2017).

[112] Albrecht, S. *et al.* Transport signatures of quasiparticle poisoning in a Majorana island. *Physical review letters* **118**, 137701 (2017).

[113] Higginbotham, A. P. *et al.* Parity lifetime of bound states in a proximitized semiconductor nanowire. *Nat. Phys* **11**, 1017–1021 (2015).

[114] Deng, M.-T. *et al.* Nonlocality of Majorana modes in hybrid nanowires. *Phys. Rev. B* **98**, 085125 (2018).

[115] Sau, J. D., Swingle, B. & Tewari, S. Proposal to probe quantum nonlocality of Majorana fermions in tunneling experiments. *Phys. Rev. B* **92**, 020511 (2015).

[116] Hell, M., Flensberg, K. & Leijnse, M. Distinguishing Majorana bound states from localized Andreev bound states by interferometry. *Phys. Rev. B* **97**, 161401 (2018).

[117] Drukier, C., Zirnstein, H.-G., Rosenow, B., Stern, A. & Oreg, Y. Evolution of the transmission phase through a Coulomb-blockaded Majorana wire. *Phys. Rev. B* **98**, 161401 (2018).

[118] Aharonov, Y. & Bohm, D. Significance of electromagnetic potentials in the quantum theory. *Phys. Rev.* **115**, 485 (1959).

[119] Yacoby, A., Schuster, R. & Heiblum, M. Phase rigidity and h/2e oscillations in a single-ring Aharonov-Bohm experiment. *Phys. Rev. B* **53**, 9583 (1996).

[120] Schuster, R. *et al.* Phase measurement in a quantum dot via a double-slit interference experiment. *Nature* **385**, 417–420 (1997).

[121] Avinun-Kalish, M., Heiblum, M., Zarchin, O., Mahalu, D. & Umansky, V. Crossover from 'mesoscopic' to 'universal' phase for electron transmission in quantum dots. *Nature* **436**, 529–533 (2005).

[122] Edlbauer, H. *et al.* Non-universal transmission phase behaviour of a large quantum dot. *Nat. Commun.* **8**, 1710 (2017).

[123] Tuominen, M. T., Hergenrother, J. M., Tighe, T. S. & Tinkham, M. Experimental evidence for parity-based 2e periodicity in a superconducting single-electron tunneling transistor. *Phys. Rev. Lett.* **69**, 1997 (1992).

[124] Eiles, T. M., Martinis, J. M. & Devoret, M. H. Even-odd asymmetry of a superconductor revealed by the Coulomb blockade of Andreev reflection. *Phys. Rev. Lett.* **70**, 1862 (1993).

[125] Shen, J. *et al.* Parity transitions in the superconducting ground state of hybrid InSb-Al Coulomb islands. *Nat. Commun.* **9**, 4801 (2018).

[126] Moore, C., Stanescu, T. D. & Tewari, S. Two-terminal charge tunneling: Disentangling Majorana zero modes from partially separated Andreev bound states in semiconductor-superconductor heterostructures. *Phys. Rev. B* **97**, 165302 (2018).

[127] Savitzky, A. & Golay, M. J. Smoothing and differentiation of data by simplified least squares procedures. *Anal. Chem.* **36**, 1627–1639 (1964).

[128] Gharavi, K., Hoving, D. & Baugh, J. Readout of Majorana parity states using a quantum dot. *Physical Review B* **94**, 155417 (2016).

[129] Ménard, G. C. *et al.* Suppressing quasiparticle poisoning with a voltage-controlled filter. *Physical Review B* **100**, 165307 (2019).

[130] Lee, E. J. *et al.* Spin-resolved Andreev levels and parity crossings in hybrid superconductor–semiconductor nanostructures. *Nature nanotechnology* **9**, 79 (2014).

[131] Larsen, T. W. *et al.* Semiconductor-nanowire-based superconducting qubit. *Physical review letters* **115**, 127001 (2015).

[132] Zazunov, A., Shumeiko, V., Bratus, E., Lantz, J. & Wendin, G. Andreev level qubit. *Physical review letters* **90**, 087003 (2003).

[133] Janvier, C. *et al.* Coherent manipulation of Andreev states in superconducting atomic contacts. *Science* **349**, 1199–1202 (2015).

[134] Yokoyama, T., Eto, M. & Nazarov, Y. V. Anomalous Josephson effect induced by spin-orbit interaction and Zeeman effect in semiconductor nanowires. *Physical Review B* **89**, 195407 (2014).

[135] Ryazanov, V. *et al.* Coupling of two superconductors through a ferromagnet: Evidence for a π junction. *Physical review letters* **86**, 2427 (2001).

[136] De Franceschi, S., Kouwenhoven, L., Schönenberger, C. & Wernsdorfer, W. Hybrid superconductor–quantum dot devices. *Nature nanotechnology* **5**, 703 (2010).

[137] Eichler, A. *et al.* Even-odd effect in Andreev transport through a carbon nanotube quantum dot. *Physical review letters* **99**, 126602 (2007).

[138] Sand-Jespersen, T. *et al.* Kondo-enhanced Andreev tunneling in inas nanowire quantum dots. *Physical review letters* **99**, 126603 (2007).

[139] Yu, L. Bound state in superconductors with paramagnetic impurities. *Acta Phys. Sin* **21**, 75–91 (1965).

[140] Shiba, H. Classical spins in superconductors. *Progress of theoretical Physics* **40**, 435–451 (1968).

[141] Rusinov, A. Theory of gapless superconductivity in alloys containing paramagnetic impurities. *Sov. Phys. JETP* **29**, 1101–1106 (1969).

[142] Jellinggaard, A., Grove-Rasmussen, K., Madsen, M. H. & Nygård, J. Tuning Yu-Shiba-Rusinov states in a quantum dot. *Physical Review B* **94**, 064520 (2016).

[143] Delagrange, R. *et al.* 0- π quantum transition in a carbon nanotube Josephson junction: Universal phase dependence and orbital degeneracy. *Physica B: Condensed Matter* **536**, 211–222 (2018).

[144] Scherübl, Z. *et al.* Large spatial extension of the zero-energy Yu-Shiba-Rusinov state in magnetic field. *arXiv preprint arXiv:1906.08531* (2019).

[145] Kiršanskas, G., Goldstein, M., Flensberg, K., Glazman, L. I. & Paaske, J. Yu-Shiba-Rusinov states in phase-biased superconductor–quantum dot–superconductor junctions. *Physical Review B* **92**, 235422 (2015).

[146] Pillet, J. *et al.* Andreev bound states in supercurrent-carrying carbon nanotubes revealed. *Nature Physics* **6**, 965 (2010).

[147] Chang, W., Manucharyan, V., Jespersen, T. S., Nygård, J. & Marcus, C. M. Tunneling spectroscopy of quasiparticle bound states in a spinful Josephson junction. *Physical review letters* **110**, 217005 (2013).

[148] Vecino, E., Martín-Rodero, A. & Yeyati, A. L. Josephson current through a correlated quantum level: Andreev states and π junction behavior. *Physical Review B* **68**, 035105 (2003).

[149] Saldaña, J. E. *et al.* Charge localization and reentrant superconductivity in a quasi-ballistic InAs nanowire coupled to superconductors. *Science advances* **5**, eaav1235 (2019).

[150] Zuo, K. *et al.* Supercurrent interference in few-mode nanowire Josephson junctions. *Physical review letters* **119**, 187704 (2017).

[151] Gharavi, K. *et al.* Josephson interference due to orbital states in a nanowire proximity effect junction. *arXiv preprint arXiv:1405.7455* (2014).

[152] Van Dam, J. A., Nazarov, Y. V., Bakkers, E. P., De Franceschi, S. & Kouwenhoven, L. P. Supercurrent reversal in quantum dots. *Nature* **442**, 667 (2006).

[153] Li, C. *et al.* Zeeman-effect-induced 0- π transitions in ballistic Dirac semimetal Josephson junctions. *Physical review letters* **123**, 026802 (2019).

[154] Rozhkov, A. & Arovas, D. P. Josephson coupling through a magnetic impurity. *Physical review letters* **82**, 2788 (1999).

[155] Prada, E., Aguado, R. & San-Jose, P. Measuring Majorana nonlocality and spin structure with a quantum dot. *Physical Review B* **96**, 085418 (2017).

[156] Clarke, D. J. Experimentally accessible topological quality factor for wires with zero energy modes. *Physical Review B* **96**, 201109 (2017).

[157] Schulenborg, J. & Flensberg, K. Detection of Majorana modes via supercurrents through quantum dots. *arXiv preprint arXiv:1910.04106* (2019).

[158] Nijholt, B. & Akhmerov, A. R. Orbital effect of magnetic field on the majorana phase diagram. *Physical Review B* **93**, 235434 (2016).

[159] Nayak, C., Simon, S. H., Stern, A., Freedman, M. & Sarma, S. D. Non-abelian anyons and topological quantum computation. *Rev. Mod. Phys.* **80**, 1083 (2008).

[160] Hell, M., Flensberg, K. & Leijnse, M. Coupling and braiding Majorana bound states in networks defined in two-dimensional electron gases with proximity-induced superconductivity. *Phys. Rev. B* **96**, 035444 (2017).

[161] Kulik, I. O. Macroscopic quantization and the proximity effect in S-N-S junctions. *Sov. Phys. JETP* **30**, 944–950 (1970).

[162] Yokoyama, T., Eto, M. & V. Nazarov, Y. Josephson current through semiconductor nanowire with spin-orbit interaction in magnetic field. *J. Phys. Soc. Jpn.* **82**, 054703 (2013).

[163] van Woerkom, D. J. *et al.* Microwave spectroscopy of spinful Andreev bound states in ballistic semiconductor. *Nat. Phys.* **13**, 876 (2017).

[164] Haim, A. & Stern, A. Benefits of weak disorder in one-dimensional topological superconductors. *Physical review letters* **122**, 126801 (2019).

[165] Hart, S. *et al.* Controlled finite momentum pairing and spatially varying order parameter in proximitized hgte quantum wells. *Nat. Phys.* **13**, 87–93 (2016).

[166] Setiawan, F., Stern, A. & Berg, E. Topological superconductivity in planar Josephson junctions: Narrowing down to the nanowire limit. *Physical Review B* **99**, 220506 (2019).

[167] Beenakker, C. Quantum transport in semiconductor-superconductor microjunctions. *Physical Review B* **46**, 12841 (1992).